Urban Area Information Extraction From Polarimetric SAR Data

Deliang Xiang

Doctoral Thesis in Geoinformatics

May 2016

Abstract

Synthetic Aperture Radar (SAR) is an active remote sensing technique capable of imaging regions of interest independent from daytime and to great extent unimpaired by weather conditions. However, the acquired data are imaged with single polarization. Along with the launch of airborne and spaceborne Polarimetric Synthetic Aperture Radar (PolSAR) sensors, PolSAR has been used for various remote sensing applications since more information could be obtained in multiple polarizations. As a consequence, it is feasible and promising to use PolSAR data for urban information extraction and analysis. The overall objective of this thesis is to investigate urban area information extraction from PolSAR data with the following specific objectives: (1) to exploit polarimetric scattering model-based decomposition methods for urban areas, (2) to investigate effective methods for man-made target detection, (3) to develop edge detection and superpixel generation methods, and (4) to investigate urban area classification and segmentation. Six PolSAR images acquired from airborne and spaceborne sensors were used in this research.

Urban scattering model-based decomposition of PolSAR data plays a key role in urban classification, segmentation and target detection. Many decomposition techniques have been proposed for urban areas, mainly resolving the overestimation problem of volume scattering. Paper 1 proposes a new scattering coherency matrix to model the cross-polarized scattering component from urban areas, which adaptively considers the polarization orientation angles of buildings. Thus, the HV scattering components from forests and oriented urban areas can be modelled respectively. Paper 2 presents two urban area decompositions using this scattering model. After the decomposition, urban scattering components can be effectively extracted.

Detection of man-made targets in urban areas has a close relationship with urban planning, rescue service, etc. Paper 3 presents an improved man-made target detection method for PolSAR data based on nonstationarity and asymmetry. Nonstationarity in azimuth direction is already utilized to separate man-made and natural targets in urban areas. However, there are still some drawbacks. Some small man-made targets and roads cannot be effectively detected. In addition, nonstationarity can also occur in some other natural surfaces, such as cropland with Bragg

resonance. Therefore, to resolve these problems, reflection asymmetry was incorporate into the azimuth nonstationarity extraction method to improve the man-made target detection accuracy, i.e., removing the natural areas and detecting the small targets.

In Paper 4, the edge detection of PolSAR data was investigated using SIRV model and Gauss-shaped filter. The classic CFAR edge detector with rectangle-shaped filter is proved to be effective and widely used in PolSAR images. However, the assumption of Wishart distribution is often not respected in heterogeneous urban areas. In addition, as a simple smoothing filter, the rectangle-shaped window is often shown to be easy to incur false edge pixels near the true edges. To overcome this restriction, a new edge detector for PolSAR images was proposed, which utilized SIRV product model to estimate the normalized covariance matrix for each pixel and then replaced the rectangle-shaped filter with the Gauss-shaped filter. This detector can locate the edge pixels accurately with fewer omissions. Therefore, it could be quite useful for speckle noise reduction, superpixel generation and other applications.

On the basis of decomposed scattering components, Paper 5 investigates an unsupervised urban area classification method for PolSAR data. The discrimination abilities of different scattering components are compared and analysed. After that, unsupervised K-means classifier is adopted to discriminate the buildings and natural areas. The ortho and oriented buildings can be discriminated very well. Based on Paper 4, Paper 6 proposes an adaptive superpixel generation method for PolSAR images. Regarding the superpixels as objects, the pixel-based classification result could be further improved with the object-based processing.

Keywords: Polarimetric SAR, Scattering Decomposition, Man-Made Target Detection, Edge Detection, Superpixel, Urban Classification

Sammanfattning

Synthetic Aperture Radar (SAR) är en aktiv fjärranalysteknik som kan skanna regioner av intresse oberoende från dagtid och i stor utsträckning av väderförhållanden. Dock är det insamlade data enkelpolariserad. Tillsammans med lanseringen av luft- och rymdburna polarimetriska Synthetic Aperture Radar (PolSAR) sensorer har PolSAR använts för olika fjärranalystillämpningar, eftersom mer information kan erhållas från multipolarisad data. Som en följd av detta är det möjligt och lovande att använda PolSAR data för informationsutvinning och analys över urbana områden. Det övergripande syftet med denna avhandling är att undersöka informationshämtning över urbana områden från PolSAR data med följande särskilda mål: (1) att utnyttja polarimetrisk spridningsmodellbaserade nedbrytningsmetoder för stadsområden, (2) att undersöka effektiva metoder för upptäckt av konstgjorda objekt, (3) att utveckla metoder som kantavkänning och superpixel generation, och (4) för att undersöka klassificering och segmentering av stadsområden. Sex PolSAR bilder som förvärvats från luftburna och rymdburna sensorer användes i denna forskning.

Modellbased nedbrytning över urbana områden av spridning från PolSAR data spelar en nyckelroll i klassificering av urbana områden, segmentering och upptäckt av föremål. Många nedbrytningstekniker har föreslagits för stadsområden, framför allt för att lösa överskattningsproblematiken med volymspridning. Artikel 1 föreslår en ny spridnings-koherens matris för att modellera korspolariserade spridningskomponent från tätorter, som adaptivt utvärderar polariseringsorienteringsvinkel av byggnader. Således kan HV spridningskomponenter från skogar och orienterade stadsområden modelleras respektive. Artikel 2 presenterar nedbrytningstekniken över två urbana områden med hjälp av denna spridningsmodell. Efter nedbrytningen kunde urbana spridningskomponenter effektivt extraheras.

Upptäckt av konstgjorda föremål i stadsområden har en nära relation med stadsplanering, räddningstjänst, etc. Artikel 3 presenterar en förbättrad detekteringsmetod för konstgjorda mål med PolSAR data baserade på icke-stationaritet och asymmetri. Icke-stationaritet i azimut riktning redan används för att separera konstgjorda och naturliga föremål i stadsområden. Det finns emellertid fortfarande vissa nackdelar. Några små konstgjorda föremål och vägar kan inte effektivt upptäckas.

Dessutom kan icke-stationaritet också förekomma hos vissa andra naturliga ytor, såsom åkermark med Bragg resonans. För att lösa dessa problem, integrerades reflektionsasymmetri i icke-stationaritetsmetoden för att förbättra noggrannheten i upptäckten av konstgjorda föremål, dvs. att ta bort naturområden och upptäcka de små föremålen.

I artikel 4 undersöktes kantdetektering av PolSAR data med hjälp av SIRV modell och ett Gauss-formad filter. Den klassiska CFAR kantdetektor med rektangel-formade filtret visat sig vara effektiv och används i stor utsträckning i samband med PolSAR bilder. Emellertid är antagandet av Wishart-fördelning ofta inte iakttagits i heterogena stadsområden. Dessutom är det enkla rektangelfiltret benäget att skapa falska kantpixlar nära riktiga kanter. För att åtgärda denna begränsning har en ny kantdetektor för PolSAR bilder föreslagits som utnyttjade SIRV produktmodell för att uppskatta den normaliserade kovariansmatrisen för varje pixel och ersattes sedan rektangeln format filter med Gauss-formade filter. Denna detektor kan hitta kantpixlarna noggrant med mindre utelämnande. Därför skulle den vara ganska användbar för reduktion av brus, superpixel generation och andra tillämpningar.

Artikel 5 utforskar en oövervakad klassificeringsmetod av PolSAR data över stadsområden baserande på nedbrutna spridningskomponenter. Olika spridningskomponenters förmåga att urskilja jämförs och analyseras. Efter det används en oövervakande K-medel klassificerare för att diskriminera byggnader och naturområden. Orto- och orienterade byggnader kan särskiljas mycket väl. Baserat på artikel 4 föreslår artikel 6 en adaptiv superpixel generationensmetod för PolSAR data. När superpixen anses som objekt, kan en pixel-baserad klassificering förbättras ytterligare med den objektbaserad behandling.

Nyckelord: Polarimetrisk SAR, Spridningsnedbrytning, Upptäckt av artificiella objekt, Kantupptäckt, Superpixel, Urban klassificering

Acknowledgements

Table of contents

List of figures

List of tables

List of acronyms

SAR   - Synthetic Aperture Radar
PolSAR - Polarimetric Synthetic Aperture Radar
PolInSAR - Polarimetric Interferometric Synthetic Aperture Radar
LULC   - Land Use and Land Cover
SIRV   - The Spherically Invariant Random Vector
PDF   - Probability Density Function
SLC   - Single-Look Complex
MLC   - Multi-Look Complex
ENL   - Equivalent Number of Looks
CFAR   - Constant-False-Alarm-Rate
POA   - Polarization Orientation Angle
HV   - Cross-Polarized Scattering
GLCM   - Grey Level Co-Occurrence Matrix
ESAR   - Experimental Synthetic Aperture Radar
PALSAR - The Phased Array type L-band Synthetic Aperture Radar
AIRSAR - The NASA/JPL airborne SAR
UAVSAR - Uninhabited Aerial Vehicle Synthetic Aperture Radar
ALOS   - Advanced Land Observing Satellite
SDAN   - Span Driven Adaptive Neighbourhood
CPD   - Co-Polarized Phase-Difference
XPD   - Cross-Polarized Phase-Difference
Y4R   - Yamaguchi Four-Component Decomposition with
     Rotation of Coherency Matrix
MCSM   - Multiple-Component Model-Based Decomposition
$H/A/\overline{\alpha}$ - Entropy/Anisotropy/Averaged alpha angle
CoV   - Coefficient of Variation
ASA   - Achievable Segmentation Accuracy
BR   - Boundary Recall
SLIC   - Simple Linear Iterative Clustering

1 Introduction

An urban area is a location characterized by high population density and many built-up features in comparison to the areas surrounding it. In 1950, the number of people living in urban areas was only 746 million. But in 2014 there were 7.25 billion people living on the planet, of which the global urban population comprised 3.9 billion (United Nations Department of Economic and Social Affairs 2014). Fast process of urbanization with increasing population leads to socioeconomic and environmental problems, such as traffic jams, environmental pollution, construction huddle, etc (Zhang et al. 2011). Urban planning and development have a close relationship with the life of residents and the environment. Urban information extraction and analysis are essential to support sustainable decision making.

Synthetic Aperture Radar (SAR) is an active remote sensing technique capable of providing remote sensing imagery independent from solar illumination and to great extent unimpaired by weather conditions. It was previously designed only on airborne platforms and then implemented on various launched satellites, making it perform multi-polarization, multi-frequency, and multi-temporal acquisitions over global areas. Multi-polarization can be achieved by Polarimetric Synthetic Aperture Radar (PolSAR) system, which can obtain more information than SAR system with single-polarization. SAR and PolSAR have long been recognized as useful tools to exploit and analyse forest biomass information (Le Toan et al. 1992, 2011; Santoro et al. 2009, 2010), agriculture monitoring and mapping (Le Toan et al. 1997; Davidson et al. 2000; Bouvet et al. 2009), urban information such as disaster mitigation, damage assessment, land use and land cover (LULC) mapping, urban change detection, urban ground subsidence monitoring etc (Ulander et al. 2005; Voigt et al. 2005; Martinez et al. 2007; Dell'Acqua et al. 2001, 2003a, 2003b, 2006; Liao, Zhang, and Balz 2009; Ban et al. 2010; Soergel 2010; Ban and Yousif 2012; Ban and Jacob 2013; Chen and Sato 2013; Niu and Ban 2013a; Yamaguchi 2012; Ban et al. 2015; Minh et al. 2015; Cuong et al. 2015). In recent decades, when high resolution PolSAR data have become available with the launch of many advanced airborne and spaceborne SAR sensors such as Pi-SAR2, UAVSAR, TerraSAR-X, RADARSAT-2, and PALSAR-2, urban information extraction from PolSAR data has already become an attractive and promising topic not

only to academia but also to governmental authorities and user communities.

Nevertheless, there still exist a lot of challenges and problems remain unresolved. Until now, the Wishart distribution (Lee et al. 1995; Lee, Grunes, and Kwok 1994) seems to be the most widely used model in various statistical PolSAR image processing methods (Anfinsen, Eltoft, and Doulgeris 2009; Dabboor et al. 2013; Lee et al. 1999). However, the Wishart distribution is proved to be more effective for distributed targets (Lee and Pottier 2009; Soergel 2010). Therefore, it is mainly optimal to analyse natural targets. Regarding high-resolution PolSAR data, the basic assumption of this distribution that a high number of independent scatterers with comparable strength is contained in each cell would be wrong, especially in urban areas (Bombrun et al. 2011; Wu, Guo, and Li 2013; Wu, Guo, and Li 2015). Therefore, it is essential to find a statistical distribution which can accurately model the urban clusters in high resolution PolSAR data. Another challenge comes from the scattering analysis of urban areas, which makes it a difficult task for polarimetric decomposition (Chen, Li, and Wang 2014), man-made target detection (Ferro-Famil, Reigber, and Pottier 2005; Wu, Guo, and Li 2013), urban classification (Deng, Yan, and Sun 2015), etc. The urban environment is usually comprised of various natural and man-made targets with several kinds of materials, different orientations, various shapes and sizes, which complicate the backscattering discrimination and analysis (Niu 2012). During PolSAR imaging, buildings aligned along the radar flight direction can usually have double-bounce scattering. However, when the buildings do not align along radar flight direction, a significant cross-polarized component is produced, which can lead to confusion with forests (Ainsworth, Schuler, and Lee 2008; Yamaguchi 2012). Until now, this scattering ambiguity is still a challenge in PolSAR data interpretation.

Although many valuable techniques and promising results have been reported in recent studies (Yamaguchi 2012; Salehi, Sahebi, and Maghsoudi 2014; Susaki, Kajimoto, and Kishimoto 2014; Niu, Ban, and Dou 2015; Sieg 2015), detailed urban information extraction from high resolution PolSAR data is still a challenging task. In the meantime, the accuracies of current processing techniques for polarimetric scattering decomposition, man-made target detection, edge detection, and urban classification are still unsatisfactory and need to be improved urgently.

Therefore, evaluation of existing PolSAR data processing algorithms for urban analysis and the development of efficient approaches for detailed urban information extraction from airborne and spaceborne PolSAR data are of great importance for remote sensing applications. Regarding the method for urban information extraction in this thesis, there are three main parts, which are urban scattering analysis stage, urban extraction stage and urban classification stage, respectively. Specifically, the urban scattering analysis stage contains scattering analysis and model-based decomposition approaches. The urban extraction stage contains man-made target detection, edge detection and superpixel generation. The urban classification stage includes unsupervised pixel-based and object-based urban classification. Comparisons and analyses with other existing algorithms will be presented and discussed.

1.1   Research Objectives

This research mainly investigates airborne and spaceborne PolSAR data for detailed urban information extraction. Particular research objectives include the following:

- Exploit the scattering coherency model for urban areas with different orientation angles and develop model-based polarimetric decomposition algorithms.
- Investigate man-made target detection by incorporating target reflection asymmetry into azimuth nonstationarity extraction, removing natural areas and improving detection accuracy of small man-made targets and roads.
- Develop edge detection for PolSAR data, especially in the urban areas using the spherically invariant random vector (SIRV) product model and Gauss-shaped filter. Then the detected edges are utilized for superpixel generation and segmentation for PolSAR images.
- Analyse the discrimination ability of different scattering components. Investigate unsupervised urban area classification using scattering powers and further improve the result using superpixels.

In order to achieve the above objectives, six PolSAR datasets acquired with airborne and spaceborne sensors were used for evaluation and comparison.

1.2 Thesis Structure

This thesis is a collection of six papers with a summery organized into six chapters. Chapter 1 provides a short introduction to the thesis. The objectives of this research are defined and an overview of how the thesis is organised is given alongside the statement of contribution. The theory background and state of the art relevant studies are reviewed in Chapter 2. Chapter 3 presents the study areas and the description of PolSAR datasets. The proposed methods that were applied and developed are shown in Chapter 4. Chapter 5 gives the analyses and discussions of experimental results. Conclusions and suggestions for future research are presented in Chapter 6.

Below is the list of papers included in the thesis. The relationship between the listed papers is graphically illustrated in Figure 1.1.

[1] D. Xiang, Y. Ban and Y. Su. "Model-Based Decomposition With Cross Scattering for Polarimetric SAR Urban Areas," *IEEE Geoscience and Remote Sensing Letters*, vol. 12, no. 12, pp. 2496-2500, Dec. 2015.

[2] D. Xiang Y. Ban and Y. Su. "The Cross-Scattering Component of Polarimetric SAR in Urban Areas and Its Application to Model-Based Scattering Decomposition," *International Journal of Remote Sensing*, accepted, 2016.

[3] D. Xiang, T. Tang, Y. Ban and Y. Su. "Man-Made Target Detection from Polarimetric SAR Data via Nonstationarity and Asymmetry," *IEEE Journal of Selected Topics in Applied Earth Observations and Remote Sensing*, vol. 9, no. 4, pp. 1459-1469, Apr. 2016.

[4] D. Xiang, Y. Ban, W. Wang and Y. Su. "Edge Detector of Polarimetric SAR Images Using SIRV Model and Gauss-Shaped Filter," 2016. (*submitted to IEEE Geoscience and Remote Sensing Letters*).

[5] D. Xiang, T. Tang, Y. Ban, Y. Su, and G. Kuang. "Unsupervised Polarimetric SAR Urban Area Classification Based on Model-Based Decomposition with Cross Scattering*" ISPRS Journal of Photogrammetry and Remote Sensing*, vol. 116, pp. 86-100, 2016.

[6] D. Xiang, Y. Ban, W. Wang and Y. Su. "Adaptive Superpixel Generation for Polarimetric SAR Images with Local Iterative Clustering and SIRV Model," 2016. (*submitted to IEEE Transactions on Geoscience and Remote Sensing*).
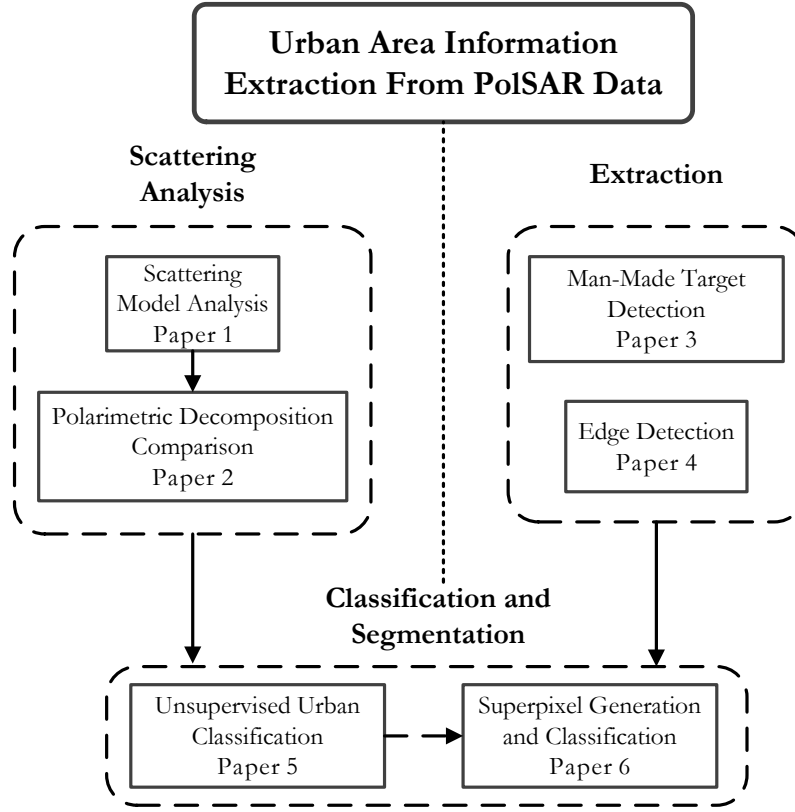
Figure 1.1 Relationship of the six papers

1.3   Statement of Contribution

Paper 1

All methodologies and analyses of paper 1 were developed and implemented by the main author under the supervision of Professor Ban, the 2nd author. Professor Su helped to improve the conception and analysis, and wrote part of the paper.

Paper 2

Deliang Xiang developed the ideas, performed the experiments and the analysis, and wrote the major part of the paper. Professor Ban initiated the experimental comparison using UAVSAR data. Professor Ban and Professor Su helped to edit the paper.

Paper 3

Deliang Xiang conceived and developed the ideas, performed the experiments and the analysis, and wrote the major part of the paper. Tao Tang, the 2nd author, helped implement the algorithm. Professor Ban and Professor Su helped to improve the conception and analysis, and edited the paper.

Paper 4

Deliang Xiang developed the ideas, performed the experiments and the analysis, and wrote the paper. Wei Wang helped to implement part of the algorithm. Professor Ban and Professor Su helped to improve the conception and analysis, and edited the paper.

Paper 5

The ideas, experiments and analysis were all developed by the main author Deliang Xiang. Tao Tang helped to write part of the paper. Professor Ban, Professor Su, and Professor Kuang helped to improve the conception and analysis, and edited the paper.

Paper 6

Professor Ban initiated the ideas for the paper. Deliang Xiang developed the ideas and performed the experiments. Wei Wang helped to implement part of the algorithm. Professor Ban and Professor Su helped to improve the conception and analysis, and edited the paper.

2 Theory Background and Literature Review

This chapter contains a detailed review of urban information extraction techniques using PolSAR data. The principles of PolSAR imagery, the existing polarimetric decomposition algorithms, man-made target detection approaches, statistical properties of PolSAR data, edge detection and superpixel generation methods, and urban area classification methodologies are reviewed in the following sections.

2.1 Polarimetric Radar Remote Sensing of Urban Areas

2.1.1 SAR Polarimetry Fundamentals

SAR imaging is a well-developed coherent and microwave remote sensing technique for providing large-scaled two-dimensional (2-D) high spatial resolution images of the Earth's surface reflectivity (Lee and Pottier 2009). Polarization is a fundamental property of electromagnetic waves, which is defined by orientations of the electric and magnetic field vectors. In this context, radar polarimetry is a technique that allows describing the properties of the target via changing the polarization state of electromagnetic waves (Antropov 2014; Jin and Xu 2013). In a full polarimetric SAR system, the transmitting and receiving antennas can be freely configured with two orthogonal polarization states. The general transformation from incident wave to backscattered wave can be described as (Zyl, Zebker, and Elachi 1987; Boerner, Mott, and Luneburg 1997)

$$
\begin{bmatrix} E_p^s \\ E_q^s \end{bmatrix} = \frac{e^{jkr}}{r} \mathbf{S} \begin{bmatrix} E_p^i \\ E_q^i \end{bmatrix} = \frac{e^{jkr}}{r} \begin{bmatrix} S_{pp} & S_{pq} \\ S_{qp} & S_{qq} \end{bmatrix} \begin{bmatrix} E_p^i \\ E_q^i \end{bmatrix} \tag{2.1}
$$

where (E_p^s, E_q^s) and (E_p^i, E_q^i) are the Jones vectors representing the backscattered and incident waves, respectively. $k = 2\pi / \lambda$ denotes the wave number and λ is the wavelength. r is the distance to the observation target. Scattering matrix $\mathbf{S}$, also called the Sinclair matrix, contains the information to interpret the scattering mechanisms, which is the fundamental measured entity in SAR polarimetry. The linear horizontal and vertical polarization basis are often used in $\mathbf{S}$ like

$$\mathbf{S} = \begin{bmatrix} S_{hh} & S_{hv} \\ S_{vh} & S_{vv} \end{bmatrix}. \tag{2.2}$$

Usually it can be expanded into the target scattering vector, represented in the Lexicographic format as

$$\mathbf{k}_{4L} = \begin{bmatrix} S_{hh} & S_{hv} & S_{vh} & S_{vv} \end{bmatrix}^{\mathrm{T}} \tag{2.3}$$

and the Pauli format as

$$\mathbf{k}_{4P} = \frac{1}{\sqrt{2}} \begin{bmatrix} S_{hh} + S_{vv} & S_{vv} - S_{hh} & S_{hv} + S_{vh} & j\left(S_{hv} - S_{vh}\right) \end{bmatrix}^{\mathrm{T}} \tag{2.4}$$

where the superscript T denotes the transpose. In the monostatic case (Henderson and Lewis 1998; Boerner, Mott, and Luneburg 1997), the reciprocity theorem can be applied and yields $S_{vh} = S_{hv}$, then the corresponding target scattering vectors could be redefined in the Lexicographic format as

$$\mathbf{k}_{3L} = \begin{bmatrix} S_{hh} & \sqrt{2}S_{hv} & S_{vv} \end{bmatrix}^{\mathrm{T}} \tag{2.5}$$

and the Pauli format as

$$\mathbf{k}_{3P} = \frac{1}{\sqrt{2}} \begin{bmatrix} S_{hh} + S_{vv} & S_{vv} - S_{hh} & 2S_{hv} \end{bmatrix}^{\mathrm{T}}. \tag{2.6}$$

These three-dimensional Lexicographic and Pauli target scattering vectors can be transformed into each other (Cloude and Pottier 1996; Lee and Pottier 2009). The Sinclair matrix $\mathbf{S}$ usually describes the information of the pure target exhibiting a particalar scattering mechnism. But in general, the earth features are more complicated or distributed with a variery of scattering responses. In such cases, the information obtained from $\mathbf{S}$ is insufficient to describe the physical properties of the surface. Based on the Sinclair matrix $\mathbf{S}$, the second order polarimetric representations of PolSAR data can be derived in form of the polarimetric covariance matrix $\langle [\mathbf{C}] \rangle$ as

$$\langle[\mathbf{C}]\rangle = \left\langle \mathbf{k}_{3\mathrm{L}}\mathbf{k}_{3\mathrm{L}}^{\dagger} \right\rangle = \begin{bmatrix} \left\langle |S_{hh}|^2 \right\rangle & \sqrt{2}\left\langle S_{hh}S_{hv}^* \right\rangle & \left\langle S_{hh}S_{vv}^* \right\rangle \\ \sqrt{2}\left\langle S_{hv}S_{hh}^* \right\rangle & 2\left\langle |S_{hv}|^2 \right\rangle & \sqrt{2}\left\langle S_{hv}S_{vv}^* \right\rangle \\ \left\langle S_{vv}S_{hh}^* \right\rangle & \sqrt{2}\left\langle S_{vv}S_{hv}^* \right\rangle & \left\langle |S_{vv}|^2 \right\rangle \end{bmatrix} \quad (2.7)$$

and coherency matrix $\langle[\mathbf{T}]\rangle$ as

$$\langle[\mathbf{T}]\rangle = \left\langle \mathbf{k}_{3\mathrm{P}}\mathbf{k}_{3\mathrm{P}}^{\dagger} \right\rangle$$

$$= \begin{bmatrix} \frac{1}{2}\left\langle |S_{hh}+S_{vv}|^2 \right\rangle & \frac{1}{2}\left\langle (S_{hh}+S_{vv})(S_{hh}-S_{vv})^* \right\rangle & \left\langle (S_{hh}+S_{vv})S_{hv}^* \right\rangle \\ \frac{1}{2}\left\langle (S_{hh}-S_{vv})(S_{hh}+S_{vv})^* \right\rangle & \frac{1}{2}\left\langle |S_{hh}-S_{vv}|^2 \right\rangle & \left\langle (S_{hh}-S_{vv})S_{hv}^* \right\rangle \\ \left\langle S_{hv}(S_{hh}+S_{vv})^* \right\rangle & \left\langle S_{hv}(S_{hh}-S_{vv})^* \right\rangle & 2\left\langle |S_{hv}|^2 \right\rangle \end{bmatrix} \quad (2.8)$$

where the superscript † denotes the complex conjugate transpose, * represents the complex conjugate only, $|\cdot|$ denotes the determinant and $\langle\cdot\rangle$ indicates spatial averaging, assuming homogeneity of the random scattering medium. The resulting second order polarimetric descriptors of the covariance and coherency matrices are able to better characterize distributed scatterers and are employed to extract physical information from the observed scattering process (Lee 2013). The relation between $\langle[\mathbf{C}]\rangle$ and $\langle[\mathbf{T}]\rangle$ is described in (Hajnsek, Pottier, and Cloude 2003). They are both 3×3 Hermitian positive semi-definite matrices, and contain the same information about the polarimetric scattering amplitudes, phase angles and correlations (Stefan 2014). Anyhow, $\langle[\mathbf{C}]\rangle$ is considered to be closer to the physical and geometrical scattering properties, whereas $\langle[\mathbf{T}]\rangle$ is directly related to the system measurables (Lee and Pottier 2009).

2.1.2 SAR Polarimetry for Urban Analysis

SAR data cannot provide complete urban scene information because radar systems operate on a single band of acquisition with single polarization. This limitation can be partly compensated by their increasingly available polarimetric capabilities (Treitz, Howarth, and

Soulis 1996). It has been proven that fully polarimetric SAR can provide detailed information on scattering mechanisms that could enable the complex targets or structures in the urban areas to be identified (e.g., buildings, bridges, ships, and other complex-shaped man-made targets) (Lee and Pottier 2009). Some semi-automatic procedures are already available providing outputs at a commercially acceptable level (Horn et al. 2007; Armando 2012).

Some examples of using PolSAR data for urban analysis can be found in a lot of articles. Most of the studies focus on urban area extraction (Schou et al. 2003; Kimura et al. 2004; Moriyama et al. 2004; Guillaso et al. 2005; Moriyama, Yamaguchi, et al. 2005; Ferro-Famil and Pottier 2007; Reigber et al. 2007; Ainsworth, Schuler, and Lee 2008; He et al. 2008; Wang et al. 2008; Guo, Li, and Zhang 2009; Wang, Tupin, and C. 2010; Zhang, Guo, et al. 2010; Li, Guo, et al. 2012; Kajimoto and Susaki 2013a; Deng and Wang 2014; Liu, Zhang, Liu, et al. 2014; Yang et al. 2014; Azmedroub and Ouarzeddine 2015; Wu, Guo, and Li 2015), urban density estimation (Iwasa and Susaki 2011; Cao, Su, and Liang 2012; Kajimoto and Susaki 2012, 2013b; Susaki, Kajimoto, and Kishimoto 2014), change detection (Li, Zhang, et al. 2012; Liu et al. 2012; Mishra and Susaki 2013; Xu et al. 2013; Lê et al. 2015; Xie et al. 2015), classification (Pellizzeri 2003; Iwasa and Susaki 2011; Bhattacharya and Touzi 2012; Niu and Ban 2013b; Salehi, Sahebi, and Maghsoudi 2014; De and Bhattacharya 2015; Deng, Yan, and Sun 2015), segmentation (Bombrun et al. 2011; Alonso-González, López-Martínez, and Salembier 2012; Lang et al. 2014; Cheng, Ji, and Liu 2015; Doulgeris 2015; Liu et al. 2015; Qin, Guo, and Lang 2015), and urban disaster assessment (Sato, Chen, and Satake 2012; Chen and Sato 2013; Susaki 2013; Zhao et al. 2013; Chen et al. 2015). Moreover, the interferometric capabilities of PolSAR, where available, allow the exploitation of terrain and man-made target height to improve the urban information extraction accuracy (Guillaso et al. 2003, 2005; Li et al. 2010; Antropov 2014; Sieg 2015). Since it is usually not easy to acquire the polarimetric interferometric SAR (PolInSAR) data over the regions of interest, PolSAR images are chosen by most of the urban information techniques.

Even though using PolSAR data to extract urban information seems promising, complexity still remains stemming from overlap of surface scattering, double bounce scattering, and triple- and higher-order bounce scattering from various components of man-made structures that make

physical interpretation a challenge (Lee and Pottier 2009). Therefore, there is still a lot of work to do for urban analysis using PolSAR data.

2.2 Polarimetric Target Decomposition

Polarimetric target decomposition is a powerful technique which can provide physical interpretations of the PolSAR observations such as scattering mechanisms or polarimetric properties. With this technique, an observed polarimetric matrix can be decomposed into a summation of several individual scattering mechanisms. The dominant scattering mechanism can be determined and physical parameters can be retrieved. Based on the decomposed parameters, a number of remote sensing applications, such as land use land cover classification (Qi et al. 2012; Chen, Kuang, et al. 2013), target detection (Deng and Wang 2014; Touzi 2007; Zhang, Zou, and Tang 2012), soil moisture estimation (Hajnsek et al. 2009), forest study (Antropov, Rauste, and Hame 2011a; Shimada 2011), ocean study (Schuler and Lee 2006), agriculture study (Merzouki, McNairn, and Pacheco 2010; Antropov, Rauste, and Hame 2011b), glacier study (Sharma et al. 2011), and disaster estimation (Sato, Chen, and Satake 2012; Chen and Sato 2013; Susaki 2013; Chen et al. 2015) were successfully applied. Over the past few decades, there have been a lot of polarimetric decomposition approaches proposed to interpret the scattering mechanisms present in PolSAR data (Cloude 2009; Lee and Pottier 2009; Zyl and J 2011). Polarimetric decomposition methods can be mainly divided into two major categories according to the assumptions of the target types, i.e., coherent target decomposition and incoherent target decomposition, which will be introduced in the following subsections. Moreover, the analysis of scattering mechanisms in urban areas will be discussed, followed by an overview of the state-of-the-art polarimetric model-based scattering decomposition methods.

2.2.1 Coherent Target Decomposition

In case of coherent decomposition, the scattering matrix is expressed as a weighted combination of scattering response of simple or canonical objects. The polarized scattered waves for which the scattering matrix holds the full polarimetric information can be completely characterized. These types of decompositions are applicable only to pure or coherent targets which give completely polarised backscatter (Cloude and Pottier 1996; Boerner, Mott, and Luneburg 1997). Thereby, the measured scattering matrix $\mathbf{S}$ can be expressed as

$$\mathbf{S} = \sum_{k=1}^{N} c_k \mathbf{S}_k \qquad (2.9)$$

where each scattering mechanism $\mathbf{S}_k$ stands for the scattering from a simple object weighted by a complex coefficient c_k. Therefore, the main goal of coherent decomposition is to interpret the physical properties through analysing the standard target contributions $\mathbf{S}_k$ (planes, dihedral, and helices). In the following, brief descriptions of three different coherent decomposition approaches are given, i.e., the Pauli (Cloude and Pottier 1996), the Krogager (Krogager 1990), and the Cameron (Cameron and Leung 1990) decompositions.

A. Pauli decomposition

The scattering matrix $\mathbf{S}$ is expressed as the complex sum of four scattering mechanisms, namely sphere surface, dihedral, di-plane oriented at 45 degrees and helix related, where each elementary scattering mechanism is associated with one Pauli basis matrix as the following

$$\mathbf{S} = \begin{bmatrix} S_{hh} & S_{hv} \\ S_{vh} & S_{vv} \end{bmatrix} = a[\mathbf{S}]_a + b[\mathbf{S}]_b + c[\mathbf{S}]_c + d[\mathbf{S}]_d \qquad (2.10)$$

$$[\mathbf{S}]_a = \frac{1}{\sqrt{2}}\begin{bmatrix} 1 & 0 \\ 0 & 1 \end{bmatrix} \qquad [\mathbf{S}]_b = \frac{1}{\sqrt{2}}\begin{bmatrix} 1 & 0 \\ 0 & -1 \end{bmatrix}$$
$$[\mathbf{S}]_c = \frac{1}{\sqrt{2}}\begin{bmatrix} 0 & 1 \\ 1 & 0 \end{bmatrix} \qquad [\mathbf{S}]_d = \frac{1}{\sqrt{2}}\begin{bmatrix} 0 & -j \\ j & 0 \end{bmatrix} \qquad (2.11)$$

where a, b, c, and d are all complex and given by

$$a = \frac{S_{hh} + S_{vv}}{\sqrt{2}}, b = \frac{S_{hh} - S_{vv}}{\sqrt{2}}, c = \frac{S_{hv} + S_{vh}}{\sqrt{2}}, d = j\frac{S_{hv} - S_{vh}}{\sqrt{2}} \quad (2.12)$$

In the monostatic case with the reciprocal assumption, where $S_{vh} = S_{hv}$, the Pauli matrix basis in Eq. (2.11) can be reduced to the first three matrices leading to $d = 0$. In general, the Pauli decomposition is usually used to display the PolSAR data with an image by a false colour scheme, i.e., Pauli coded image.

12

B. Krogager decomposition

The Krogager decomposition exploits the fact that any scattering matrix **S** can be uniquely represented as the combination of a sphere, a di-plane and a helix scattering model. In the linear orthogonal basis, the Krogager decomposition has the formulation as follows:

$$\mathbf{S} = e^{j\varphi}\left(e^{j\varphi s}k_s\left[\mathbf{S}\right]_s + k_d\left[\mathbf{S}\right]_d + k_h\left[\mathbf{S}\right]_h\right) \qquad (2.13)$$

where k_s, k_d and k_h correspond to the weights of the three scattering components, respectively. The main goal of the Krogager decomposition is to resolve different scattering characteristics independent from the incidence angles (Lee and Pottier 2009).

C. Cameron decomposition

In the Cameron decomposition, the scattering matrix **S** is decomposed using the Pauli matrices into the non-reciprocal part and the reciprocal part. The reciprocal part is further factorized into the max symmetric component and min symmetric component. Cameron decomposition emphasizes the importance of a class of symmetric targets that have linear Eigen polarizations on the Poincaré sphere and have a restricted target vector parameterization.

It should be noted that there are two problems with coherent decompositions (Lee and Pottier 2009). One is that the high speckle noise effect associated with SLC data is ignored in these types of decompositions, which will distort physical interpretation and scattering mechanisms of the coherent data. The second major problem is that there are many ways of decomposing a given scattering matrix **S** without a priori information, making it impossible to apply a unique decomposition.

2.2.2 Incoherent Target Decomposition

In general, the scattered wave is partially polarized and extracting physical parameters from a distributed target with incoherent scatterers is usually of more interest; moreover, to overcome the limitations of coherent decompositions, the incoherent target decomposition techniques were developed to represent the second order polarimetric representations of PolSAR data (such as covariance matrix $\langle[\mathbf{C}]\rangle$ or

coherency matrix $\langle [\mathbf{T}] \rangle$) into a sum of single scattering matrices. Incoherent target decompositions can provide a better interpretation of the underlying distributed scattering and simpler ways of extracting the physical parameters from the measured radar data (Cloude and Pottier 1996; Cloude 2009; Lee and Pottier 2009). Until now, there have been many incoherent target decomposition techniques proposed for PolSAR data, which can be mainly divided into two categories, i.e., eigenvalue-eigenvector-based decompositions and model-based decompositions.

A. Eigenvalue-eigenvector-based decomposition

Since the eigenvalue-eigenvector-based decomposition techniques have a clear mathematical background and only one decomposition solution, this kind of methods become relatively mature. Among them, entropy/anisotropy/averaged alpha angle ($H / A / \overline{\alpha}$) polarimetric decomposition is a typical representative which is based on the analysis of the eigenvectors and eigenvalues of the 3×3 Hermitian averaged coherency matrix $\langle [\mathbf{T}] \rangle$ (Cloude and Pottier 1997) with the form of

$$\langle [\mathbf{T}] \rangle = \sum_{i=1}^{3} \lambda_i \mathbf{\mu}_i \mathbf{\mu}_i^{\dagger} = \mathbf{T}_{01} + \mathbf{T}_{02} + \mathbf{T}_{03} \qquad (2.14)$$

where λ_i and $\mathbf{\mu}_i$ denote the *i*th eigenvalue and eigenvector respectively. Therefore, $\langle [\mathbf{T}] \rangle$ can be decomposed into the sum of three independent targets $\mathbf{T}_{01}, \mathbf{T}_{02}$, and $\mathbf{T}_{03}$, each of which indicating a deterministic scattering mechanism associated with an individual scattering matrix. Note that the eigenvalue λ_i determines the contribution from the *i*th deterministic scattering mechanism and $\mathbf{\mu}_i$ relates to the type of scattering (Cloude 1992; Cloude and Pottier 1997), which can be further expressed as

$$\mathbf{\mu}_i = e^{j\varphi_i} [\cos \alpha_i \quad \sin \alpha_i \cos \beta_i e^{j\delta_i} \quad \sin \alpha_i \sin \beta_i e^{j\gamma_i}]^{\mathrm{T}}. \quad (2.15)$$

Moreover, Cloude and Pottier defined entropy H , mean alpha angle $\overline{\alpha}$, and anisotropy A for the analysis of the physical information related to the scattering mechanisms of a medium as

14

$$H = -\sum_{i=1}^{3} p_i \log_3(p_i) \quad \text{with} \quad p_i = \frac{\lambda_i}{\sum_{k=1}^{3} \lambda_k} \qquad (2.16)$$

$$A = \frac{\lambda_2 - \lambda_3}{\lambda_2 + \lambda_3}, \quad \bar{\alpha} = \sum_{i=1}^{3} p_i \alpha_i. \qquad (2.17)$$

It should be noted that the entropy $0 \le H \le 1$ represents the randomness of a scattering medium between isotropic scattering ($H = 0$) and fully random scattering ($H = 1$). Specifically, when H is low, one dominant scattering corresponding to the largest eigenvalue can be extracted and the other eigenvalue components can be ignored whereas when H is high, a mixture of various types of scatterings should be considered. The mean alpha angle $\bar{\alpha}$ is related to the average scattering mechanisms from single-bounce scattering with $\bar{\alpha} = 0°$, dipole scattering with $\bar{\alpha} = 45°$, and double-bounce scattering with $\bar{\alpha} = 90°$. The anisotropy A is a complementary parameter to H, indicating the relative importance of the second and third eigenvalues. Polarimetric entropy, mean alpha angle, and anisotropy are widely used in a lot of studies for scattering mechanisms understanding (Ferro-Famil, E., and Lee 2001; Pellizzeri 2003; Cao et al. 2007; Deng and Wang 2014; Deng, Yan, and Sun 2015).

B. Model-based scattering decomposition

Compared to eigenvalue-eigenvector-based decompositions, model-based decompositions can obtain different decomposition results with various combinations of scattering models. The Freeman-Durden three-component decomposition (Freeman and Durden 1998) is the pioneer of incoherent model-based decompositions. It considers the covariance (or coherency) matrix as a combination of three scattering mechanisms, namely a volume scattering from a cloud of randomly oriented dipoles, double-bounce scattering from a pair of orthogonal surfaces with different dielectric constants, and surface scattering from a moderately rough surface. This decomposition process can be depicted using the covariance matrix as

$$\langle[\mathbf{C}]\rangle = f_v [\mathbf{C}]_v + f_d [\mathbf{C}]_d + f_s [\mathbf{C}]_s \qquad (2.18)$$

where f_v, f_d, and f_s correspond to the contributions of volume scattering component, double-bounce scattering component, and surface

scattering component, respectively. The volume, double-bounce, and surface scattering covariance matrices $[\mathbf{C}]_v$, $[\mathbf{C}]_d$, and $[\mathbf{C}]_s$ are given as

$$[\mathbf{C}]_v = \begin{bmatrix} 1 & 0 & 1/3 \\ 0 & 2/3 & 0 \\ 1/3 & 0 & 1 \end{bmatrix}, [\mathbf{C}]_d = \begin{bmatrix} |\alpha|^2 & 0 & \alpha \\ 0 & 0 & 0 \\ \alpha^* & 0 & 1 \end{bmatrix}, [\mathbf{C}]_s = \begin{bmatrix} |\beta|^2 & 0 & \alpha \\ 0 & 0 & 0 \\ \alpha^* & 0 & 1 \end{bmatrix}. (2.19)$$

This composite scattering model is widely used and has been proven to be effective to describe the polarimetric backscatter from natural scatterers. To improve the polarimetric decomposition performance in urban areas, a popular four-component model-based decomposition method was introduced (Yamaguchi et al. 2005; Yamaguchi, Yajima, and Yamada 2005). The helix scattering is added to address the co-pol and cross-pol correlations, which generally appears in complicated geometric scattering structures and disappears in natural areas. Therefore, this term is mainly relevant for modelling the scattering of man-made targets in urban areas. This four-component decomposition can be expressed as

$$\langle[\mathbf{C}]\rangle = f_v[\mathbf{C}]_{v(\theta)} + f_d[\mathbf{C}]_d + f_s[\mathbf{C}]_s + f_c[\mathbf{C}]_c \qquad (2.20)$$

where f_c is the contribution of helix scattering component and $[\mathbf{C}]_c$ is the helix scattering covariance matrix given by

$$[\mathbf{C}]_c = \frac{1}{4}\begin{bmatrix} 1 & -j\sqrt{2} & -1 \\ j\sqrt{2} & 2 & -j\sqrt{2} \\ -1 & j\sqrt{2} & 1 \end{bmatrix}. \qquad (2.21)$$

Nevertheless, model-based decompositions with models or assumptions that do not fit the actual observations may induce deficiencies, such as the negative powers solved for scattering mechanisms, overestimation or underestimation of volume scattering power, scattering mechanism ambiguities, etc (Chen, Li, and Wang 2014). Thereby, many advances have been proposed in the recent decades to improve the model-based decompositions, such as orientation compensation strategy (An, Cui, and Yang 2010; Lee and Ainsworth 2011; Yamaguchi et al. 2011), nonnegative eigenvalue constraint (Zyl, Arii, and Y. Kim 2011; Cui, Yamaguchi, and Yang 2014; Kusano, Takahashi, and Sato 2014), and

generalized scattering models (Freeman 2007; Arii, Zyl, and Kim 2011; Chen et al. 2014; Chen, Wang, and Sato 2014), etc. But until now, developing an effective and robust decomposition technique for PolSAR data is still a promising and challenging research topic, especially for urban areas with complicated scattering mechanisms.

2.2.3 Modelling and Interpretation of Scattering Mechanisms in Urban Areas

It is still difficult to extract urban information from PolSAR data due to the various orientation angles of buildings and the complex backgrounds, which can significantly influence the urban scattering mechanisms (Niu and Ban 2013b; Wu, Guo, and Li 2013; Deng and Wang 2014; Yang et al. 2014). As stated in many PolSAR interpretation studies, vegetation usually exhibits strong cross-polarized scattering (HV) (Lee and Pottier 2009). Since the scattering mechanisms of urban areas are related to the building orientation angles, buildings in PolSAR data can be divided into two categories, i.e., ortho buildings and oriented buildings. The former are buildings with walls perpendicular to the radar range direction while the latter buildings are not. The scattering reflection symmetry of oriented buildings is usually broken and the mixed polarization scattering terms can be quite large (Ainsworth, Schuler, and Lee 2008). Some studies pointed out that vegetation and oriented built-up areas both contribute to the HV scattering, which leads to scattering mechanism ambiguity between these two land covers (Sato and Yamaguchi 2012; Chen, Ohki, et al. 2013).

Another issue that needs to be raised is how to determine the scattering mechanism of oriented buildings. Many decomposition algorithms tried to identify the scattering of oriented buildings as double-bounce scattering, which is the same as that of ortho buildings (Shan, Zhang, and Wang 2012; Chen, Ohki, et al. 2013; Chen, Li, and Wang 2014; Chen et al. 2014; Chen, Wang, and Sato 2014; Chen et al. 2015). Nevertheless, it is not reasonable if all of the oriented buildings show double-bounce scattering like the ortho buildings after decomposition. On one hand, although oriented buildings and vegetation both generate cross-polarized scattering, they are not the same land cover. Thus it is not reasonable to use the volume scattering model designed for forests to describe the HV scattering from oriented buildings. On the other hand, the HV scattering of oriented buildings is not the same as the double-bounce scattering of ortho buildings. Therefore, the objective of polarimetric decomposition

should be urban scattering analysis and not to get pure double-bounce scattering for all of the buildings. Hence it is not enough to use double-bounce scattering model for polarimetric decomposition in urban areas. A new scattering model should be studied to describe the cross-polarized scattering component from oriented buildings.

Many model-based decomposition techniques have been studied over recent decades, among them, several approaches can be utilized for urban areas. Based on the four-component model-based decomposition (Yamaguchi et al. 2005; Yamaguchi, Yajima, and Yamada 2005; Yamaguchi et al. 2011), Sato and Yamaguchi (2012) proposed an extended volume scattering model for oriented urban areas. An et al. (2010) proved that the identity matrix is suitable for urban area decomposition for the reason that this scattering matrix can model pure volume scattering and be helpful to reduce the volume scattering overestimation in urban areas. Shan et al. (2012a, 2012b) utilized this matrix as the volume scattering model instead of the traditional ones in four-component decomposition. Moriyama et al. (2005) stated that in urban areas, surface, double-bounce, and cross scatterings are all significant. Furthermore, they proposed a new cross scattering matrix. Inspired by this theory, a new multiple-component model-based decomposition method for urban areas was proposed (Zhang et al. 2008). In this method, the wire scattering of built-up areas is analysed and then added to the Yamaguchi four-component model-based decomposition. The decomposition results in urban areas are improved and satisfactory. However, this method has a drawback, which is the underestimation of volume scattering in vegetated areas. A well-designed decomposition technique for urban areas should have the ability of reducing the HV scattering overestimation in oriented urban areas and underestimation in vegetated areas at the same time. Furthermore, the scatterings of ortho and oriented buildings should also be distinguished.

2.3 Man-Made Target Extraction from Urban Areas

Man-made target detection in urban areas is of high relevance for research on topics such as city expansion, construction monitoring, disaster damage evaluation, or some military applications such as target location and tracking (Yamaguchi 2012; Chen and Sato 2013; Zhao et al. 2013). For PolSAR data, it is challenging to extract man-made targets from complex built-up areas due to speckle effect and complex backscatter. This section will give an overview of widely used techniques

for man-made target detection first, and then followed by the scattering properties analysis, especially the target refection asymmetry.

2.3.1 Overview of Man-Made Target Detection Methods

Full polarization acquisition can enhance the radar capability in man-made target parameter (e.g., material, shape, and orientation) retrieval (Chen, Li, and Wang 2014). In general, many man-made targets with dominant double-bounce scattering, such as buildings aligned along radar flight direction, can be extracted effectively in the polarimetric dimension. However, when the buildings do not align along radar flight direction, a significant cross-polarized component is produced, which can lead to confusion with forests (Sato and Yamaguchi 2012; Shan, Zhang, and Wang 2012; Chen, Ohki, et al. 2013). Moreover, some small man-made targets such as metallic fences along the road are also very difficult to be extracted. In recent years, many effective algorithms have been proposed for man-made target extraction from PolSAR data. For instance, the phase-difference characteristics of urban areas for various orientation angles were analysed and an effective phase-difference parameter to detect buildings was proposed (Lee, Oh, and Kim 2012). In this method, co-polarized phase-difference (CPD) is adequate for aligned urban areas while cross-polarized phase-difference (XPD) is suitable for oriented urban areas with 45 degrees. Kajimoto and Susaki (2013a) proposed a novel building detection method that utilizes polarization orientation angle (POA), volume scattering power, and total power, where the POA randomness parameter between neighbouring pixels is used to discriminate urban areas from forest areas. Yang et al. (2014) utilized scattering mechanism-based statistical features from adaptive model decomposition (Arii, Zyl, and Kim 2011) to extract urban buildings. Xiao et al. (2014) maximized the correlation coefficient between two polarimetric channels by rotating a polarimetric coherence matrix in the rotation domain around the radar line of sight. Then the coherence of oriented man-made targets is enhanced while that of forests remains relatively low. It can be seen that these methods all concentrate on distinguishing oriented man-made targets from forest areas since these two land covers are easily misinterpreted by the model-based scattering decomposition techniques.

Nonstationarity analysis based on time-frequency decomposition is a useful tool in SAR and PolSAR image information extraction (Touzi et al. 2007; Spigai, Tison, and Souyris 2011). Complex man-made targets with anisotropic geometrical structures are illuminated from different

positions and may show changing electromagnetic characteristics (Ainsworth et al. 1999). More information can be provided for buildings not facing the radar and man-made targets can effectively be discriminated from forest areas. Based on this theory, an azimuth nonstationarity extraction method over the Wishart distribution was developed and then utilized to detect man-made targets from PolSAR data (Ferro-Famil et al. 2003; Ferro-Famil, Reigber, and Pottier 2005; Ferro-Famil and Pottier 2007; Reigber et al. 2007). To achieve better detection results, this method was further modified by employing Rician distribution and nonzero-mean statistical model instead of Wishart distribution, which are more suitable for high resolution PolSAR data (Wu, Guo, and Li 2013, 2014; Wu, Guo, and Li 2015). Although nonstationarity analysis can describe the anisotropic characteristic of man-made targets, there are some deficiencies, as stated in (Wu, Guo, and Li 2013). One reason is that anisotropy can also occur with other natural surfaces. For instance, cropland with Bragg resonance also exhibits the behaviour of a nonstationary target (Ulander et al. 1999; Ferro-Famil, Reigber, and Pottier 2005), resulting in some false alarms of the man-made target detection. Another reason is the number of sub-aperture images. A small number of sub-apertures cannot effectively describe the target anisotropy while a large number of sub-apertures can seriously degrade the image resolution, leading to the detection omissions of small man-made targets and roads.

2.3.2 Reflection Property of Man-Made Targets

Symmetry in the background usually leads to symmetries in the scattered field (Yueh, Kwok, and Nghiem 1994). Reflection symmetry makes the co- and cross-polarized scattering amplitudes uncorrelated (Nghiem et al. 1992). As a result, this important reflection property, becomes robust and independent of any particular assumed scattering mechanism (Nunziata, Migliaccio, and Brown 2012). Symmetry in electromagnetics was first exploited to discriminate targets in Baum (1997) and Baum (2003). There have been a lot of studies demonstrating that backscatter from natural areas is often reflection symmetric; i.e., characterized by near zero values for coherency matrix off-diagonal elements and their conjugates due to $\left\langle S_{hv} S_{hh}^{*} \right\rangle \approx \left\langle S_{hv} S_{vv}^{*} \right\rangle \approx 0$ (Yueh, Kwok, and Nghiem 1994). In contrast, backscatter from complex man-made structures in urban areas often occurs from different geometries and, therefore, reflection symmetry is often broken (Ainsworth, Schuler, and Lee 2008; Nunziata, Migliaccio, and Brown 2012; Yamaguchi et al. 2005; Kimura et

al. 2004; Zou et al. 2015). The coherency matrix mixed polarization terms (e.g., T_{13}, T_{23}, and their conjugates) can be quite large for these scattering cases, which was also discussed in (Yamaguchi et al. 2005; Yamaguchi, Yajima, and Yamada 2005) and (Ferro-Famil and Lavalle 2009). Nunziata et al (2012) and Migliaccio et al. (2011) developed a symmetry-based detector in a processing chain to provide two added-value products: sea oil slick maps and metallic targets at sea maps. Ainsworth et al. normalized the conventional RR-LL correlation coefficient by a circular-pol RR-LL correlation coefficient (Ainsworth, Schuler, and Lee 2008), which was constructed from the same covariance or coherency matrix terms, but with the mixed terms $\langle S_{hv} S_{hh}^* \rangle, \langle S_{hv} S_{vv}^* \rangle$ artificially set to zero, i.e. reflection symmetry. This normalized circular-pol correlation coefficient can effectively detect scattering from reflection asymmetric structures. Nevertheless, the man-made target details are reduced, which may omit the small targets and roads. Wang et al. derived the statistical models of the magnitude of the (2, 3) term in the coherency matrix within different degrees of homogeneity and proposed an automatic constant-false-alarm-rate (CFAR) detection scheme. This detector has the capability of detecting non refection symmetry ships, oil stores, buildings, etc., in homogeneous and heterogeneous areas (Wang et al. 2012). Therefore, the reflection property of man-made targets has a great potential ability for detection.

2.4   PolSAR Edge Detection and Superpixel Generation

2.4.1   Statistical Properties of PolSAR Data

The statistics of PolSAR data are usually based on the analysis of SAR speckle. Speckle of SAR images results from the coherent interference of waves reflected from many elementary scatterers (Goodman 1976). A random walk model was utilized to describe the scattering process (Touzi 2002; Goodman 2007), which describes the measured electromagnetic wave as a vector sum of the wave components by the scatters in the same resolution cell. The speckle leads to a pixel-to-pixel variation which is represented as a granular speckle pattern on the SAR image. Understanding the speckle statistics of SAR and PolSAR data is essential for better information extraction by designing robust algorithms for speckle filtering, geophysical parameter estimation, target detection, classification and segmentation, etc (Lee and Pottier 2009). In this section, the speckle statistics of a single polarization SAR will be discussed first, followed by the statistics of PolSAR data. The complex

Wishart distribution for the polarimetric covariance or coherency matrices will be emphasized and some more complex distributions which better describe the heterogeneous urban areas will be further discussed.

A. Speckle statistics of a single polarization SAR

A single polarization observation A can be formed as the product of two independent components: speckle Z and texture τ (Oliver and Quegan 2004) like

$$A=\sqrt{\tau}Z, \quad I=\tau P, \quad P=|Z|^2 \tag{2.22}$$

where A and I denote the amplitude and intensity of the SAR observation, respectively. Texture τ indicates the ideal scattering of the target and Z is a complex random variable representing the amplitude of speckle. P denotes the speckle intensity. For single-look SAR data, P follows the negative exponent distribution as (Lee and Pottier 2009)

$$f(p)_P=\frac{1}{\pi}\exp(-p), \qquad (p>0) \tag{2.23}$$

whereas for multi-look SAR data, P follows a Gamma distribution as

$$f(p\,|\,L)_P=\frac{L^L}{\Gamma(L)}p^{L-1}\exp(-Lp), \quad (L, p>0) \tag{2.24}$$

where L is the equivalent number of looks (ENL) of SAR data, and $\Gamma(\cdot)$ is the gamma function. With the above product model and speckle distribution, we can derive various intensity distributions for multi-look SAR data by assuming different texture distributions, as shown in Table 2.1.

According to the degrees of homogeneity, these intensity distributions could be used to model the backscatter of different types of classes. For instance, pasture is usually more homogeneous than forest and urban areas and can be modelled by the Gamma distribution. For forest, the K distribution is better since it is derived based on a physical scattering process (Jakeman 1980) and it can reduce to the Rayleigh distribution in the case of homogeneous media (Lee, Hoppel, et al. 1994; Lee and Pottier 2009). However, to model extremely heterogeneous clutter, such

as urban areas, the K distribution cannot work very well and G_0 distribution is more appropriate (Frery et al. 1997). To further model the cluster of very high-resolution SAR images over urban areas, the Fisher distribution seems to be better (Tison et al. 2004).

Table 2.1: Texture distributions and the corresponding SAR intensity distributions

Intensity (Texture) distributions	Intensity Probability Density Function (PDF)
Gamma (Constant)	$f(I \mid \lambda, \alpha) = \dfrac{\lambda^{\alpha}}{\Gamma(\alpha)} I^{\alpha-1} \exp(-\lambda I)$
K (Gamma)	$f(I \mid \mu, \alpha) = \dfrac{2L\alpha}{\Gamma(L)\Gamma(\alpha)\mu} \left(\dfrac{L\alpha I}{\mu} \right)^{(\alpha+L)/2-1} K_{\alpha-L}(2\sqrt{\dfrac{\alpha LI}{\mu}})$
G_0 (Inverse Gamma)	$f(I \mid \mu, \lambda) = \dfrac{L^{L}\Gamma(L+\lambda)\left((\lambda-1)\mu\right)^{\lambda} z^{L-1}}{\Gamma(L)\Gamma(\lambda)\left(LI+(\lambda-1)\mu\right)^{L+\lambda}}$
Fisher (F distribution)	$f(I \mid l, m, \mu) = \dfrac{\Gamma(l+m)}{\Gamma(l)\Gamma(m)} \dfrac{l}{m\mu} \dfrac{\left(\dfrac{lI}{m\mu} \right)^{l-1}}{\left(1 + \dfrac{lI}{m\mu} \right)^{l+m}}$

B. Statistics of PolSAR data

The statistical characteristics of PolSAR data are not limited to the intensities or amplitudes. Speckle noise not only appears in the HH, HV, and VV intensity images, but also appears in the complex cross product terms between different polarizations (Lee and Pottier 2009). By using the product model, the single-look complex (SLC) target scattering vector **k** can be decomposed as (Freitas, Frery, and Correia 2005)

$$\mathbf{k} = \sqrt{\tau}\mathbf{Z} \tag{2.25}$$

where **Z** is a complex random vector following a zero mean multivariate complex Gaussian distribution (Goodman 1963). Therefore, the multi-look complex (MLC) covariance or coherency matrix can be written as

$$\langle[\mathbf{C}]\rangle \ or \ \langle[\mathbf{T}]\rangle = \langle\mathbf{k}\mathbf{k}^{\dagger}\rangle = \tau\langle\mathbf{Z}\rangle. \tag{2.26}$$

The average complex speckle $\langle \mathbf{Z} \rangle$ obeys a scaled multivariate complex Wishart distribution (Goodman 1963; Srivastava 1965; Lee, Schuler, et al. 1994; Lee, Hoppel, et al. 1994) with density given by

$$f_{\langle \mathbf{z} \rangle}(\mathbf{z}) = \frac{L^{Ld} |\mathbf{z}|^{L-d} \exp(-L\mathrm{Tr}(\Sigma^{-1}\mathbf{z}))}{h(L,d)|\Sigma|^L} \qquad (2.27)$$

where $\mathrm{Tr}(\cdot)$ denotes the trace and d is the dimension of $\mathbf{k}$. The scaling function $h(L,d)$ is given by $h(L,d) = \pi^{d(d-1)/2}\Gamma(L)\cdots\Gamma(L-d+1)$ and $\Sigma = \mathrm{E}(\mathbf{kk}^\dagger) = \mathrm{E}(\mathbf{ZZ}^\dagger)$. Therefore, various distributions for PolSAR MLC covariance or coherency matrix can be derived by assuming different texture distributions. Table 2.2 presents some common distributions formed in this way.

Table 2.2. Texture distributions and the corresponding PolSAR distributions

PolSAR (Texture) distributions	*Probability Density Function (PDF) of the covariance matrix*
Wishart (Constant)	$f(\mathbf{C}\|\Sigma,L) = \dfrac{L^{Ld}|\mathbf{C}|^{L-d}\exp(-L\mathrm{Tr}(\Sigma^{-1}\mathbf{C}))}{\Gamma_d(L)|\Sigma|^L}$
K (Gamma)	$f(\mathbf{C}\|\Sigma,L,\alpha) = \dfrac{2|\mathbf{C}|^{L-d}(L\alpha)^{\frac{\alpha+Ld}{2}}(\mathrm{Tr}(\Sigma^{-1}\mathbf{C}))^{\frac{\alpha-Ld}{2}}}{\Gamma_d(L)|\Sigma|^L\Gamma(\alpha)}$ $\cdot K_{\alpha-Ld}(2\sqrt{L\alpha\mathrm{Tr}(\Sigma^{-1}\mathbf{C})})$
G_0 (Inverse Gamma)	$f(\mathbf{C}\|\Sigma,L,\lambda) = \dfrac{L^{Ld}|\mathbf{C}|^{L-d}\Gamma(Ld+\lambda)(\lambda-1)^\lambda}{\Gamma_d(L)|\Sigma|^L\Gamma(\lambda)}$ $\cdot(L\mathrm{Tr}(\Sigma^{-1}\mathbf{C})+\lambda-1)^{-\lambda-Ld}$
KummerU (F distribution)	$f(\mathbf{C}\|\Sigma,L,\xi,\zeta) = \dfrac{L^{Ld}|\mathbf{C}|^{L-d}}{\Gamma_d(L)|\Sigma|^L}\dfrac{\Gamma(\xi+\zeta)}{\Gamma(\xi)\Gamma(\zeta)}(\dfrac{\xi}{\zeta-1})^{Ld}\Gamma(Ld+\zeta)$ $\cdot U(Ld+\zeta,Ld-\xi+1,L\mathrm{Tr}(\Sigma^{-1}\mathbf{C})\xi/(\zeta-1))$

As a classic statistical model, the Wishart distribution has been widely used in various PolSAR image processing techniques (Lee, Grunes, and Kwok 1994; Lee et al. 1999; Ferro-Famil, E., and Lee 2001; Schou et al. 2003; Anfinsen, Eltoft, and Doulgeris 2009; Dabboor et al. 2013; Silva et al. 2013; Frery, Nascimento, and Cintra 2014). It has been demonstrated

that the Wishart distribution can perform very well for low resolution PolSAR data. However, with the new PolSAR sensors, the number of scatterers present in each resolution cell decreases considerably, which makes the assumption that PolSAR clutter is homogeneous easily be violated. To overcome this difficulty, the K distribution was introduced to model the PolSAR data, which has shown promising results in the forested scenes (Lee, Schuler, et al. 1994). Compared to the K distribution, the G_0 and the KummerU distributions can be able to fit an extremely heterogeneous clutter, such as the urban areas (Bombrun and Beaulieu 2008; Bombrun et al. 2011; Khan and Guida 2014).

2.4.2 Review of Edge Detection Methods

Edge detection of PolSAR data is essential for various applications, e.g., speckle noise reduction (Lang, Yang, and Li 2015), superpixel segmentation (Lang et al. 2014; Qin, Guo, and Lang 2015) and so on. Extracting edges of urban buildings can be helpful for urban planning and urban mapping. In simple terms, the purpose of PolSAR edge detection is to identify boundaries between regions with different polarimetric information, as well as structural characteristics (Nascimento et al. 2014).

There have been several algorithms proposed for PolSAR edge detection. On the basis of ratio edge detector for SAR images (Fjortoft et al. 1998), a new approach to edge detection in PolSAR data using a statistical test for equality of complex covariance matrices following a complex Wishart distribution was proposed (Schou et al. 2003). Zhou et al. (2011) proposed a two-scale edge detection method, consisting of a coarse level and a fine level. The former extracts the linear features using a curvelet transform and the latter accurately locates the linear features via a fuzzy polarimetric detector. Under the scaled complex Wishart distribution, Frery et al. (2014) and Nascimento et al. (2014) compared the performances of four stochastic distances, two differences of entropies, and the maximum likelihood criterion on PolSAR edge detection. Liu et al. (2014) presented a degenerate filter design integrated with the weighted maximum likelihood estimation to overcome the limitation of the traditional constant-false-alarm-rate (CFAR) edge detector. After that, Liu et al. (2015) further proposed a multiscale edge detection method based on wedgelet analysis for PolSAR images to capture the local geometrical information. Lang et al. (2015) analysed the line features in PolSAR data and proposed a line-and-edge detector on the basis of traditional CFAR edge detector, which can detect both lines and edges.

Most of these methods are developed under the assumption of complex Wishart distribution. However, in heterogeneous urban areas, this assumption is usually violated (Bombrun and Beaulieu 2008; Soergel 2010; Bombrun et al. 2011). In the meantime, it is quite difficult to find a particular distribution to describe the backscatters of urban areas since they are extremely complex (Wu, Guo, and Li 2015; Liu, Zhang, Wang, et al. 2014). Therefore, the edge detection for heterogeneous urban areas still remains unsolved.

2.4.3 Superpixel Generation Methods for PolSAR Data

A superpixel is defined as a local region which preserves most of the object information and well adheres to object boundaries (Li and Lu 2011; Xiang et al. 2013). Superpixels are approximately regular in size and shape just like pixels, especially in homogeneous regions. They have actively been used for a wide range of applications such as classification (Cheng, Liu, and Xu 2013), segmentation (Liu et al. 2011) and stereo matching or tracking. Until now, numerous superpixel algorithms have been proposed for optical images, among them the simple linear iterative clustering (SLIC) method is popular and shows good performance in superpixel generation (Achanta et al. 2012). In contrast, there are very few superpixel generation approaches proposed for SAR and PolSAR images. Some existing superpixel algorithms such as Meanshift (Comaniciu and Meer 2002) and Turbopixel (Levinshtein et al. 2009) originally designed for optical images were adopted for SAR and PolSAR image classification (Su et al. 2011). Xiang et al. (2013) developed a novel superpixel generation algorithm based on pixel intensity and location similarity, which modified the similarity measure of SLIC to make it applicative for SAR images. For PolSAR data, Liu et al. (2013) incorporated the revised Wishart distance and edge map into the Normalized cuts (Shi and Malik 2000) algorithm to produce superpixels. On the basis of SLIC, Feng et al. (2014), Song et al. (2015), and Qin et al. (2015) utilized the symmetric revised Wishart distance, Bartlett distance and revised Wishart distance respectively as the similarity measures instead of the original one to generate superpixels. In (Qin, Guo, and Lang 2015), the PolSAR edge map obtained by traditional CFAR edge detector (Schou et al. 2003) was introduced to replace the simple gradient calculation. It can be seen that these methods are all designed based on the assumption of Wishart distribution, which can well model the backscatter of natural areas. However, for heterogeneous urban areas, this assumption is usually violated, making the superpixels not well adhere to urban boundaries and preserve the polarimetric features. In the

meantime, it is quite difficult to find a particular distribution to describe the backscatters of urban areas since they are extremely complex. Therefore, superpixel generation for PolSAR images, especially in heterogeneous urban areas, still remains unsolved. Another drawback of these methods lies in the non-adaptive selection of the trade-off factor, which balances polarimetric similarity and spatial proximity while simultaneously providing control over the shape and compactness of the superpixels. This parameter is usually set manually by trial and error, which might cause over- or under-segmentation in some spatially complex areas.

2.5 Urban Area Classification Using PolSAR Data

State of the art urban area classification methods using PolSAR data will be reviewed in the next subsection, followed by the discussion of the challenges in this research field.

2.5.1 Pixel- and Object-based Classification

The classification of PolSAR images has become an important research topic since a lot of airborne and spaceborne PolSAR data are available. The remote sensing image classification methods can be defined as pixel-based or object-based according to whether the basic processing element is either a single pixel or a segment. Many classification methods for SAR and PolSAR data have been explored with pixel-based strategies (Rignot, Chellappa, and Dubois 1992; Chen, Huang, and Amar 1996; Barnes and Burki 2006; Gamba P et al. 2006; Shimoni et al. 2009; Dell'Acqua et al. 2009; Niu and Ban 2012, 2013b, 2014; Niu et al. 2015). Recently, on the basis of various polarimetric decomposition theorems, classification methods based on decomposition results have been explored (Lee, Grunes, and Kwok 1994; Cloude and Pottier 1997; Lee et al. 1999; Cao et al. 2007; Wang et al. 2013). These scattering features cover the H/alpha, the Yamaguchi, the Neumann, the Huynen, the Krogager, and the Cameron decomposition results, etc. Moreover, some studies have indicated that the fusion of physical and textural information derived from various SAR polarizations is helpful in improving classification results. Tu et al. (2012) utilized Pauli, Krogager, Cloude, Freeman-Durden, and Huynen decomposition scattering powers, as well as co-polarized, cross-polarized backscattering coefficients, phase difference, depolarization ratio and the degree of polarization polarimetric signatures for PolSAR image classification. Zhang et al. (2010) used the multiple component decomposition powers and gray

level co-occurrence matrix (GLCM) texture features to classify ESAR image. However, there exist some deficiencies in these pixel-based classification methods. On one hand, utilizing the textural and spatial information of PolSAR images through pixel-based methods is difficult. On the other hand, the results of pixel-based methods are insufficient for extracting objects of interest and can be easily influenced by speckle noise (Niu 2012).

Compared with pixel-based image classification methods, object-based classification is a promising scheme. After segmenting images under some constraints such as intensity, location, texture, and edge, many homogeneous regions can be obtained, and then classification is based on these regions instead of pixels. Xiang et al. (2013) proposed a superpixel generating algorithm based on pixel intensity and location similarity for SAR image and extracted the Gabor filters and GLCM from each superpixel for classification. The results are less affected by speckle and the computational cost is lower. Hu and Ban (2012) investigated the potential of very high resolution SAR data for urban mapping using the object-based approach. Qi et al. (2012) proposed a novel object-based classification method for RADARSAT-2 data using polarimetric decomposition, PolSAR interferometry and image texture information. Esch et al. (2010) developed an object-based approach to depict the urban footprints using TerraSAR-X data. Niu and Ban (2013a) investigated object-based support vector machine urban land-cover classification for multi-temporal PolSAR data. Ban and Jacob (2013) developed an edge-aware region growing and merging algorithm for segmentation of multitemporal SAR and optical data for detailed urban land-cover mapping. Deng et al. (2014) developed a new effective hierarchical segmentation method for multitemporal ultrafine-beam SAR data in urban areas. Ban et al. (2015) evaluated spaceborne SAR data for improved global urban mapping using the KTH-Pavia Urban Extractor, which is also an object-based method. So far, most studies have focused on the classification of single or dual polarization SAR data with coarse categories of only one or few urban classes. There is still a lack of studies on detailed urban classification using PolSAR data.

2.5.2 Challenges in Urban Area Classification with PolSAR

We have discussed the classification strategy using decomposed scattering components in the previous subsection. However, there are some misclassifications. Some land covers belong to different classes but may have the same scattering mechanism. Some land covers within the

same class but can have different scattering mechanisms (Kajimoto and Susaki 2013a; Deng and Wang 2014). Moreover, because many objects are sensitive to the polarization orientation angle during imaging, a set of features with a very small number of polarimetric signatures, from one to four parameters, are not enough for terrain classification.

To resolve this issue, a wide variety of polarimetric features are used, including the decomposition powers and several polarimetric indexes such as backscattering coefficients of different polarizations (linear: HH, HV, VV; circular: LL, RR, RL; and linear 45°, 45C, 45X), and their ratios. In addition to polarimetric information, some studies on PolSAR image classification are also proposed from the prospects of image understanding, indicating the effectiveness of image texture on classification (Qi et al. 2012). However, with the addition of polarimetric, interferometric, textural, and spatial information, hundreds of features can potentially be incorporated into the classification of PolSAR images, resulting in feature information redundancies. For instance, the Krogager rotation angle is relative to the polarization orientation angles and the H/alpha parameters describe the chaotic volume scattering, which is also considered in the Freeman-Durden methods, etc. These information redundancies may lead to confusion for classifier and decrease the classification accuracy. Therefore, feature selection is quite import and needs to be considered.

The detailed discrimination of urban areas, e.g., high/low density urban classification and ortho/oriented building classification, is also an important problem. Urban spaces are rapidly becoming extremely dense, especially in some Asian countries. To understand the details of urban areas, urban density classification can be one of the effective methods (Niu 2012; Niu and Ban 2012, 2013a, 2013b, Niu et al. 2015). Even though using PolSAR data for urban density classification could be a useful method, it has not been practical because of the complex scattering mechanisms of urban areas (Iwasa and Susaki 2011; Kajimoto and Susaki 2013b; Susaki, Kajimoto, and Kishimoto 2014). In terms of ortho/oriented building classification, most of the classification methods regard the ortho and oriented buildings as the same class. However, they depict different scattering mechanisms in PolSAR image and should be regarded as different classes. This point will be focused in this thesis.

3 Study Areas and Data Description

3.1 Study Areas

Since this thesis focuses on urban information extraction, all of the study areas cover cities including Tsukuba in Japan, Oberpfaffenhofen in Germany, San Francisco Bay in USA, Long Beach in USA, and Southern California Coast in USA.

Tsukuba is a city located in Ibaraki Prefecture, in the northern part of Japan. This city has an estimated population of 223,151 and a population density of 787 persons per square kilometres. Oberpfaffenhofen is a village which is part of Bavaria in Germany. It is 20 kilometres from the city centre of Munich. This village is home to a major site of the German Aerospace Centre (DLR) and became hence known to a wide audience. Eight scientific institutes are located in this site and the current population approximates 1700. There are a lot of buildings and an airport here, which makes this site suitable for urban target detection and scattering analysis (Shan, Zhang, and Wang 2012; Zhang, Zou, and Tang 2012). San Francisco Bay is in the U.S. state of California, surrounded by a contiguous region known as the San Francisco Bay Area, dominated by the large cities San Francisco, Oakland, and San Jose. The waterway entrance to San Francisco Bay from the Pacific Ocean is called the Golden Gate. Across the strait spans the Golden Gate Bridge. The buildings and Golden Gate Bridge can be helpful for urban scattering analysis (Zhang, Zou, and Tang 2012; Deng and Wang 2014; Deng, Yan, and Sun 2015). Long Beach is a city in Los Angeles County in Southern California, on the Pacific coast of the United States. The city is the 36th-largest city in the United States and the seventh-largest in California. As of 2010, its population was 462,257. In addition, Long Beach is the second largest city in the Greater Los Angeles Area and a principal city of the Los Angeles metropolitan area. The Port of Long Beach is the United States' second busiest container port and one of the world's largest shipping ports. Therefore, this study area has coverage of different types of land covers and should be suitable for urban area classification. The South Coast is a term used in the West Coast region of the United States to refer to both the south Pacific Coast of California and the adjacent resort and residential communities. This area also covers buildings, sea, and farms and therefore is good for urban scattering analysis (Bhattacharya et al. 2015).

3.2 Data Description

3.2.1 PolSAR Data

Both airborne and spaceborne PolSAR data acquired with different frequencies and resolutions were used throughout the studies. Table 3.1 summarizes all datasets and Figure 3.1 shows the corresponding Pauli coded images used in this thesis, where the definition of Pauli coded is described in Section 2.2.1.

Table 3.1 Overview of the PolSAR data that was used in this thesis including instrument, spatial resolution, band, and acquisition period.

Paper	Instrument	Band (resolutions)	Acquisition date
1, 2, 5	AIRSAR	C/L (9.26 m)	1995/04/07
1, 2, 5	RADARSAT-2	C (5 m)	2008/04/09
2	UAVSAR	L (7.2 m)	2014/11/20
3	PALSAR	L (9.36 m)	2009/11/11
4, 6	PiSAR	L (3 m)	1997/09/30
3, 4, 6	ESAR	L (3 m)	1999/07/20

AIRSAR

The NASA/JPL airborne SAR (AIRSAR) system can operate in fully polarimetric mode at P-, L- and C-band or in the interferometric mode in both L- and C-band. This system became operational in late 1987 and flew its first mission aboard a DC-8 aircraft in Mountain View, California. Since then, the AIRSAR system has flown missions every year and acquired a huge amount of data in North, Central and South America, Europe and Australia. The AIRSAR data are usually processed to 9 looks or 18 looks with a resolution of about 5 meters and 10 meters, respectively. The data in this thesis was acquired with C band and has a resolution of about 10 meters.

RADARSAT-2

RADARSAT-2 is an Earth observation satellite that was launched on December 14, 2007 for the Canadian Space Agency. This satellite has a SAR with multiple polarization modes, including a fully polarimetric mode. Its highest resolution is 1 meter in Spotlight mode (3 meters in Ultra Fine mode). The SAR data used in this thesis is the fine-beam polarimetric SAR data. The centre frequency at this beam mode is 5.4GHz, i.e., C-band, and the pixel spacing is 4.7 meters in the range direction and 5.1 meters in the azimuth direction.

UAVSAR

UAVSAR is an airborne SAR system with L-band, which firstly acquired data on 18 September 2007. Since 2009, over 1,800 flight lines have been acquired during more than 160 flights, acquiring over 40 terabytes of raw signal data. These data have already been used in various remote sensing applications (Migliaccio, Nunziata, and Buono 2015; Collins et al. 2015). UAVSAR can provide high-resolution, fully-polarimetric data products. The single look complex data have a pixel spacing of 0.6 m in azimuth direction and 1.6 m in range direction. Usually the available products are 36-look slant-range polarimetric products at 5 m x 7.2 m pixel spacing.

PALSAR

The Phased Array type L-band Synthetic Aperture Radar (PALSAR) is an active microwave sensor using L-band frequency to achieve cloud-free, day-and-night land observation. PALSAR was one of three instruments on the Advanced Land Observing Satellite-1 (ALOS-1), developed to contribute to the fields of mapping, precise regional land-coverage observation, disaster monitoring, and forest surveying. ALOS-1 was a mission of the Japan Aerospace Exploration Agency (JAXA). This spaceborne sensor can provide higher performance than the JERS-1 SAR. Apart from the conventional mode, PALSAR has another observation mode, i.e., ScanSAR, which will enable us to acquire a SAR image with 250 to 350km swath width. In addition, it also provides the polarimetric mode. In this thesis, the SAR data have the nominal pixel spacing of 9.36 and 3.54 meters in the range and azimuth directions respectively.

PiSAR

The Pi-SAR system is a dual-frequency airborne polarimetric and interferometric SAR imaging sensor. The frequencies of this system are X-band (9.55GHz) and L-band (1.27GHz), where the X-band SAR was developed by the National Institute of Information and Communication Technology (NICT), and the L-band SAR by Japan Aerospace Exploration Agency (JAXA) (Uratsuka et al. 2010). The resolution for the X-band radar is 1.5 meters and for the L-band it is 3 meters. Both X-band and L-band systems have polarimetry function. Experiments and observations using this PolSAR system have been carried out in Japan since 1995. The observations have been applied in various remote sensing areas such as urban analysis, forestry and agriculture monitoring, disaster damage assessment, oceanography etc.

(a) PiSAR
(Tsukuba)

(b) ESAR
(Oberpfaffenhofen)

(c) AIRSAR
(Long Beach of California)

(d) UAVSAR
(Southern California Coast)

(e) PALSAR
(San Francisco Bay)

(f) RADARSAT-2
(San Francisco Bay)
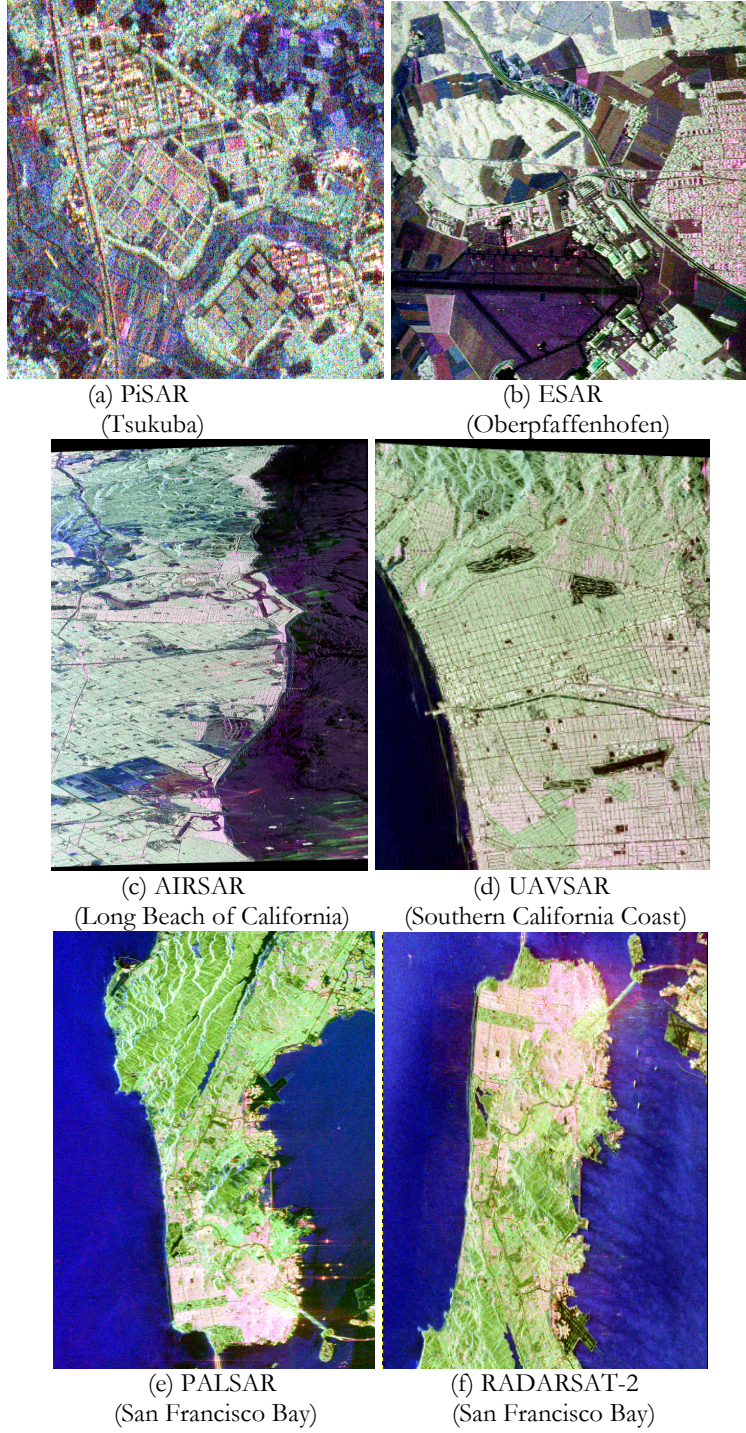
Figure 3.1 PolSAR datasets used in this thesis.

ESAR

ESAR identifies the DLR airborne experimental synthetic aperture radar system which is operated by the Microwaves and Radar Institute. Being developed in the Institute ESAR delivered first images in 1988 in its basic system configuration. Since then the system has been continuously upgraded to become what it is today: a versatile and reliable workhorse in airborne Earth observation with applications worldwide. ESAR can operate in four frequency bands, X-, C-, L- and P-band, hence it covers a range of wavelengths from 3 to 85 cm. The polarisation of the radar signal is selectable, horizontal as well as vertical. The ESAR data used for this thesis is in L-band with a resolution of about 3 meters in both azimuth and range direction.

3.2.2 Ancillary data

In addition to the above PolSAR images, some ancillary data were also used to support the experiments. To verify the results, some optical images from Google Earth covered the same study areas were employed as the reference images. Moreover, some field data were also collected during the SAR observations.

4 Methodology

This chapter describes urban area information extraction methodologies using PolSAR data. The chapter consists of three main parts. The first part focuses on urban scattering analysis, which considers polarimetric decomposition techniques. The second part is target extraction from urban areas, where the research work consists of man-made target detection and edge detection. The edge pixels are helpful for superpixel generation. The third part concentrates on urban area classification and segmentation, which is based on the first part and the second part. Here, the urban scattering mechanisms are analysed and scattering powers of different land covers are obtained after decomposition. After that, classification can be implemented using the scattering components. This pixel-based classification result can be further improved with the superpixels. The flowchart in Figure 4.1 gives an overview of all major analytic steps:
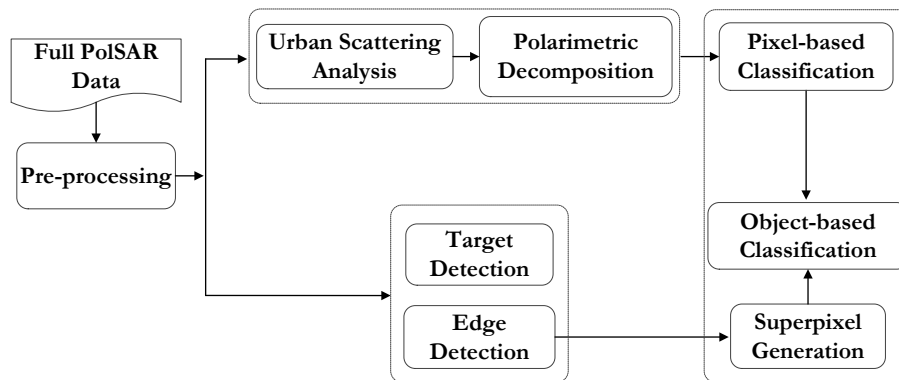
Figure 4.1 Methodology flowchart of the whole thesis

There are mainly two stages in the pre-processing. Firstly, co-registration should be performed on the optical images. The optical reference data should be co-registered to the PolSAR data scenes, which will be useful to validate the detection and classification results. And then speckle filtering is carried out on the full PolSAR data. There are many speckle reduction algorithms proposed for PolSAR data, in this thesis, the classical refined Lee filter (Lee, Grunes, and De Grandi 1999) was chosen since it can preserve statistical characteristics similar to multilook processing, and also can avoid introducing cross-talk. Moreover, this filter is easy to be implemented and can perform efficiently.

35

4.1 PolSAR Model-Based Decomposition

In this section, a new cross scattering matrix for urban areas and two modified four-component model-based decompositions are presented. If we regard the HV scattering as an independent cross scattering and add it to the Yamaguchi four-component model-based decomposition, we can distinguish the cross-polarized scattering of built-up areas from that of forests. This decomposition procedure is designed to validate the proposed scattering model. After that, like most of the other urban area decomposition techniques, the cross-polarized scattering of urban areas is regarded as their volume scattering, which can reduce the volume scattering overestimation. We first introduce the new cross scattering model, followed by two modified decomposition procedures.

4.1.1 New Cross Scattering Model

As shown in Chapter 2, the sample coherency matrix $\mathbf{T}$ can be created from $\mathbf{k}$ as

$$\langle [\mathbf{T}] \rangle = \langle \mathbf{k}\mathbf{k}^{\dagger} \rangle = \begin{bmatrix} T_{11} & T_{12} & T_{13} \\ T_{12}^* & T_{22} & T_{23} \\ T_{13}^* & T_{23}^* & T_{33} \end{bmatrix} \tag{4.1}$$

Then we can get the polarization orientation angle θ as (Lee 2002)

$$\theta = \frac{1}{4} \tan^{-1} \left(\frac{2\,\mathrm{Re}\{T_{23}\}}{T_{22} - T_{33}} \right) \tag{4.2}$$

where $\mathrm{Re}\{T_{23}\}$ represents the real component of T_{23}.

Ortho buildings usually exhibit strong double-bounce scattering, which can be modelled by dihedral corner reflectors with zero polarization orientation angle (Freeman and Durden 1998; Yamaguchi et al. 2005). For oriented buildings, the dominant orientation angle of buildings is incorporated into the cosine function to obtain the cross scattering model. Here, the orientation angle distribution is

$$p(\theta) = \frac{1}{2} \cos(\theta - \theta_{\mathrm{dom}}) \quad \text{for} \quad -\frac{\pi}{2} + \theta_{\mathrm{dom}} < \theta < \frac{\pi}{2} + \theta_{\mathrm{dom}} \tag{4.3}$$

where θ_{dom} is the dominant orientation angle or direction of buildings, which can be get by Eq. (4.3). Then the theoretical ensemble matrix for oriented building reflection can be derived as

$$\langle[\mathbf{T}]\rangle_{cross} = \int_{-\pi/2+\theta_{dom}}^{\pi/2+\theta_{dom}} \left[T_d(\theta)\right] p(\theta) d\theta \qquad (4.4)$$

where $T_d(\theta)$ is the coherency matrix of dihedral corner reflectors and the scattering matrix can be expressed as

$$\langle[\mathbf{T}]\rangle_{cross} = \begin{bmatrix} 0 & 0 & 0 \\ 0 & \dfrac{1}{2}-\dfrac{1}{30}\cos(4\theta_{dom}) & 0 \\ 0 & 0 & \dfrac{1}{2}+\dfrac{1}{30}\cos(4\theta_{dom}) \end{bmatrix}. \qquad (4.5)$$

It is apparent that this cross scattering matrix is influenced by the building orientation angles. If we use this model to modify four-component decomposition, it is interesting to see that the cross scattering power of buildings with large orientation angles is larger than that of buildings with small orientation angles. This adaptivity is beneficial for urban scattering analysis. Further detailed discussion can be found in Paper 2.

4.1.2 Modifying the Four-Component Decomposition Using Procedure One

This procedure is designed to validate the ability of the proposed scattering matrix to model the HV scattering from urban areas. Even though it has been reported by Moriyama et al. (2005) that scattering response from urban areas can be represented by a sum of responses from surface, double-bounce, and cross scattering, without loss of generality and for the sake of comparison with helix and wire scattering, we apply this decomposition on the whole PolSAR data and check the results in natural and built-up areas respectively. Similar to the framework in (Zhang et al. 2008; Hong and Wdowinski 2014), we also regard this cross scattering component as an independent component and add it to the original four-component model-based decomposition. Therefore, there are five scattering components in the decomposition,

which can be described as follows:

$$\langle[\mathbf{T}]\rangle = f_{\mathrm{s}}\langle[\mathbf{T}]\rangle_{\text{surface}} + f_{\mathrm{d}}\langle[\mathbf{T}]\rangle_{\text{double}} + f_{\mathrm{v}}\langle[\mathbf{T}]\rangle_{\text{volume}}$$

$$+ f_{\mathrm{c}}\langle[\mathbf{T}]\rangle_{\text{helix}} + f_{\mathrm{cro}}\langle[\mathbf{T}]\rangle_{\text{cross}}$$

$$= f_{\mathrm{s}}\begin{bmatrix} 1 & \beta^* & 0 \\ \beta & |\beta|^2 & 0 \\ 0 & 0 & 0 \end{bmatrix} + f_{\mathrm{d}}\begin{bmatrix} |\alpha|^2 & \alpha & 0 \\ \alpha^* & 1 & 0 \\ 0 & 0 & 0 \end{bmatrix} + \frac{f_{\mathrm{v}}}{4}\begin{bmatrix} 2 & 0 & 0 \\ 0 & 1 & 0 \\ 0 & 0 & 1 \end{bmatrix} \quad (4.6)$$

$$+ \frac{f_{\mathrm{c}}}{2}\begin{bmatrix} 0 & 0 & 0 \\ 0 & 1 & \pm j \\ 0 & \mp j & 1 \end{bmatrix} + f_{\mathrm{cro}}\langle[\mathbf{T}]\rangle_{\text{cross}}$$

where $f_{\mathrm{s}}, f_{\mathrm{d}}, f_{\mathrm{v}}, f_{\mathrm{c}}$, and f_{cro} are the expansion coefficients to be determined while $\langle[\mathbf{T}]\rangle_{\text{surface}}, \langle[\mathbf{T}]\rangle_{\text{double}}, \langle[\mathbf{T}]\rangle_{\text{volume}}$, and $\langle[\mathbf{T}]\rangle_{\text{helix}}$ are the well-known expansion matrices corresponding to surface, double-bounce, volume, and helix scattering mechanisms, respectively. For simplicity, the volume scattering here is the symmetric form in (Yamaguchi et al. 2005), employing a randomly oriented dipole model. Eq. (4.7) gives five equations with seven unknowns, where m_{22} and m_{33} are the second and third diagonal element in Eq. (4.5).

$$f_{\mathrm{s}} + f_{\mathrm{d}}|\alpha|^2 + f_{\mathrm{v}}/2 = T_{11} \qquad \text{(a)}$$

$$f_{\mathrm{s}}|\beta|^2 + f_{\mathrm{d}} + f_{\mathrm{v}}/4 + f_{\mathrm{c}}/2 + m_{22}f_{\mathrm{cro}} = T_{22} \quad \text{(b)}$$

$$f_{\mathrm{v}}/4 + f_{\mathrm{c}}/2 + m_{33}f_{\mathrm{cro}} = T_{33} \qquad \text{(c)} \qquad (4.7)$$

$$f_{\mathrm{s}}\beta^* + f_{\mathrm{d}}\alpha = T_{12} \qquad \text{(d)}$$

$$f_{\mathrm{c}}/2 = |\mathrm{Im}(T_{23})| \qquad \text{(e)}$$

We can obtain f_{c} directly from Eq. (4.7e). After obtaining f_{c}, there are four equations with six unknowns. To solve these equations, , additional assumptions should be made and two unknowns need to be fixed similar to (Yamaguchi et al. 2005). According to the sign of $\mathrm{Re}(S_{hh}S_{vv}^*)$, either surface scattering or double-bounce scattering is dominant can be determined, i.e. $f_{\mathrm{s}} = 0$ when $\mathrm{Re}(S_{hh}S_{vv}^*) < 0$ whereas $f_{\mathrm{d}} = 0$ when $\mathrm{Re}(S_{hh}S_{vv}^*) > 0$. Therefore, we can have four unknown parameters with

four equations. However, the analytic expressions are still complex. To make the results clear, the equations can be simplified in the following manner. From Eq. (4.7b) and Eq. (4.7c) we have

$$f_d + (m_{22} - m_{33})f_{cro} = T_{22} - T_{33}, \qquad \mathrm{Re}(S_{hh}S_{vv}^*) < 0$$
$$f_s|\beta|^2 + (m_{22} - m_{33})f_{cro} = T_{22} - T_{33}, \quad \mathrm{Re}(S_{hh}S_{vv}^*) > 0. \tag{4.8}$$

In these two equations, we can omit $(m_{22} - m_{33})f_{cro}$ because it is much smaller than f_d and $f_s|\beta|^2$. Then f_d and f_s can be obtained directly with Eq. (4.7d). Now, the seven unknowns can be estimated as

$$\begin{cases} f_s = \dfrac{|T_{12}|^2}{T_{22} - T_{33}}, \ f_v = 2\left(T_{11} - \dfrac{|T_{12}|^2}{T_{22} - T_{33}}\right), \ \beta = \dfrac{T_{22} - T_{33}}{T_{12}} \\[4mm] f_d = 0, \ f_c = 2|\mathrm{Im}(T_{23})|, \ f_{cro} = \left(T_{33} - \dfrac{f_c}{2} - \dfrac{f_v}{4}\right)/m_{33} \end{cases} \tag{4.9}$$

when $\mathrm{Re}(S_{hh}S_{vv}^*) > 0$ and as

$$\begin{cases} f_d = T_{22} - T_{33}, \ f_v = 2\left(T_{11} - \dfrac{|T_{12}|^2}{T_{22} - T_{33}}\right), \ \alpha = \dfrac{T_{12}}{T_{22} - T_{33}} \\[4mm] f_s = 0, \ f_c = 2|\mathrm{Im}(T_{23})|, \ f_{cro} = \left(T_{33} - \dfrac{f_c}{2} - \dfrac{f_v}{4}\right)/m_{33} \end{cases} \tag{4.10}$$

when $\mathrm{Re}(S_{hh}S_{vv}^*) < 0$. If the result $f_{cro} < 0$, we set $f_{cro} = 0$ and follow the same solutions of Yamaguchi four-component decomposition. Then the decomposed powers can be obtained as

$$P_s = f_s(1 + |\beta|^2), \ P_d = f_d(1 + |\alpha|^2), \ P_v = f_v$$
$$P_c = f_c, \ P_{cro} = f_{cro} \tag{4.11}$$

where P_s, P_d, P_v, P_c, and P_{cro} are the surface, double-bounce, volume, helix, and cross scattering powers, respectively.

4.1.3 Modifying the Four-Component Decomposition Using Procedure Two

4.1.3.1 Discrimination of Urban and Natural Areas in PolSAR images

Urban and natural areas need to be discriminated before decomposition in this procedure and then two scattering coherency matrices are used to model the HV components of these two terrains respectively. It should be noted that the urban areas can be extracted using the proposed target detection method in Paper 2. However, it is a bit complicated. There are several ways to distinguish urban buildings from natural areas quickly. For instance, Moriyama et al. (2005) utilized the correlation coefficient between co- and cross-polarized channels to discriminate these two land covers. The evaluated area can be judged as urban area if the correlation coefficient is close to one and as natural area if the correlation coefficient is close to zero. Sato et al. discriminated these two scattering mechanisms using the sign of $\text{Re}\left\{\left\langle S_{hh}S_{vv}^{*}\right\rangle\right\}$, i.e. urban areas if $\text{Re}\left\{\left\langle S_{hh}S_{vv}^{*}\right\rangle\right\}<0$ whereas natural areas if $\text{Re}\left\{\left\langle S_{hh}S_{vv}^{*}\right\rangle\right\}>0$ (Sato and Yamaguchi 2012). In (Singh, Yamaguchi, and Park 2013), this criterion was adopted to discriminate these two terrains. In (Shan et al. 2012; Shan, Zhang, and Wang 2012), the densely vegetated areas and the residual areas were separated via the H/A/$\overline{\alpha}$ classification. The urban areas are considered in zone1, zone2, and zone5. In (Lee, Oh, and Kim 2012), the co-polarized phase-difference (CPD) was found to be useful to indicate the aligned urban areas, while the cross-polarized phase-difference (XPD) was suitable for the oriented urban areas. In this section, we also use this criterion to distinguish urban areas from natural areas. The formulas for CPD and XPD are given as

$$\rho_{hhvv}\exp(j\varphi_{hhvv})=\frac{\left\langle S_{hh}S_{vv}^{*}\right\rangle}{\sqrt{\left\langle S_{hh}S_{hh}^{*}\right\rangle\left\langle S_{vv}S_{vv}^{*}\right\rangle}} \tag{4.12}$$

$$\rho_{hhhv}\exp(j\varphi_{hhhv})=\frac{\left\langle S_{hh}S_{hv}^{*}\right\rangle}{\sqrt{\left\langle S_{hh}S_{hh}^{*}\right\rangle\left\langle S_{hv}S_{hv}^{*}\right\rangle}} \tag{4.13}$$

where φ_{hhvv} and φ_{hhhv} are the CPD and XPD respectively. ρ_{hhvv} and ρ_{hhhv} are correlation coefficients. As we know, the CPD equals 180 degrees for ideal double-bounce scattering and zero degree for ideal surface

scattering (Lee and Pottier 2009). However, when the orientation angles of buildings are large, e.g., 45 degrees, the dominated scattering mechanism of urban areas is not double-bounce scattering any more. The CPD is not high enough, and consequently the CPD cannot be used to describe the urban scattering in such cases (Lee, Oh, and Kim 2012). For most natural surfaces such as bare and vegetation covered fields, the XPD is uniformly distributed over $[0, 2\pi]$, and therefore contains less target specific information. However, for oriented built-up urban areas, since there are many structures such as tilted metallic edges which make large contributions to the cross-polarization due to the orientation angle effects (Lee 2002), the XPD is close to 180 degrees. Hence, the XPD can be used to discriminate the oriented built-up areas. Lee et al. (2012) stated that buildings with orientation angles less than 22.5 degrees can be well discriminated by the CPD, buildings with orientation angles larger than 22.5 degrees can be discriminated by the XPD.

4.1.3.2   Framework of the Proposed Decomposition

Similar to (Sato and Yamaguchi 2012), the proposed cross scattering model is used to model the HV component of urban areas and the decomposed power is regarded as their volume scattering. For natural areas, the volume scattering matrices of Yamaguchi four-component are adopted. Therefore, in this section, we only focus on solving the equations for urban areas. The decomposed powers for natural areas can be obtained using the same way in (Yamaguchi et al. 2005; Yamaguchi, Yajima, and Yamada 2005). Similar to (Sato and Yamaguchi 2012), the decomposition equation can be represented as

$$\left\langle [\mathbf{T}] \right\rangle = f_s \left\langle [\mathbf{T}] \right\rangle_{\text{surface}} + f_d \left\langle [\mathbf{T}] \right\rangle_{\text{double}} + f_c \left\langle [\mathbf{T}] \right\rangle_{\text{helix}}$$
$$+ \begin{cases} f_v \left\langle [\mathbf{T}] \right\rangle_{\text{Y4}} & \text{for natural areas} \\ f_v \left\langle [\mathbf{T}] \right\rangle_{\text{cross}} & \text{for urban areas} \end{cases} \qquad (4.14)$$

where $f_s, f_d, f_v,$ and f_c are the expansion coefficients to be determined. $\left\langle [\mathbf{T}] \right\rangle_{\text{surface}}, \left\langle [\mathbf{T}] \right\rangle_{\text{double}}$, and $\left\langle [\mathbf{T}] \right\rangle_{\text{helix}}$ are the expansion matrices corresponding to surface, double-bounce, and helix scattering mechanisms, respectively. $\left\langle [\mathbf{T}] \right\rangle_{\text{Y4}}$ represents the volume scattering coherency matrix of Yamaguchi four-component decomposition and

$\langle[\mathbf{T}]\rangle_{\text{cross}}$ is the proposed cross scattering model. Then we can get five equations with six unknowns as shown in Eq. (4.15).

$$
\begin{aligned}
f_s + f_d |\alpha|^2 &= T_{11} &&\text{(a)}\\
f_s |\beta|^2 + f_d + f_c / 2 + m_{22} f_v &= T_{22} &&\text{(b)}\\
f_c / 2 + m_{33} f_v &= T_{33} &&\text{(c)}\\
f_s \beta^* + f_d \alpha &= T_{12} &&\text{(d)}\\
f_c / 2 &= |\text{Im}(T_{23})| &&\text{(e)}
\end{aligned}
\tag{4.15}
$$

It can be seen that f_c and f_v can be obtained from Eq. (4.15e) and Eq. (4.15c) directly. The remaining four unknowns with three equations can be solved using the same manner in (Yamaguchi et al. 2005). Therefore, the decomposed volume scattering power for urban areas can be obtained as

$$
P_v = \left(T_{33} - \frac{1}{2} f_c \right) / \left(\frac{1}{2} + \frac{1}{30} \cos(4\theta_{\text{dom}}) \right). \tag{4.16}
$$

Specifically, when $\theta_{\text{dom}} = 0°$, $P_v = \frac{15}{8} \left(T_{33} - \frac{1}{2} f_c \right)$, which is the same as (Sato and Yamaguchi 2012). When $\theta_{\text{dom}} = 22.5°$, $P_v = 2 \left(T_{33} - \frac{1}{2} f_c \right)$, the same as (Hong and Wdowinski 2014). When $\theta_{\text{dom}} = 45°$, $P_v = \frac{15}{7} \left(T_{33} - \frac{1}{2} f_c \right)$. We can see that the volume scattering power of buildings with large orientation angles is larger than that of buildings with small orientation angles. This is reasonable because the former can generate stronger cross-polarized scattering component. Consequently, the proposed scattering model can reduce the underestimation of HV component for urban areas with large orientation angles. If we use the volume scattering model in (An, Cui, and Yang 2010), $P_v = 3 \left(T_{33} - \frac{1}{2} f_c \right)$. However, this scattering matrix is also a cloud of dipole scatterers like that of the Freeman volume scattering model, the volume scattering of urban areas may be still overestimated. Figure 4.2 shows the proposed decomposition scheme using procedure two.
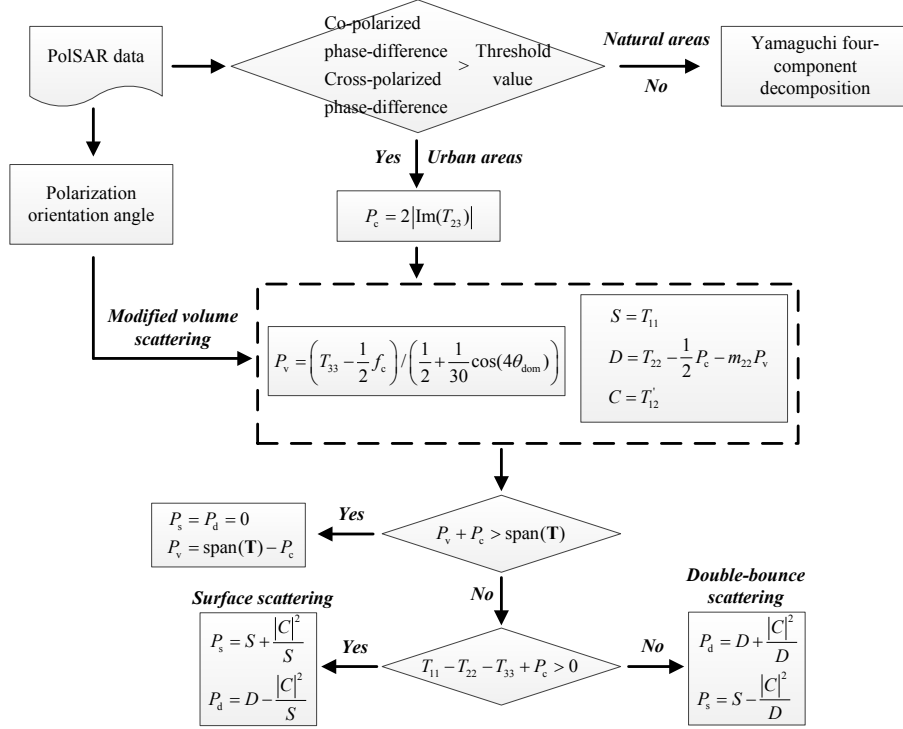
Figure 4.2 The proposed decomposition framework using procedure two.

4.2 Man-Made Target Detection

4.2.1 Reflection Asymmetry Ratio of Man-Made Targets

In Chapter 2 we show that the sample coherency matrix $\mathbf{T}$ obeys a scaled multivariate complex Wishart distribution with density given by

$$P(\mathbf{T}\,|\,\Sigma) = \frac{n^{qn}\,|\,\mathbf{T}\,|^{n-q}\,\exp(-\mathrm{Tr}(n\Sigma^{-1}\mathbf{T}))}{K(n,q)\,|\,\Sigma\,|^{n}}$$

$$K(n,q)=\pi^{q(q-1)/2}\prod_{j=1}^{q}\Gamma(n-j+1)$$

(4.17)

where n represents the number of looks, and q represents the number of elements of the target vector $\mathbf{k}$. $\Gamma(\cdot)$ is the gamma function. Σ denotes the averaged sample coherence matrix with $\Sigma = E(\mathbf{k}\mathbf{k}^{\mathrm{H}})$. Tr and $|\cdot|$ denote the trace and the determinant, respectively. Ainsworth et al. (2008) pointed out the above full coherency matrix determines the

43

conventional RR-LL correlation coefficient $|\rho|$. Forcing reflection symmetry in Eq. (4.17) by setting matrix elements $T_{13} = T_{23} = 0$ defines the normalized RR-LL correlation coefficient $|\rho_0|$. For reflection symmetric scattering the ratio $|\rho|/|\rho_0|$ is one, since both linear co-pol and cross-pol correlations are already zero. In contrast, the ratio has larger values for scattering from reflection asymmetric structures.

Normalized circular-pol correlation coefficient will reduce the man-made target details and may omit the small targets and roads. Here we consider the asymmetry test for man-made targets using the coherency matrix directly. The averaged sample coherency matrix for each pixel is obtained using a sliding local window. Under the hypothesis of reflection symmetry, the maximum likelihood estimate of the coherency matrix is given by

$$\Sigma_{Sym} = \begin{bmatrix} T_{11} & T_{12} & 0 \\ T_{12}^* & T_{22} & 0 \\ 0 & 0 & T_{33} \end{bmatrix}. \tag{4.18}$$

Then the likelihood ratio is

$$\lambda = \frac{P(\mathbf{T}\,|\,\Sigma)}{P(\mathbf{T}\,|\,\Sigma_{Sym})}. \tag{4.19}$$

The denominator of Eq. (4.19) is the probability evaluated under the hypothesis of reflection symmetry, whereas the numerator is the probability evaluated under the hypothesis of reflection asymmetry. Thus we can conclude that the ratio λ is one or nearly one for reflection symmetric structures and has larger values for reflection asymmetric structures. The results are not always satisfactory if we do not consider the time-frequency decomposition. Some complicated man-made targets mixed with vegetation cannot be detected at one azimuth look angle. Since the nonstationarity analysis can provide much more information about complex man-made targets based on the time-frequency decomposition, we combine target reflection asymmetry and nonstationarity analysis to detect man-made targets in the following subsections.

4.2.2 Time-Frequency Decomposition

Full polarimetric SAR images are generally selected for time-frequency analysis. We can use the decomposition technique in both azimuth and range directions. A set of coarser-resolution sub-aperture images containing different parts of the SAR Doppler spectrum can be obtained in the azimuth direction decomposition and another set of sub-aperture images with different observation frequencies is derived from the range direction. As man-made target scattering is more significantly affected by radar looking directions than frequency effects (Ferro-Famil et al. 2003), as well as for the sake of improving the efficiency, time-frequency decomposition in azimuth direction is enough to deal with man-made target extraction problem.

The procedure of full PolSAR data time-frequency decomposition is as follows. Firstly, a 2D Fourier transform is utilized to transform a PolSAR image into the spectral domain. Then the total frequency spectrum is divided into regions, called sub-spectrums, centered around specific spectral locations using a window function such as Hamming window. At last, using a 2D inverse Fourier transform, every sub-spectrum is transformed back into the spatial domain, and thus we can get a sub-aperture image representing the focused PolSAR response around a specific spectral location. The sub-aperture images can be used to characterize some properties of the man-made target scatterers.

4.2.3 Likelihood Ratio Test Based on Nonstationarity and Target Reflection Asymmetry

The likelihood ratio test based on nonstationarity and reflection asymmetry discussed here is similar to the original azimuth nonstationarity detection method (Ferro-Famil et al. 2003), the difference is the null hypothesis. This hypothesis is employed to extract the man-made target characteristics via testing whether the backscatter is nonstationary and asymmetric or not in different sub-aperture images. Therefore, we can have the null hypothesis as $H_0: \Sigma_1 = \cdots = \Sigma_R = \Sigma_{Sym}$, where Σ_i is the original sample coherence matrix of ith sub-aperture image. The likelihood ratio in the ith sub-aperture image is defined as the ratio of the probability calculated from the ith sub-image and the probability calculated from the average of all the sub-images as depicted in Eq. (4.20). Σ_0 is the averaged coherence matrix obtained from all the sub-aperture images under the hypothesis of reflection asymmetry.

$$\lambda_i = \frac{P(\mathbf{T}_i \mid \Sigma_i)}{P(\mathbf{T}_i \mid \Sigma_0)}. \tag{4.20}$$

Similar to Eq. (4.19), the denominator of Eq. (4.20) is also under the hypothesis of reflection symmetry whereas the numerator is under the hypothesis of reflection asymmetry. If the scatter is stationary and the reflection is symmetric, then this ratio is close to one. If the scatter is nonstationary or the reflection is asymmetric, this ratio becomes larger. If the scatter is nonstationary and the reflection is asymmetric, this ratio is even larger. The test will select the alternative hypothesis if the result exceeds a discrimination threshold. In that case we can remove the natural areas and detect man-made targets.

The overall likelihood ratio Λ is calculated as the product of all λ_i, where R is the total number of sub-aperture images. The examination operator shown in Eq. (4.22) is obtained to simplify the calculation.

$$\Lambda = \prod_{i=1}^{R} \lambda_i \tag{4.21}$$

$$\log \Lambda = Rn \log |\Sigma_0| - n \sum_{i=1}^{R} \log |\Sigma_i|. \tag{4.22}$$

This operator is asymptotically distributed as a chi-squared distribution, and the discrimination threshold can be obtained from the quantile $(1-\alpha)$ for an arbitrary false alarm rate α.

4.3   Edge Detection

This section gives a new edge detection method for PolSAR images, which is designed on the basis of the SIRV product model. Using this new edge map, a superpixel generation method is then proposed, which will be discussed in the next section.

4.3.1   SIRV Product Model

In the SIRV product model, the m-dimensional complex measurement $\mathbf{k}$ is defined as (Yao 1973)

$$\mathbf{k} = \sqrt{\tau}\mathbf{z} \tag{4.23}$$

46

where $\mathbf{z}$ is an independent complex circular Gaussian vector with zero mean and normalized covariance matrix $\mathbf{C} = \mathrm{E}\{\mathbf{z}\mathbf{z}^{\dagger}\}$. $\dagger$ denotes the conjugate transpose operator. τ is a positive random variable and its PDF is not explicitly specified. Therefore, the SIRV model can describe a whole class of stochastic distributions. For PolSAR data, the normalized covariance matrix $\mathbf{C}$ characterizes polarimetric diversity while the random variable τ can be considered as the spatial texture, which represents the randomness of spatial variations and only affects the scattering power. The PDF of $\mathbf{k}$ is denoted as (Vasile et al. 2010)

$$p(\mathbf{k} \mid \tau, \mathbf{C}) = \frac{1}{(\pi)^{mN} \mid \mathbf{C} \mid^{N}} \prod_{i=1}^{N} \frac{1}{\tau_i^{m}} \exp\left(-\frac{\mathbf{k}_i^{\dagger} \mathbf{C}^{-1} \mathbf{k}_i}{\tau_i}\right) \qquad (4.24)$$

where N represents the number of independent data used in the estimation. For PolSAR applications, the target vector $\mathbf{k}$ is usually formed using the Pauli basis as

$$\mathbf{k} = \frac{1}{\sqrt{2}}\left[S_{hh} + S_{vv}, S_{hh} - S_{vv}, 2S_{hv}\right]^{\mathrm{T}} \qquad (4.25)$$

here S_{hh}, S_{vv} and S_{hv} are the elements of complex scattering matrix, T is the transpose operator. For a given $\mathbf{C}$, the texture estimator $\hat{\tau}_i$ can be obtained by maximizing the log likelihood function of Eq. (4.24) like

$$\hat{\tau}_i = \frac{\mathbf{k}_i^{\dagger} \mathbf{C}^{-1} \mathbf{k}_i}{m}. \qquad (4.26)$$

Replacing τ_i in Eq. (4.24) with Eq. (4.26), we can obtain the maximum likelihood estimator of $\mathbf{C}$ as

$$\hat{\mathbf{C}} = f\left(\hat{\mathbf{C}}\right) = \frac{m}{N} \sum_{i=1}^{N} \frac{\mathbf{k}_i \mathbf{k}_i^{\dagger}}{\mathbf{k}_i^{\dagger} \hat{\mathbf{C}}^{-1} \mathbf{k}_i} \qquad (4.27)$$

which can be obtained by a recursive algorithm as

$$\hat{\mathbf{C}}_{i+1} = f(\hat{\mathbf{C}}_i). \qquad (4.28)$$

Note that the convergence of Eq. (4.28) can be assured regardless the initialization (Vasile et al. 2010). The algorithm can be initialized with the identity matrix $\hat{\mathbf{C}}_0 = \mathbf{I}_m$. In practice, five or six iterations are usually sufficient for this convergence. The maximum likelihood estimator of span is then defined as

$$\hat{P} = \frac{1}{N} \sum_{i=1}^{N} \mathbf{k}_i^\dagger \hat{\mathbf{C}}_i^{-1} \mathbf{k}_i. \tag{4.29}$$

In terms of the number of samples N used in the estimation, existing studies have shown that the span driven adaptive neighbourhood (SDAN) (Vasile et al. 2008) can achieve a good trade-off between preserving signal characteristics and collecting a large number of samples. **Algorithm 1** gives the estimation process of normalized covariance matrix with SDAN spatial support for one pixel.

Algorithm 1: normalized covariance estimation with SDAN

Begin

    1. Initial estimation

        Estimate $\hat{\mathbf{C}}^{(I)}$, $\hat{P}^{(I)}$ for each pixel within 3*3 neighborhood using (5) and (7)

    2. Region growing

        For pixel(i, j), ***while***$(Count < nThre)$

            if the eight direct neighbors (i', j') satisfy

$$1-\delta \leq \frac{\mathbf{k}^\dagger(i', j')\hat{\mathbf{C}}^{(I)}(i, j)^{-1}\mathbf{k}(i', j')}{\hat{P}^{(I)}(i, j)} \leq 1+\delta \quad \Rightarrow \quad \begin{matrix} (i', j') \in \mathrm{AN}(i, j); Count++ \\ (i, j) = (i', j') \end{matrix}$$

            elseif

$$(i', j') \in \mathrm{AN\_B}(i, j)$$

        Re-estimate $\hat{\mathbf{C}}^{(II)}$, $\hat{P}^{(II)}$ of pixel (i, j) using (5) and (7) within $\mathrm{AN}(i, j)$

    3. Reinspection of the background pixels

        For pixel (i'', j'') in $\mathrm{AN\_B}(i, j)$,

            if satisfy

$$1-T_{\mathrm{low}}\delta \leq \frac{\mathbf{k}^\dagger(i'', j'')\hat{\mathbf{C}}^{(II)}(i, j)^{-1}\mathbf{k}(i'', j'')}{\hat{P}^{(II)}(i, j)} \leq 1+T_{\mathrm{high}}\delta \quad \Rightarrow \quad (i'', j'') \in \mathrm{AN}(i, j)$$

        Re-estimate $\hat{\mathbf{C}}$, $\hat{P}$ of pixel (i, j) using (5) and (7) within $\mathrm{AN}(i, j)$ as the final results, then move to next pixel and repeat Step 1, 2, 3

End

δ denotes the coefficient of variation. AN represents adaptive neighborhood.

AN_B is set of background pixels. *nThre* is the predefined upper limit of neighbor pixels.

$T_{\mathrm{low}}, T_{\mathrm{high}}$ are two thresholds to control the range of AN.

4.3.2 Gauss-Shaped Edge Detector with SIRV Model

Originally proposed by Schou et al. (2003), a set of filters with different orientations are applied on each pixel of a PolSAR image to calculate the edge map. The filter, displayed in Figure 4.4 (a), is controlled by four parameters, i.e., the length l_f, the width w_f, the spacing d_f between two rectangular regions, and the angular increment θ_f between two filter orientations. These filters estimate the average covariance matrix within the rectangular window on both sides of the center pixel and then calculate the Wishart distance as a measure of the probability of an edge pixel. The edge strength of each pixel is represented by the maximum distance from different sets of filters in this pixel. This method has been widely used in various PolSAR image applications (Lang et al. 2014; Qin, Guo, and Lang 2015). There are two limitations:

i)   Rectangle window functions are poor 2-D smoothing filters. Strong speckle in PolSAR data will diminish the average accuracy of the covariance matrix since all the pixels are given equal weights;

ii) Wishart distribution is not suitable for heterogeneous urban areas, resulting in incorrect covariance matrix estimation and the corresponding distance measure.
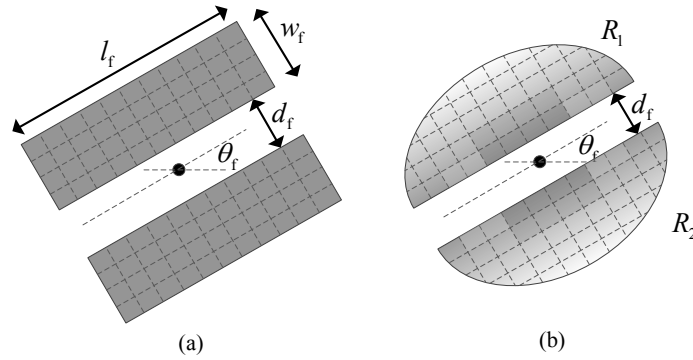
Figure 4.3 Filter configuration. (a) Rectangle-shaped filter. (b). Gauss-shaped filter.

Filter banks have been proven to be effective for edge detection since they can extract directional intensity variations (Shui and Cheng 2012). Inspired by this idea, we replace the rectangle-shaped filter with Gauss-shaped filter to overcome the first limitation of traditional CFAR edge detector, as shown in Figure 4.4 (b). The horizontal Gauss-shaped window function is defined as:

$$W(x, y) = \frac{1}{\sqrt{2\pi}\sigma_x \sqrt{2\pi}\sigma_y} \exp\left(-\left(\frac{x^2}{2\sigma_x^2} + \frac{y^2}{2\sigma_y^2}\right)\right) \quad (4.30)$$

where σ_x and σ_y control the window length and width, respectively. W is the Gauss weight for each pixel, which will be used for the average of covariance matrix on both sides of the central pixel. From Eq. (4.30) it can be observed that the pixels near the centre pixel have larger weights than other pixels. This is in accordance with the fact that information contained at the pixels near the centre pixel is more important than those at other pixels when deciding whether the centre pixel is an edge pixel. Therefore, we can get more accurate average covariance matrix on both sides of the central pixel. At each orientation, the local averaging function for a PolSAR image can be computed as

$$\mathbf{Z} = \frac{\sum_{(x,y)} W(x, y)\hat{\mathbf{C}}(x, y)}{\sum_{(x,y)} W(x, y)}. \quad (4.31)$$

Since the normalized covariance matrix estimated based on SIRV model does not respect the Wishart distribution any more, the Wishart distance cannot be used as the dissimilarity measure. We utilize the SIRV distance (Vasile et al. 2010) to calculate the dissimilarity of covariance matrices on both sides of the central pixel, which can be depicted as

$$D_{\text{SIRV}}(\mathbf{Z}_1, \mathbf{Z}_2) = \ln\frac{|\mathbf{Z}_1|}{|\mathbf{Z}_2|} + \frac{m}{M}\sum_{i=1}^{M}\frac{\mathbf{k}_i^\dagger \mathbf{Z}_1^{-1}\mathbf{k}_i}{\mathbf{k}_i^\dagger \mathbf{Z}_2^{-1}\mathbf{k}_i} \quad (4.32)$$

where $\mathbf{Z}_1, \mathbf{Z}_2$ are the average normalized covariance matrix on both sides of the central pixel, respectively. M is the cardinality of the Gauss-shaped window. Note that computing this distance requires the original scattering vector $\mathbf{k}$. Furthermore, we can also observe that when the texture is high, the second term of Eq. (4.32) becomes small, and the distance is dominated by the determinant ratio. This usually corresponds to strongly polarized targets. However, when the span values are low, the distance is dominated by the second term which takes into account the neighbourhood pixel information. This can reduce the effect of speckle noise to some extent. Therefore, from Eq. (4.31) and Eq. (4.32), we can

see that after incorporating the normalized covariance matrix estimated based on SIRV model and the corresponding dissimilarity measure into the edge detector, the edge detection performance of heterogeneous urban areas should be improved. Hence, the second limitation can be overcome. Inherited from the framework of traditional CFAR edge detector, the proposed method is shown in **Algorithm 2**.

Algorithm 2: proposed edge map calculation for PolSAR data

Begin

    1. Set the parameters σ_x, σ_y, d_f, and θ_f.

    2. Calculate normalized covariance matrix for each pixel using **Algorithm 1**.

    3. For $N_f = \dfrac{\pi}{\theta_f}$ models with different orientations θ_f, calculate the Gauss weight and local averaging covariance matrix using (8) and (9).

    4. Calculate SIRV distance on both sides of the central pixel according to (10).

    5. Find the maximum SIRV distance D_{max} of the N_f values, and the corresponding orientation θ_{max}.

    6. Save the distance D_{max} and the orientation θ_{max}, move to the next pixel, and continue from Step 3.

End

After obtaining the edge map D_{max} for each pixel, we can get the final edge pixels via few post-processing steps as the following. Similar to (Schou et al. 2003), it is tested whether D_{max} is larger than a given threshold, and if this is true, an edge is detected. Since D_{max} approximately satisfies the chi-square distribution (Schou et al. 2003), we can get the threshold through setting a probability of false alarm. Then morphological operations are applied on the thresholding result to fine the final edge pixels.

4.4 Urban Area Classification and Segmentation

4.4.1 Unsupervised Pixel-Based Classification

This subsection will introduce one unsupervised classification method based on the decomposed scattering powers. The objective is to illustrate the ability of scattering components to discriminate different land covers. Therefore, this method only chooses the scattering powers for pixel-based classification without considering the spatial features of PolSAR image. This pixel-based classification result can be further improved with

the superpixels. Since we have discussed the challenges and difficulties of urban area classification in Chapter 2, here we try to resolve the misclassification of ortho and oriented buildings. These two kinds of buildings have quite different polarization orientation angles, leading to different scattering mechanisms. Hence, in order to improve the accuracy of urban area classification, they have to be distinguished.

The whole classification workflow is given in Figure 4.5. First of all, the polarization orientation angle is calculated using the coherency matrix. Then, after polarimetric decomposition using procedure one, five scattering powers are regarded as the inputs of unsupervised K-means classifier. It should be noted that there is only one input parameter in this step, which is the number of classes. In this thesis, the difference of scattering mechanisms of ortho and oriented buildings need to be discussed, therefore, these two kinds of buildings should be regarded as two different classes. Finally, the urban area distribution map can be obtained after the fast unsupervised classification. To further evaluate the urban classification accuracy, the extraction results, including edges and man-made targets, will be utilized as the reference information.
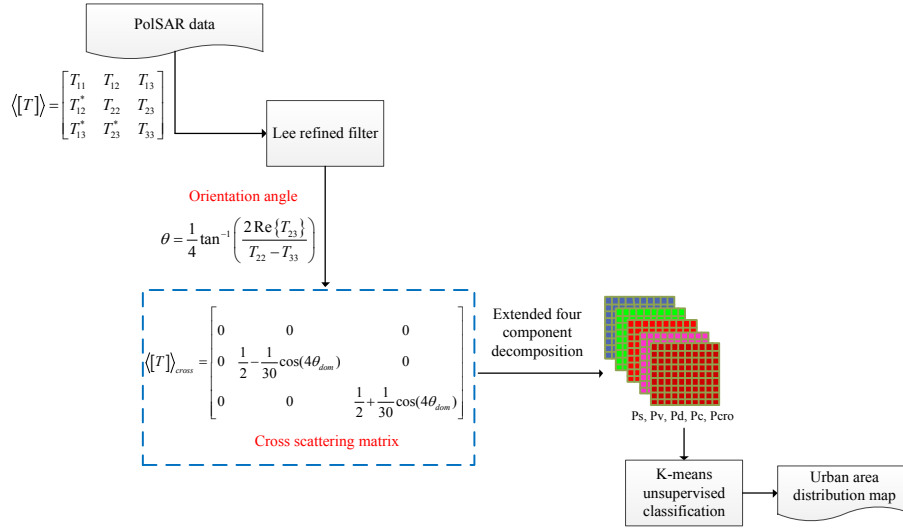
Figure 4.4 Urban area classification framework based on the proposed polarimetric decomposition method.

4.4.2 Adaptive Superpixel Generation

The new edge map introduced in the previous section not only can be beneficial to the initialization of cluster centres in SLIC, but also will be helpful to analyse the homogeneity in PolSAR images. Coefficient of variation (CoV) was firstly proposed in (Lopes, Touzi, and Nezry 1990) for SAR image homogeneity measurement and has been widely used in two decades. This method is dependent on the ENL of the whole image, which can be estimated from a manually selected homogeneous region. However, in fact, the ENL values of different regions may be different, and the estimated ENL of the whole image may not be appropriate for some areas (Anfinsen, Doulgeris, and Eltoft 2009). Inspired by (Lang, Yang, and Li 2015), we utilize the ENL estimation method proposed in (Anfinsen, Doulgeris, and Eltoft 2009) to calculate the ENL value for each pixel and then combine the proposed edge map to define a homogeneity measurement for PolSAR data. It is worth to point out that this ENL estimator is less affected by texture and thus provides more accurate results than other estimators. Therefore, although the technique in (Anfinsen, Doulgeris, and Eltoft 2009) is based on the Wishart distribution, it can be used for ENL estimation in this study.

Since the ENL and edge map are both related to target polarimetric information and more importantly, their value trends in homogeneous and heterogeneous regions are opposite, combining the ENL and edge map can significantly improve the probability of discriminating homogeneous and heterogeneous areas. The homogeneity measurement can be represented as

$$\text{HoM} = \frac{\text{ENL}}{\text{EDGE}} \qquad (4.33)$$

where EDGE denotes the proposed edge map.

The distance measure for PolSAR superpixel generation in this study considers the polarimetric, texture, and spatial information at the same time. The homogeneity measurement is incorporated into the distance measure, making the trade-off factor adaptive to balance the shape and compactness of the superpixels. The SIRV distance between two normalized covariance matrices is given in Eq. (4.32) and can measure the polarimetric information similarity. However, this distance measure is not symmetric, which makes it unsuitable for superpixel generation.

Similar to the definition of symmetric revised Wishart distance in (Anfinsen, Jenssen, and Eltoft 2007), we define the symmetric SIRV distance as

$$SD_{\text{SIRV}}(\mathbf{Z}_1, \mathbf{Z}_2) = \frac{1}{2}\left(D_{\text{SIRV}}(\mathbf{Z}_1, \mathbf{Z}_2) + D_{\text{SIRV}}(\mathbf{Z}_2, \mathbf{Z}_1)\right)$$

$$= \frac{m}{2M}\left(\sum_{i=1}^{M}\frac{\mathbf{k}_i^\dagger\mathbf{Z}_1^{-1}\mathbf{k}_i}{\mathbf{k}_i^\dagger\mathbf{Z}_2^{-1}\mathbf{k}_i} + \sum_{i=1}^{M}\frac{\mathbf{k}_i^?\mathbf{Z}_2^{-}\mathbf{k}_i}{\mathbf{k}_i^?\mathbf{Z}_1^{-}\mathbf{k}_i}\right)$$

(4.34)

where it can be seen that the first term of Eq. (4.32) is removed and the symmetric distance is dominated by the second term which takes into account the neighbour observed samples. This is beneficial for distributed targets, such as complex buildings in heterogeneous urban areas.

In subsection 4.3.1, the conventional covariance matrix can be decomposed into two parts, i.e., the normalized covariance matrix which contains the polarimetric information and the span that contains scalar texture information. Since the distance measure in Eq. (4.34) mainly considers the polarimetric information, we define a texture distance based on the estimated span like

$$D_{\text{T}} = \frac{\left|\hat{P}(x_i, y_i) - \hat{P}(x_j, y_j)\right|}{\max(\hat{P})}$$

(4.35)

where $\max(\hat{P})$ denotes the maximum value of $\hat{P}$ and $|\cdot|$ represents the absolute value operator. It should be noted that since the estimated span only contains the scalar texture information without polarimetric information, simple subtraction operation can be applied directly.

In conventional SLIC, a weighting factor is set manually to balance the spectral similarity and spatial proximity. Similarly, in (Feng, Cao, and Pi 2014; Qin, Guo, and Lang 2015; Song et al. 2015), this parameter is also chosen to be a constant to balance the polarimetric and spatial similarity. This parameter is usually set by trial and error, which might cause over- or under- superpixel segmentation in some spatially complicated areas. In this study, this parameter is set adaptively according to the local spatial complexity of the scene, which can be defined as

$$\beta_{\mathrm{adp}} = \frac{1}{2}\left(\mathrm{HoM}(x_i, y_i) + \mathrm{HoM}(x_j, y_j)\right). \qquad (4.36)$$

It can be seen that this adaptive parameter considers the homogeneity measurement of two compared pixels. Let N_p be the total pixel number, and K is the desired superpixel number. Initially, K cluster centres are sampled on a regular grid of uniform step size $S = \sqrt{N_\mathrm{p}/K}$. Then the complete adaptive distance measure for superpixel generation is defined as

$$D_{\mathrm{Pol\text{-}ASLIC}} = \sqrt{\left(SD_{\mathrm{SIRV}}\right)^2 + \left(D_{\mathrm{T}}\right)^2 + \beta_{\mathrm{adp}} \cdot \left(\frac{d_\mathrm{s}}{S}\right)^2}. \qquad (4.37)$$

where d_s is the spatial distance between two superpixels with centre locations at (x_i, y_i) and (x_j, y_j), respectively and defined as

$$d_\mathrm{s} = \sqrt{(x_i - x_j)^2 + (y_i - y_j)^2}. \qquad (4.38)$$

Since this presented research is designed on the basis of traditional SLIC superpixel generation algorithm, the implementation procedure of this superpixel generation method is similar to that of SLIC except the steps before local iterative clustering.

Input: original PolSAR image
1) Normalized covariance matrix and span estimation using **Algorithm 1**.
2) Edge map calculation based on normalized covariance matrix using **Algorithm 2**.
3) ENL estimation using the method in (Anfinsen, Doulgeris, and Eltoft 2009).
4) Homogeneity measurement calculation using Eq. (4.33).
5) Set the number of superpixels K and initialize the cluster centres.
6) Local iterative clustering with the adaptive distance calculated using Eq. (4.37), detailed explanation can be found in Paper 6.
7) Post-processing to eliminate the disjointed pixels.
Output: superpixel map.

5 Results and Discussion

5.1 Polarimetric Decomposition

This section depicts the urban scattering analysis based on the model-based polarimetric decomposition. Paper 1 gives the cross scattering model for urban areas, and Paper 2 shows the two decomposition procedures with this cross scattering model. The results of these papers are the basis of urban area classification, which will be displayed in the Section 5.4.

5.1.1 Validation of Two Decomposition Procedures

5.1.1.1 Results of Decomposition Procedure One

In this thesis, three datasets are utilized to test the effectiveness of the proposed decomposition method. To compare the results, Yamaguchi four-component model-based decomposition method with rotation of coherency matrix (Y4R) (Yamaguchi et al. 2011), and the multiple-component model-based decomposition method (MCSM) (Zhang et al. 2008) are also implemented. Figure 5.1 gives the decomposition results of spaceborne RADARSAT-2 data. Figure 5.2 shows the percentages of different scattering powers in two selected sites, i.e. one oriented urban area (area A in Figure 5.1) and one vegetation area (area B in Figure 5.1). From Figure 5.1 (b), we can see that for ortho buildings, the double-bounce scattering power is very strong whereas for oriented buildings, it becomes quite low. In contrast, the oriented buildings have strong cross scattering power whereas ortho buildings do not, as shown in Figure 5.1 (e). It is also interesting to see that vegetated areas have quite low cross scattering power compared to oriented buildings although they both contribute to the overall HV scattering. These facts indicate that the proposed cross scattering model can effectively describe the HV scattering component from oriented buildings. Figure 5.1 (d) gives the helix scattering power, where we can see that the oriented buildings also have the strongest powers among different land covers. What we can see from Figure 5.1 (f)-(h) is that this cross scattering makes the difference between oriented buildings and vegetation more clear. In contrast, in Y4R decomposition, these two land covers both show strong volume scattering. Although wire scattering can also enhance the urban characteristic in MCSM decomposition, the volume scattering of vegetation and the surface scattering of sea are suppressed, as shown in Figure 5.1 (h).
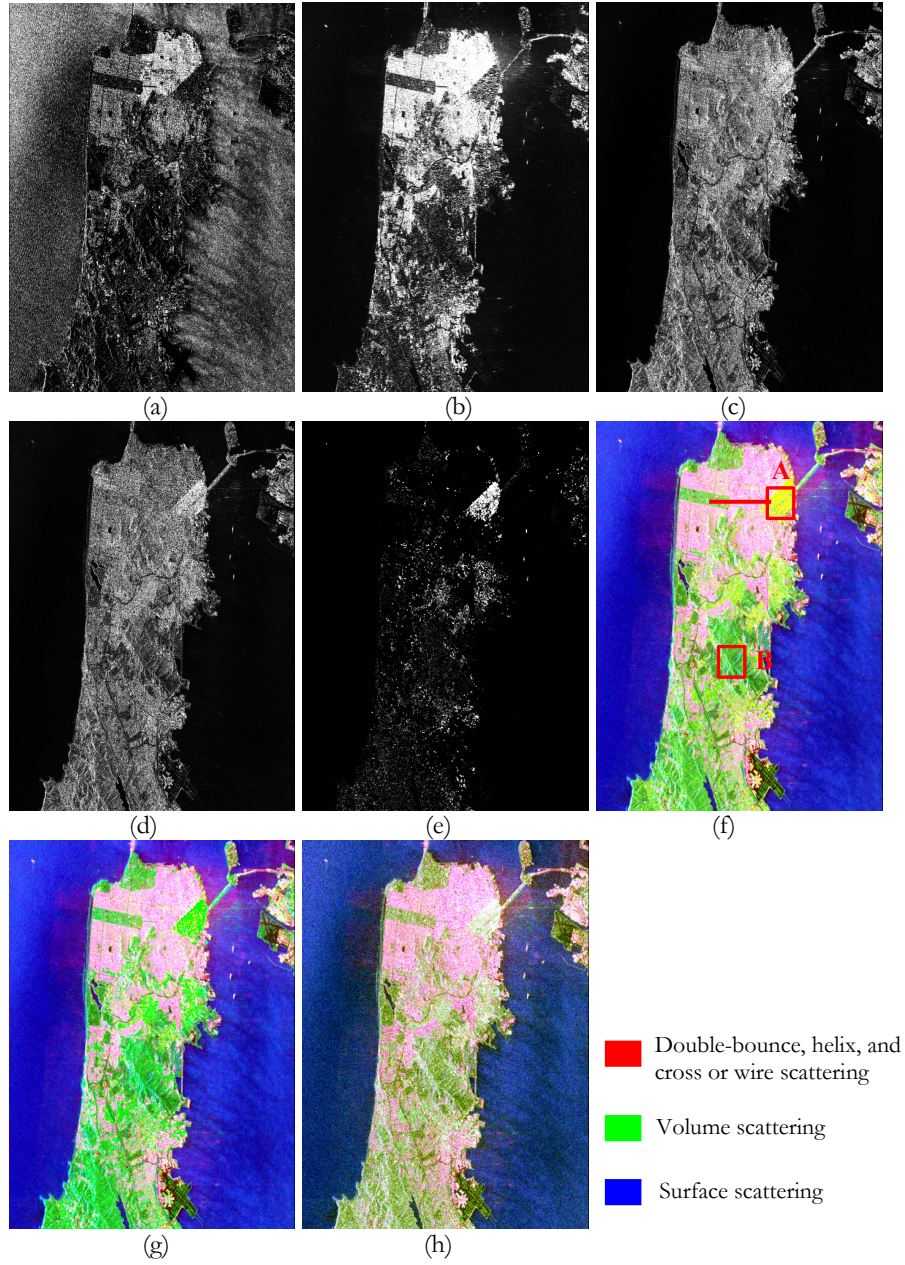
Figure 5.1 Scattering powers and decomposition results of RADARSAT-2 data. (a)-(e) Surface, double-bounce, volume, helix, and cross scattering powers of the proposed method. (f)-(h) Decomposition results (blue—surface scattering, red—urban scattering (from double-bounce, helix and cross or wire scattering), and green—volume scattering.) of the proposed, Y4R, and MCSM methods, respectively.
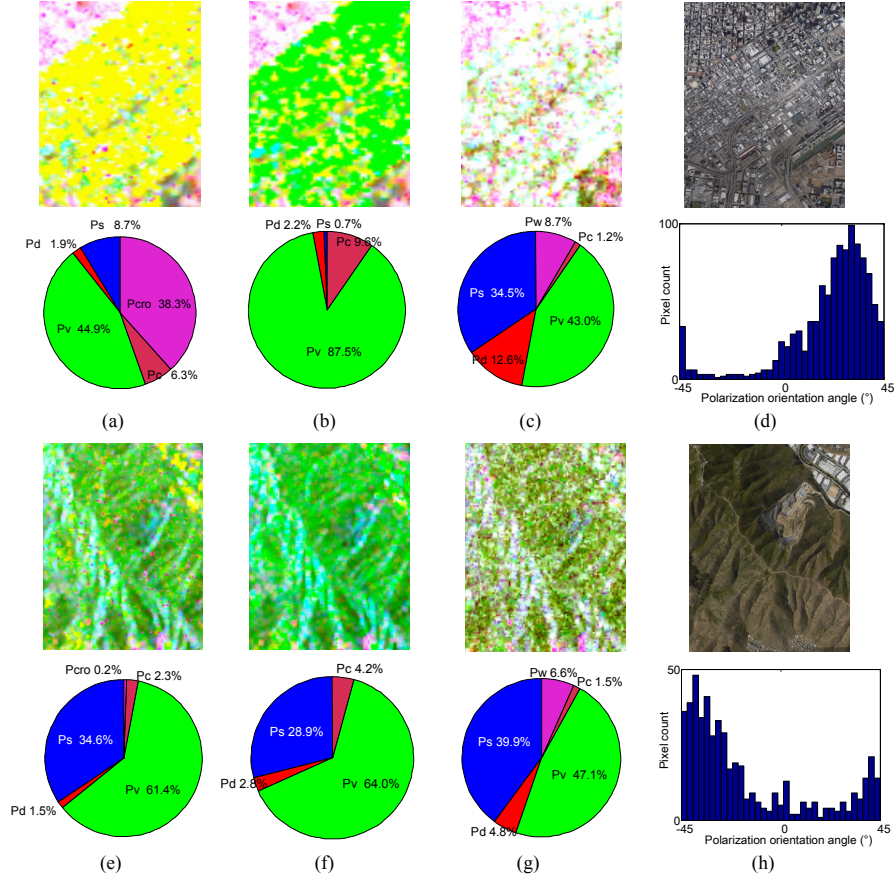
Figure 5.2 Detailed decomposition results of two selected sites. (a)-(c) Decomposition results and the scattering power distribution of the proposed, Y4R, and MCSM methods in area A. (e)-(g) Decomposition results and the scattering power distribution of the proposed, Y4R, and MCSM methods in area B. (d) and (h) Optical image and the estimated polarization orientation angle histogram of area A and B, respectively.

From Figure 5.2, we can see that in urban areas, the scattering powers of double-bounce and helix of the proposed method are similar to those of Y4R. However, the cross scattering power is very strong and the volume scattering power is reduced significantly. Furthermore, the surface scattering power also increases slightly. This fact indicates that our proposed method can successfully separate the cross scattering caused by oriented buildings from the overall HV scattering component. Even though MCSM can also reduce the volume scattering in urban areas, the surface scattering is too strong and the wire scattering is not evident.

Therefore, the urban characteristic is weaker than that of the proposed method. The scattering of oriented buildings is still mixed with that of vegetation after decomposition. From Figure 5.2 (e) to Figure 5.2 (g), it can be observed that the scattering powers of our proposed method are similar to those of Y4R method in vegetated areas. The cross scattering power contribution is only 0.2%. Nevertheless, the result of MCSM decomposition is quite different, where the volume scattering power is lower than those of other methods and the wire scattering still exists. Therefore, there exists slight volume scattering underestimation in vegetated areas. Figure 5.2 (d) and Figure 5.2 (h) display the corresponding optical images and the estimated polarization angle distributions of two sites, respectively. It is clear to see that the orientation angles of these two areas are both mainly around 45 degrees; however, the cross scattering powers are quite different. According to the above analysis, it can be summarized that the proposed cross scattering model is effective to describe the HV scattering component from oriented buildings. In contrast, the dipole volume scattering matrix of Yamaguchi four-component decomposition is more suitable to model the HV component from vegetation.

Figure 5.3 gives the decomposition results of three different methods using AIRSAR data. What we can see from Figure 5.3 (a) is that the cross scattering of oriented buildings is generated clearly whereas water and ortho buildings have quite low cross scattering powers, as shown in the area marked with red ellipse. From Figure 5.3 (b) and Figure 5.3 (c), it can be observed that there is an apparent difference in oriented built-up areas, which results from the cross scattering contribution. Moreover, the scattering mechanisms of water and vegetation in Figure 5.3 (b) are similar to those in Figure 5.3 (c), indicating that the proposed cross scattering model mainly describes the HV component caused by oriented buildings. Therefore, the volume scattering underestimation in forest areas is low. MCSM decomposition result is shown in Figure 5.3 (d), compared to Figure 5.3 (c), the volume scattering power of oriented buildings is reduced and the wire scattering also enhances the urban characteristics. Nevertheless, the decomposed scatterings of vegetation and water are worse than those of Y4R and the proposed approach. The volume scattering of vegetation is not strong, in addition, some water areas show volume scattering not the surface scattering. Therefore, wire scattering has negative influence on the decomposition of vegetation and water areas. It is worth mentioning that MCSM decomposition seems to perform better than the proposed method in oriented urban areas. This

is because in this AIRSAR data, the buildings have small orientation angles (about 15 degrees). The HV scattering component is not significant, leading to low cross scattering power. Further analyses and discussions are shown in Paper 1 and Paper 2.
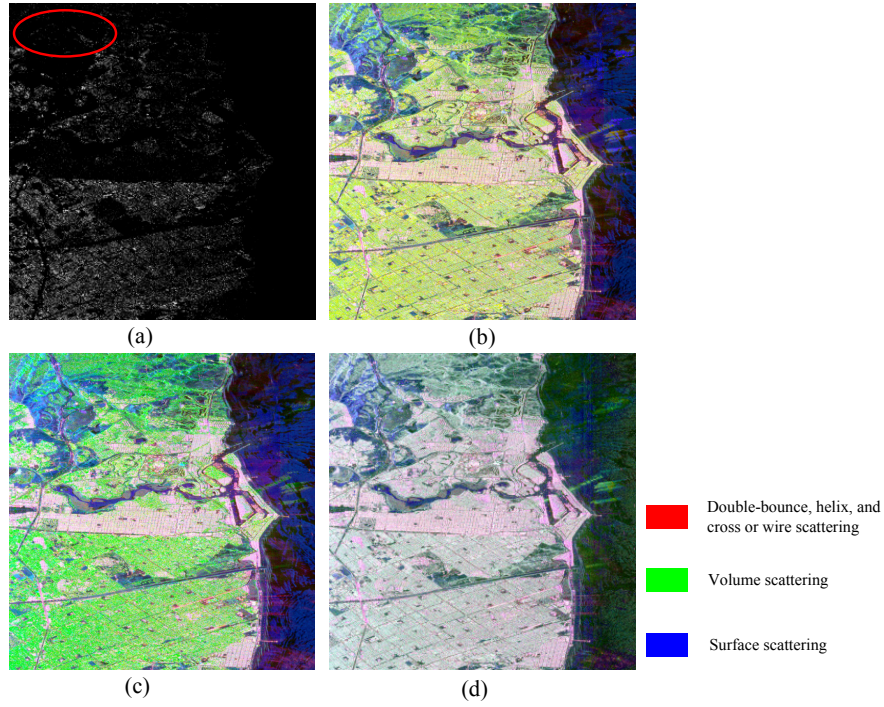
Figure 5.3 Cross scattering power and the decomposition results of AIRSAR data. (a) Cross scattering powers of the proposed method. (b)-(d) Decomposition results (blue—surface scattering, red—urban scattering (from double-bounce, helix and cross or wire scattering), and green—volume scattering.) of the proposed, Y4R, and MCSM methods, respectively.

The decomposition results of UAVSAR are similar to those of AIRSAR, which are shown in Figure 5.4. We can observe from Figure 5.4 (a) that cross scattering powers of the forests and oriented buildings are different. There are quite few cross scatterings in forests (e.g., red rectangular area) and ortho buildings whereas the cross scattering in oriented buildings is apparent. Two patches of ortho and oriented buildings (area A and area B in Figure 5.4 (a)) are selected and the histograms of their cross scattering powers are displayed in the right column of Figure 5.4. It can be observed that buildings with large orientation angles exhibit larger cross scattering powers than those with small orientation angles. From

Figure 5.4 (b) - Figure 5.4 (d), we can see that for forest areas, the result of our proposed method is very similar to the result of Y4R whereas in MCSM decomposition, it seems that the volume scattering is underestimated. For ortho urban buildings, the results of three methods are all satisfactory; however, for oriented buildings, the colour in Figure 5.4 (b) is a little bit yellow, resulting from the cross scattering.
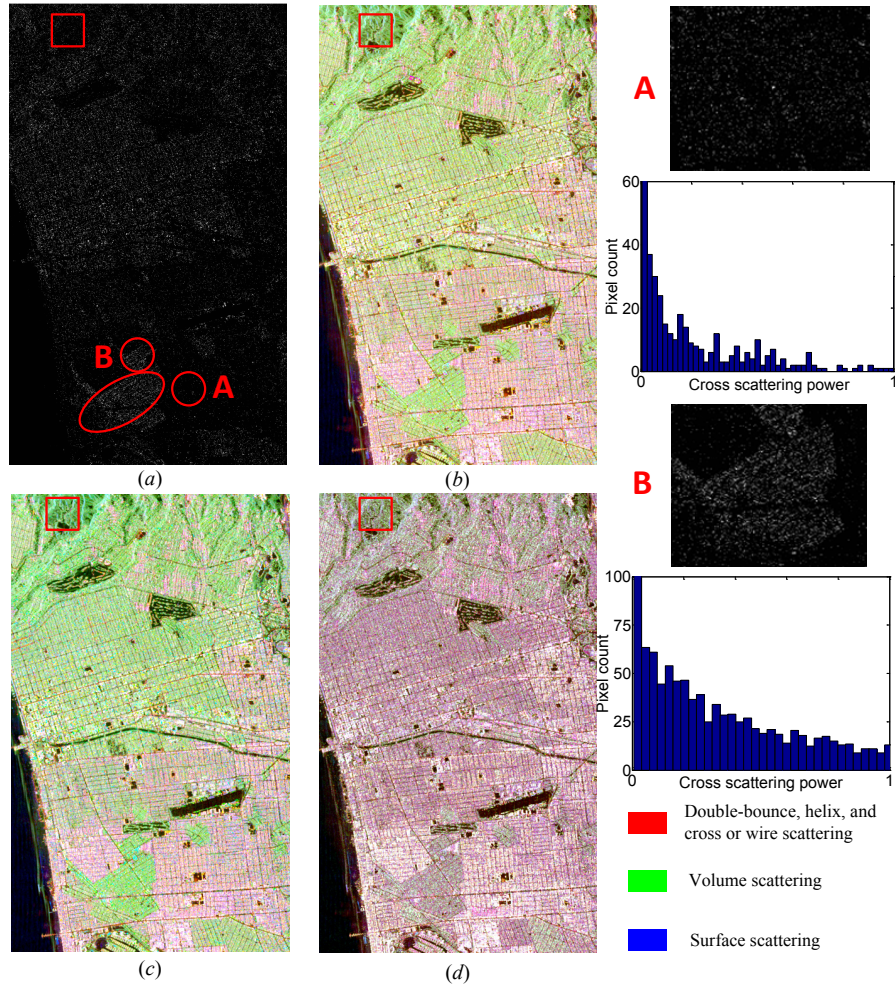
Figure 5.4 Cross scattering power and the decomposition results of UAVSAR data. (a) Cross scattering powers of the proposed method. (b)-(d) Decomposition results (blue—surface scattering, red—urban scattering (from double-bounce, helix and cross or wire scattering), and green—volume scattering.) of the proposed, Y4R, and MCSM methods, respectively. Right column is the cross scattering power and corresponding histograms of area A and B in (a).

61

5.1.1.2   Results of Decomposition Procedure Two

Like most of the other urban area decomposition techniques, in this subsection we only apply this cross scattering model on urban areas to model the HV components caused by oriented buildings and regard them as their volume scattering. For natural areas, the volume scattering coherency matrices of Yamaguchi four-component are still adopted. The above RADARSAT-2 data are used and two existing methods, which are proposed in (Sato and Yamaguchi 2012) and (Shan, Zhang, and Wang 2012), are implemented for comparison in this experiment.
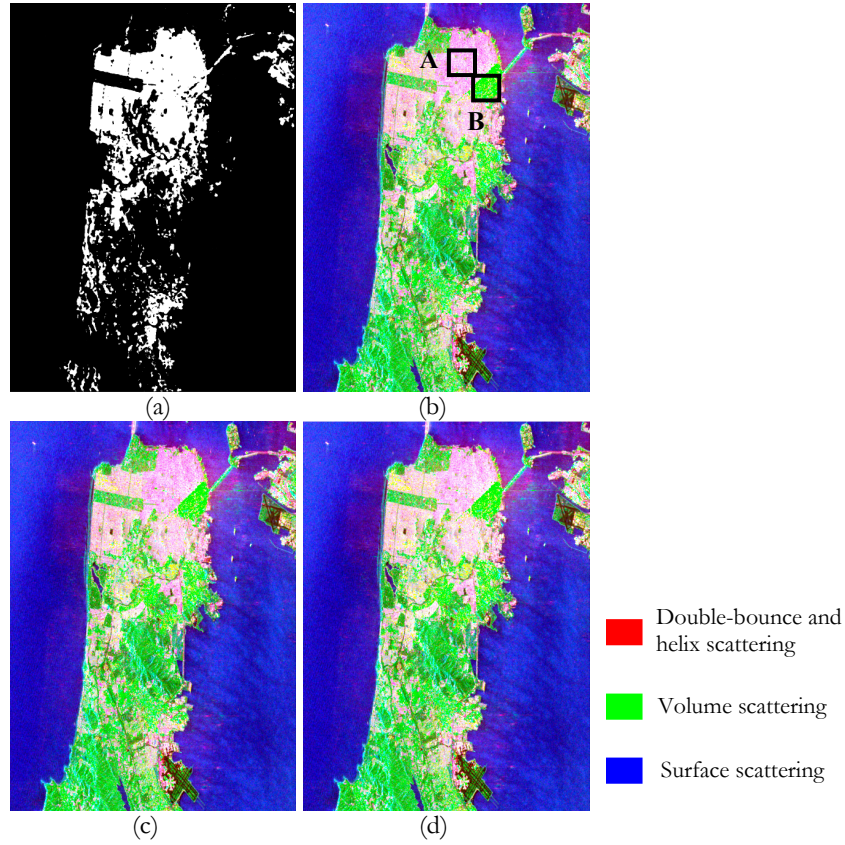
Figure 5.5 (a) Binary image of the region where threshold value was exceeded. (b)-(d) Decomposition results of the proposed method, method in (Sato and Yamaguchi 2012), and method in (Shan, Zhang, and Wang 2012), respectively.

Firstly, to discriminate between the urban areas and the natural distributed areas, the threshold value of CPD and XPD is chosen to be 120 degrees. The region where the threshold value is exceeded is shown in Figure 5.5 (a). Figure 5.5 (b)–(c) depict the decomposition results of

our proposed technique using procedure two, method in (Sato and Yamaguchi 2012), and method in (Shan, Zhang, and Wang 2012) respectively. Since natural areas have the same decomposition, in the following analysis, we only focus on urban areas. It can be seen that the results of these three methods are very similar, this is because the volume scattering power difference is not significant. To make the difference clear, we select two urban areas, which are marked with A and B in Figure 5.5 (b), and then list the quantitative comparison in Table 5.1 and Table 5.2, respectively.

Table 5.1 Distribution of scattering components with different methods (area A)

Scattering components	Proportion of scattering components (%)		
	Proposed method	Sato's method	Shan's method
Surface	35.6	35.2	37.4
Double-bounce	56.1	56.3	52.0
Volume	6.0	6.0	8.4
Helix	2.3	2.5	2.3

Table 5.2 Distribution of scattering components with different methods (area B)

Scattering components	Proportion of scattering components (%)		
	Proposed method	Sato's method	Shan's method
Surface	2.8	8.3	0.9
Double-bounce	5.3	8.8	2.6
Volume	84.2	75.0	89.1
Helix	7.7	7.9	7.5

What we can find from Table 5.1 is that for ortho buildings, the scattering component distributions of Figure 5.5 (b) and Figure 5.5 (c) are almost the same; however, the double-bounce scattering power of Figure 5.5 (d) is lower and the volume scattering power is higher. This is because the volume scattering model in Figure 5.5 (d) is also a cloud of dipole scatterers as that of the Freeman volume scattering model. Therefore, the volume scattering of urban areas may be still overestimated. From Table 5.2, it can be observed that for our proposed method, the volume scattering power of the oriented urban areas is 9% higher than that in (Sato and Yamaguchi 2012). As we discussed in the former sections, the proposed cross scattering model can compensate

the loss of HV component from urban areas with large orientation angles. Further discussions and comparisons can be found in Paper 2.

5.1.1.3 Discussion of These Two Decomposition Procedures

The two decomposition procedures in this thesis can both be used for urban scattering analysis. Decomposition procedure one can validate the ability of cross scattering coherency matrix on modelling the HV component from oriented buildings. Therefore, in this decomposition, the scattering mechanisms of ortho and oriented buildings can be clearly discriminated, which will be beneficial for urban area classification without discriminating the natural and urban areas. However, the scattering powers of natural areas may be not very accurate. This coherency matrix is only suitable for urban areas whereas dipole volume scattering coherency matrix is more appropriate for natural areas. Similar to many other existing decomposition methods, decomposition procedure two is implemented for urban and natural areas respectively. Hence, it is beneficial for precise scattering analysis of different land covers because the decomposed scattering powers are more accurate than decomposition procedure one. A detailed discussion can be found in Paper 2.

5.1.2 Comparison and Analysis of the Urban Scattering Components Using RADARSAT-2 Data

The theoretical difference between helix, wire and cross scattering is discussed in section 4.1.1. Here we quantitatively compare these scattering components over vegetation and urban areas. A transect over forest and urban area is displayed using a red line in Figure 5.1 (f) and the corresponding decomposed scattering power profiles are shown in Figure 5.6 (a). The corresponding optical image and the area map are depicted in Figure 5.6 (b) and Figure 5.6 (c), respectively.

It can be seen from Figure 5.6 that the cross scattering power is quite low in both vegetation and ortho urban areas whereas it is quite large in oriented building areas. In contrast, the helix and wire scattering power differences between oriented buildings and vegetation are much smaller than that of cross scattering. Moreover, it also can be seen that the wire scattering is similar to helix scattering, especially for oriented buildings. This is because similar to helix scattering, wire scattering also focuses on the scattering reflection asymmetry of buildings. In contrast, cross

scattering mainly tries to discriminate the HV scattering component caused by oriented buildings from that caused by vegetated areas.
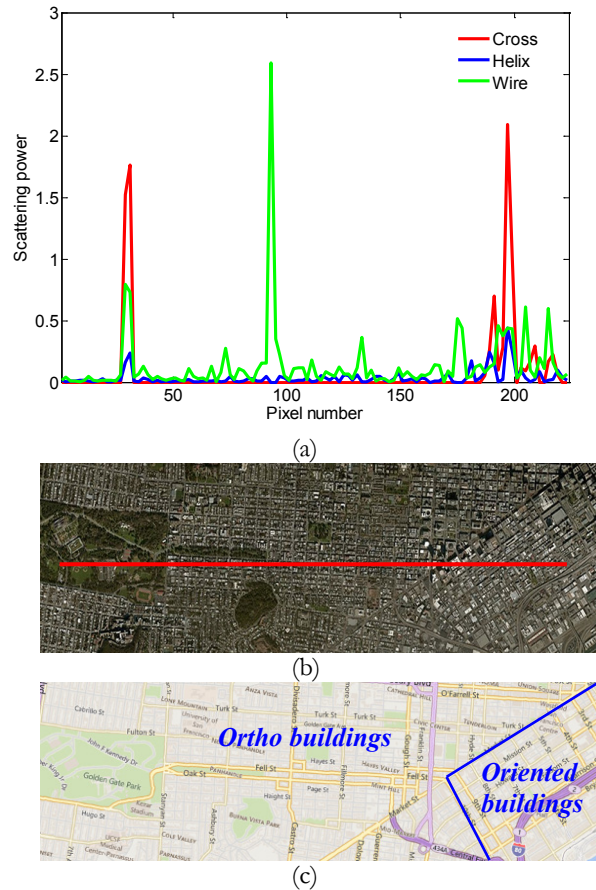
Figure 5.6 (a) Scattering power profiles of three components. (b) Photograph by Google Earth. (c) Map of the test area.

5.2 Man-Made Target Detection

This section gives the man-made target detection results of Paper 3 using two PolSAR datasets, i.e., ESAR and PALSAR, which cover the study areas in Oberpfaffenhofen, Germany and San Francisco Bay, USA.

5.2.1 Experimental Results with ESAR Data

Figure 5.7 (a) is an optical image, which is obtained from Google Earth. Figure 5.7 (b) is the Pauli coded PolSAR image with size 1104 by 724, where the red channel describes double-bounce scattering, blue channel describes surface scattering, and the green channel describes volume

scattering. These two images are co-registered for the convenience of display and comparison. The image columns correspond to range direction, and the rows correspond to azimuth direction. Figure 5.7 (c) gives the Yamaguchi four-component decomposition with rotation of coherency matrix. From the three images, it can be seen that buildings not aligned along the azimuth direction (e.g. buildings in the middle and lower part of the image) show volume scattering, which is the same as forests. This is because these oriented buildings have strong cross-polarized scattering powers. Moreover, the roads also show volume scattering, the man-made grounds and some small targets show surface scattering, indicating that these kinds of man-made targets are difficult to be discriminated from natural areas.
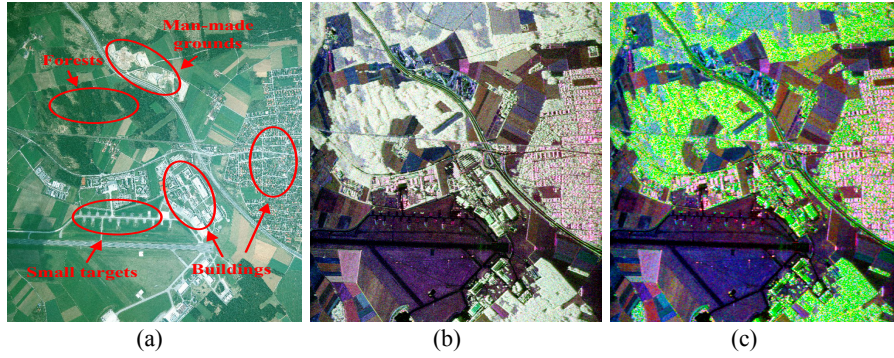
Figure 5.7 Study area and ESAR data. (a) Optical image from Google Earth. (b) Pauli coded ESAR image with L band (Red: HH-VV, green: HV, blue: HH+VV). (c) Yamaguchi four-component decomposition with rotation of coherency matrix (Red: Double-bounce and helix scattering, green: volume scattering, blue: surface scattering).

Three methods are chosen for analysis, i.e., azimuth nonstationarity detection with and without target reflection asymmetry, and the improved azimuth nonstationarity detection method with nonzero-mean statistical model (Wu, Guo, and Li 2014). In this experiment, we set the number of sub-apertures to four for three methods. Figure 5.8 gives the detection results. It is interesting to see that even though the area with label 1 shows surface scattering in the Pauli image, it can be extracted by these three methods. The main reason is that this area is not flat and sub-aperture images can describe the anisotropy at different observation angles. Nevertheless, compared with Figure 5.8 (a), the results in Figure 5.8 (b) and Figure 5.8 (c) are better due to the nonzero-mean statistical model and reflectance asymmetry, respectively. The roads in Figure 5.8 (c) are clearly detected but are missing in Figure 5.8 (a). It is because long

metallic fences have low anisotropy at limited observation angles. However, after introducing the asymmetry, the detection results are significantly improved. Even though nonzero-mean statistical model can improve the detection accuracy, the detected roads are still not obvious. The area with label 3 contains some small parking aprons. They are covered by trees and have approximately round shapes. Although they have isotropic property, they can be extracted using the proposed approach. Further detailed results and comparisons can be found in Paper 3.
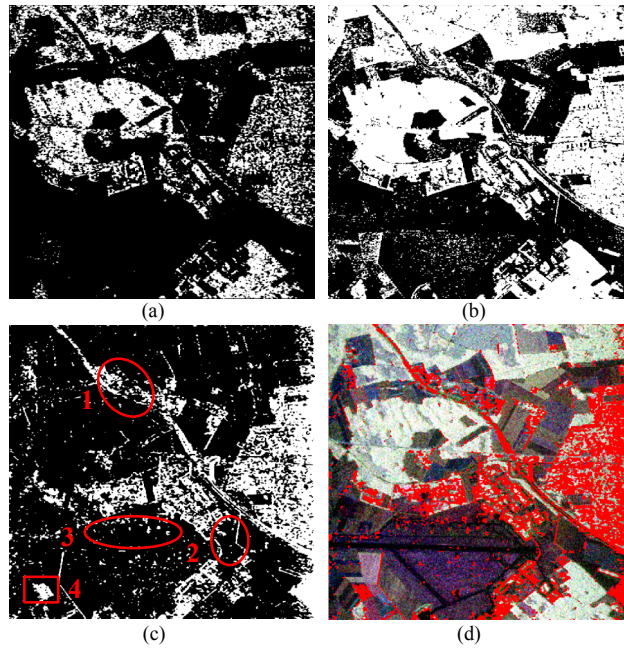
Figure 5.8 Man-made target detection results of (a) original nonstationarity detection method, (b) nonstationarity detection method with nonzero-mean statistical model, and (c) the proposed method. (d). Detection results (red) of the proposed method overlaid Pauli image.

From Table 5.5 we can see that the overall accuracy is about 84%, which is fairly good, and the kappa coefficient is 0.6892, indicating substantial agreement with the visual evaluation of the detection result. Although the original nonstationarity detection method and the method in (Wu, Guo, and Li 2014) can extract most of the buildings, the confusion with vegetation is quite large, and the overall accuracy is 20% lower than the proposed approach, as shown in Table 5.3 and Table 5.4. These methods cannot effectively identify the forest vegetation with Bragg resonance,

which is regarded as man-made targets. Moreover, some of the roads and small man-made targets are also not clearly detected.

Table 5.3 Accuracy Assessment of the Result by Original Nonstationarity Detection Method

	Man-made	Natural	Prod. Acc.
Man-made	73.23%	45.84%	73.23%
Natural	26.77%	54.16%	54.16%
User. Acc.	61.50%	66.92%	
Overall accuracy = 63.69%		Kappa coefficient = 0.2739	

Table 5.4 Accuracy Assessment of the Result by Nonstationarity Detection Method with Nonzero-Mean Statistical Model

	Man-made	Natural	Prod. Acc.
Man-made	79.51%	48.68%	79.51%
Natural	20.49%	51.32%	51.32%
User. Acc.	62.02%	71.47%	
Overall accuracy = 65.42%		Kappa coefficient = 0.3083	

Table 5.5 Accuracy Assessment of the Result by Proposed Method

	Man-made	Natural	Prod. Acc.
Man-made	83.24%	14.32%	83.24%
Natural	16.76%	85.68%	85.68%
User. Acc.	85.32%	83.64%	
Overall accuracy = 84.46%		Kappa coefficient = 0.6892	

5.2.2 In-Depth Analysis of the Detection Results

To further evaluate the performance of asymmetry on man-made target detection, the PolSAR image is decomposed into 2, 3, 4, 5, 6, 7 and 8 sub-aperture images. We select six test areas, i.e., ortho buildings, oriented buildings, forest, roads, bare soil, and small man-made targets, to compare their average log ratio values with different sub-apertures. Figure 5.9 depicts log ratio values of three methods with different sub-apertures, respectively. From Figure 5.9 (a), it can be seen that with original nonstationarity detection method, the forest areas are mixed with two types of buildings all the time, in addition, roads, small man-made targets, and bare soils are also difficult to be distinguished. This

indicates that some natural areas with Bragg resonance also have anisotropy and can easily be detected as man-made targets. Roads and small man-made targets are usually omitted because they have low anisotropy with limited sub-apertures; however, if we increase the number of sub-apertures, the resolution of sub-images gets coarser, making it even more difficult to extract small targets. Figure 5.9 (b) has a similar result with Figure 5.9 (a) except for the roads and small man-made targets. Even though the nonzero-mean statistical model can enhance the anisotropy of man-made targets in high resolution SAR data, the roads and small targets are still not as obvious as the proposed method. This is because their log ratio values are closer to bare soil in Figure 5.9 (b) than in Figure 5.9 (c), which is marked with a red ellipse. Figure 5.9 (c) shows the log ratio values of the proposed approach, where the curve gap between man-made targets and natural areas is bigger, indicating that the result is much better than the other two methods.
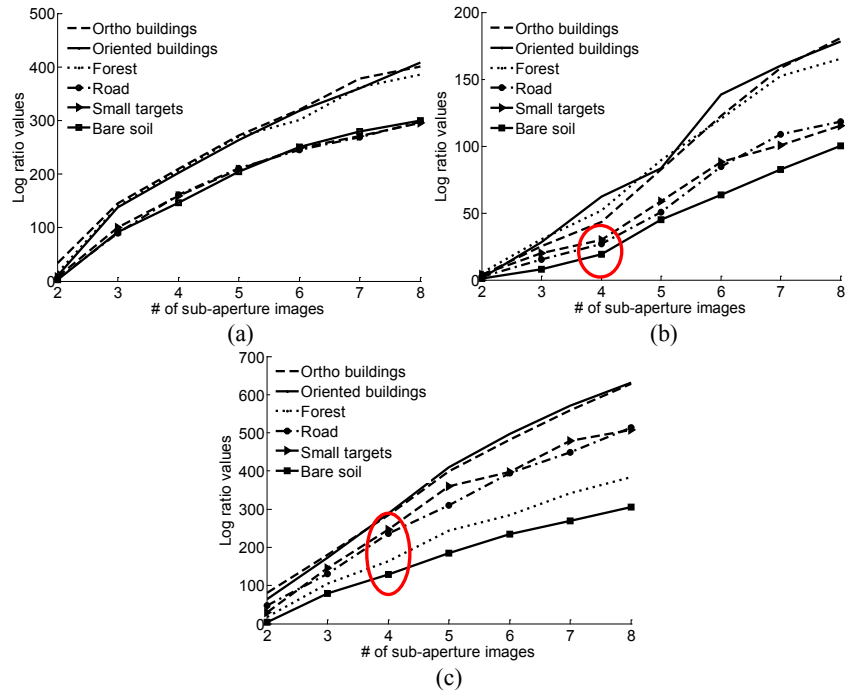
Figure 5.9 Log ratio values of three methods with different sub-apertures. (a) Original nonstationarity detection method. (b) Nonstationarity detection method with nonzero-mean statistical model. (c) The proposed method.

Another issue to be discussed is the number of sub-apertures. It can be observed from Figure 5.9 (c) that when the number gets larger, the difference between man-made targets and natural areas becomes bigger. This is because some man-made targets may have symmetry reflectance at one azimuthal look angle but have strong asymmetry reflectance at another look angle. Therefore, sub-aperture decomposition can help improve the man-made target detection performance of asymmetry. In (Wu, Guo, and Li 2014), the sub-aperture size was set to four. The reason is that too many sub-apertures will lead to a serious reduction of the spatial resolution, which is not good for target detection. In addition, the computation load is also apparent with too many sub-apertures. However, this conclusion was not demonstrated with quantitatively analysis. From Figure 5.9, it can be seen that the difference of log ratio values between man-made targets and natural areas does not change dramatically when the number of sub-apertures exceeds four. Considering time consuming and to compare the detection result with (Wu, Guo, and Li 2014), four sub-apertures are suitable for man-made target detection in our experiment.

5.2.3 Experimental Results with PALSAR Data

The second study area is located in San Francisco Bay, USA. This spaceborne PALSAR Polarimetric SAR data, with centre frequency 1270 MHz, i.e., L-band., was acquired over the study area in 2009. The image columns correspond to range direction and the rows correspond to azimuth direction. Figure 5.10 (a) gives the optical image of the study area and Figure 5.10 (b) is the Pauli coded PolSAR image.

(a)   (b)
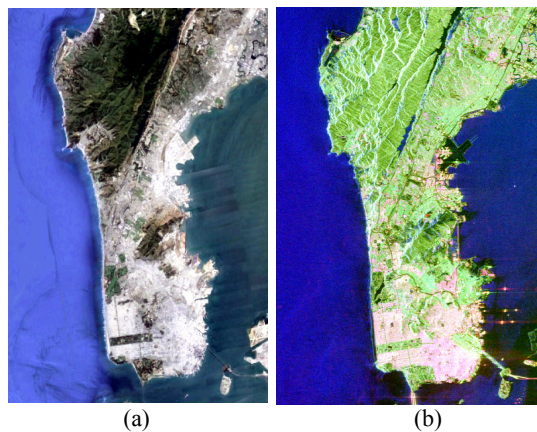
Figure 5.10 Study area and PALSAR data. (a) Optical image from Google Earth. (b) Pauli coded PALSAR image (Red: HH-VV, green: HV, blue: HH+VV).

Figure 5.11 (a)-(c) show the man-made target detection results of three methods and Figure 5.11 (d) overlays the proposed detection result on Pauli image. We can see that even though the original nonstationarity detection method can extract man-made targets effectively, the forests (marked with red circle) are also incorrectly detected. In contrast, the proposed method can remove most of the natural areas and also can detect the man-made targets. Detailed comparisons and discussions can be found in Paper 2.
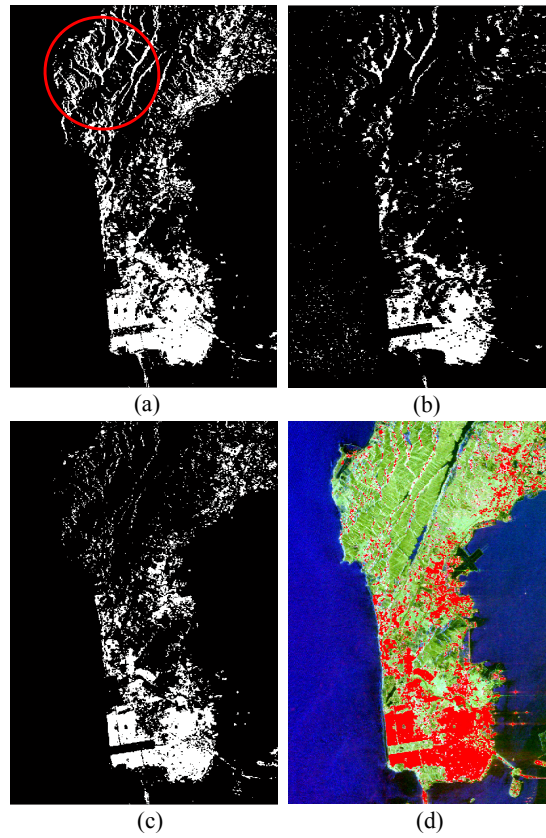
Figure 5.11 Man-made target detection results of (a) original nonstationarity detection method, (b) nonstationarity detection method with nonzero-mean statistical model, and (c) the proposed method. (d). Detection results (red) of the proposed method overlaid Pauli image.

5.3 Edge Detection

The edge detection results of Paper 4 are displayed in this section. Two PolSAR datasets are chosen to demonstrate the effectiveness of the

proposed method. The first one was acquired by ESAR L band system with study area located in Oberpfaffenhofen, Germany. The second one is a PiSAR L band image from Tsukuba, Japan. These two datasets cover on both urban and natural areas.

Figure 5.12 (a) and Figure 5.12 (b) give the two Pauli coded images, respectively. The red channel describes double-bounce scattering, the green channel describes volume scattering, and the blue channel describes surface scattering. There are a lot of man-made buildings in Figure 5.12 (a), which is a heterogeneous urban area. In Figure 5.12 (b), apart from the buildings, there are also a lot of farms.

| (a) | (b) |
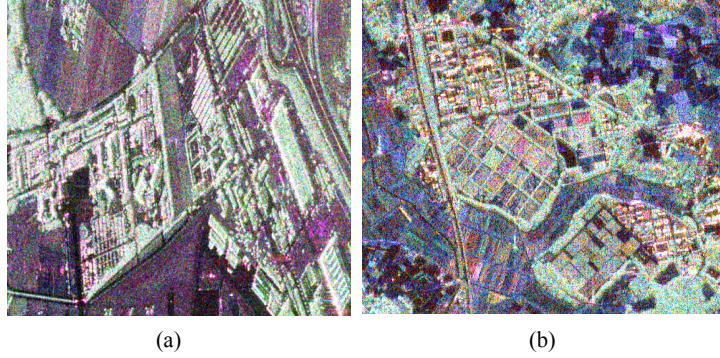
Figure 5.12 Two Pauli coded datasets. (a) ESAR image. (b). PiSAR image.

5.3.1 Comparisons and Analysis in Urban Areas

Before displaying the edge detection results, some parameters should be discussed. In normalized covariance matrix estimation, we set the parameters according to (Vasile et al. 2008), which shows good performance in heterogeneous urban areas. The coefficient of variation δ equals 3. The upper limit of neighbour pixels *nThre* is set to 30. $T_{\text{low}}, T_{\text{high}}$ are set to 1.66 and 5, respectively. In this experiment, two existing edge detection methods, i.e., the traditional CFAR edge detector (Schou et al. 2003) proposed by Schou et al. (T-CFAR hereafter) and the edge detector based on degenerate filter (Liu, Zhang, Liu, et al. 2014) proposed by Liu et al. (D-CFAR) are chosen for comparison. In addition, we also implement the traditional CFAR edge detector with Gauss-shaped filter (G-CFAR). The parameters $d_{\text{f}}, \theta_{\text{f}}$ in four methods are set to 1 and $\pi/8$, respectively. l_{f} and w_{f}, which are the window length and width in T-CFAR and D-CFAR, are set to 11 and 5, respectively. This

setting works fine for various scenes according to (Liu, Zhang, Liu, et al. 2014). To ensure that the window areas of different methods approximate the same, the parameters σ_x and σ_y in G-CFAR and our proposed method are set to 6.4 and 3.1, respectively. The probability of false alarm is set to 1% for all of the methods.
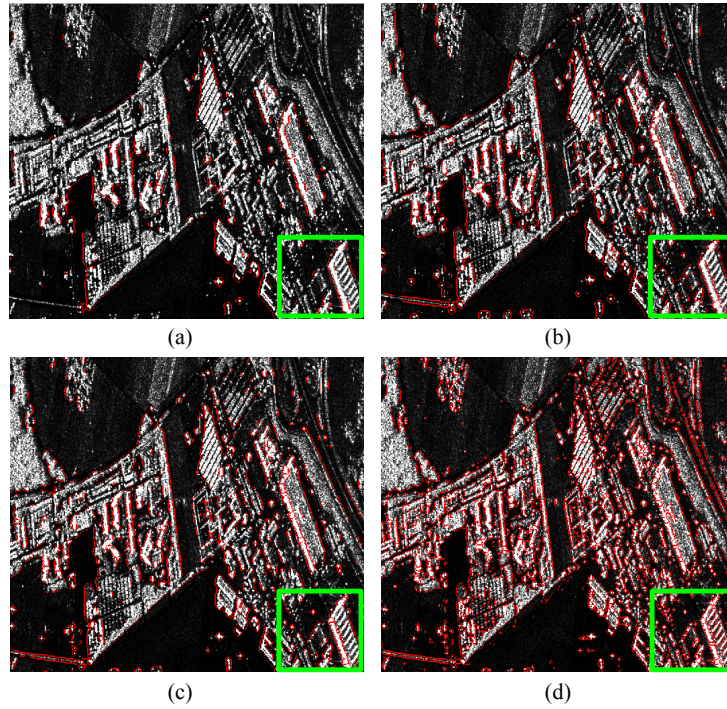
Figure 5.13 Overlay display of the final detected edges on span image (ESAR). (a) T-CFAR. (b) D-CFAR. (c) G-CFAR. (d) The proposed method.

After thresholding and morphological operations, we get the final detected edges overlaid on span image, which are shown in Figure 5.13. We can see that the results of Figure 5.13 (d) are fairly good, where most of the edges can be effectively detected. To further compare the results in detail, we select one urban area (marked with green rectangle) and display the results, as shown in Figure 5.14. It can be observed that our proposed method can extract the urban edges very well, although some of the buildings are distributed with small sizes. In contrast, lots of the edges of buildings are missed by the other methods. We can also see that the locations of the detected edges in Figure 5.14 (d) are more accurate, which demonstrates the effectiveness of our proposed method.
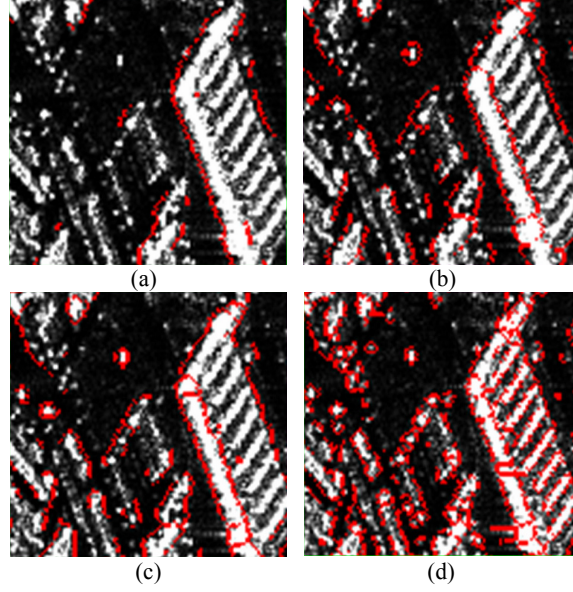
Figure 5.14 Enlarged edge detection results of urban area by (a) T-CFAR, (b) D-CFAR, (c) G-CFAR and (d) the proposed method, respectively.

To further evaluate the edge detection performance quantitatively, similar to (Liu, Zhang, Liu, et al. 2014), we also use the measures of precision and recall. Precision is the fraction of edge detections that are true positives rather than false positives, whereas recall is the fraction of true positives that are detected rather than missed. Figure 5.15 gives the results of different detection methods. It should be pointed out that the detector is better if its precision and recall curve lies in the upper right side of those of other detectors. From Figure 5.15, we can observe that the recalls of D-CFAR and G-CFAR are similar and much higher than that of T-CFAR when the precision is high. This is because D-CFAR and G-CFAR can extract edges more effective than T-CFAR. Since our proposed method can detect edges quite well, particularly in heterogeneous urban areas, as shown in Figure 5.15, the recall achieves the highest among different methods. It also can be seen that when the recall is high, the precision of the proposed method is still the highest, indicating that the locations of the detected edges are correct.
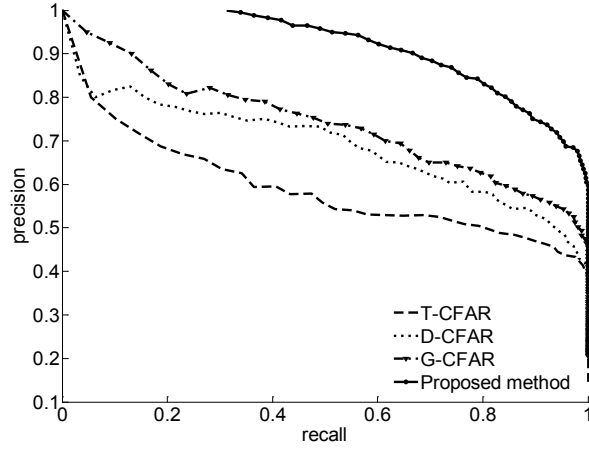
Figure 5.15 Precision and recall curves of different edge detection methods.

5.3.2 Comparisons and Analysis in Natural Areas

To further evaluate the effectiveness on natural areas, in this section, we choose PiSAR data which cover buildings and farms for edge detection evaluation. Figure 5.16 shows the final detected edges overlaid on the span image by different methods.
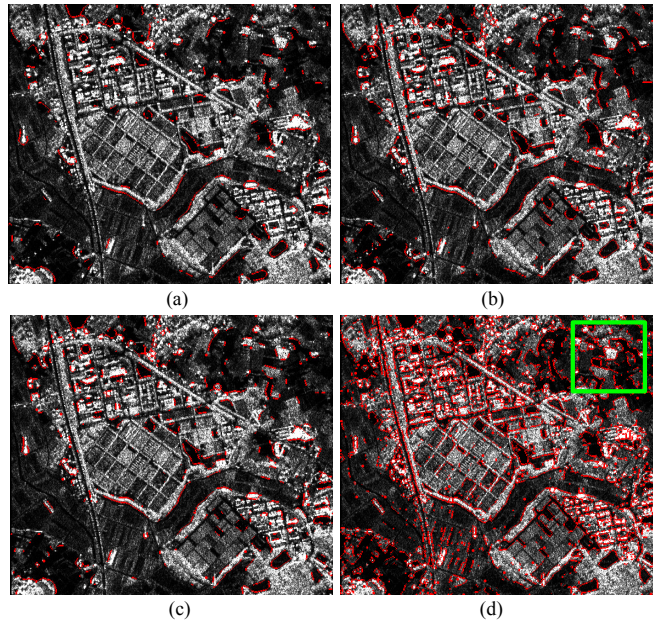
Figure 5.16 Overlay display of the final detected edges on span image (PiSAR). (a) T-CFAR. (b) D-CFAR. (c) G-CFAR. (d) The proposed method.

75

From Figure 5.16, it is clear that D-CFAR and G-CFAR still perform better than T-CFAR. The edge locations are accurate. However, there are still some edges of buildings missed, which decreases the detection accuracy. In contrast, our proposed method achieves much better result, where both urban and natural edges are well detected. This indicates that Gauss-shaped filter and SIRV model can effectively improve the edge detection accuracy. To view the results of natural areas in detail, we select one area in Figure 5.16 (d) and enlarge the results in Figure 5.17, where we can see that most of the edges in natural areas can be well extracted.

(a)   (b)
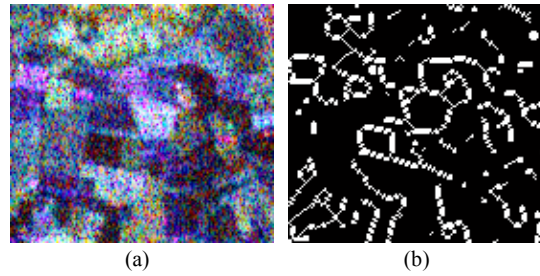
Figure 5.17 Pauli image (a) and the edge detection results (b) of natural areas marked in Figure 5.16 (d).

Since Paper 3 and Paper 4 are both related to urban extraction using ESAR data, here we have a discussion on the relationship between target detection and edge detection. The target detection mainly discriminates the man-made targets from the natural areas, therefore, the number of detected man-made pixels plays a key role in the accuracy evaluation. In contrast, edge detection focuses on the locations of the targets. If we consider the edge information in the target detection approach, there is an advantage, i.e., the man-made target detection results can be refined. The isolated pixels can be removed and the target edges can be accurately located, which will improve the detection accuracy. Therefore, a logical AND operator using the edge information can be used as a post-processing step for the final man-made target detection result.

5.4   Urban Area Classification and Segmentation

This section gives the urban area classification results using scattering powers obtained by decomposition procedure one. The objective is to resolve ortho and oriented urban area misclassifications, as discussed in Paper 5. Discrimination abilities of various scattering components are

analysed firstly, followed by the classification results. Then we show the superpixel generation and segmentation results. The pixel-based classification result is further improved with object-based processing, which regards the superpixels as objects.

5.4.1 Discrimination Abilities of Various Scattering Components

Figure 5.18 presents the scatter diagrams of different targets using RADARSAT-2 data, where x-axis and y-axis indicate double-bounce and volume scattering power, respectively. Z-axis represents one of helix, wire, and cross scattering power. The ortho buildings, oriented buildings and vegetated areas are represented by red points, black points, and green points, respectively.
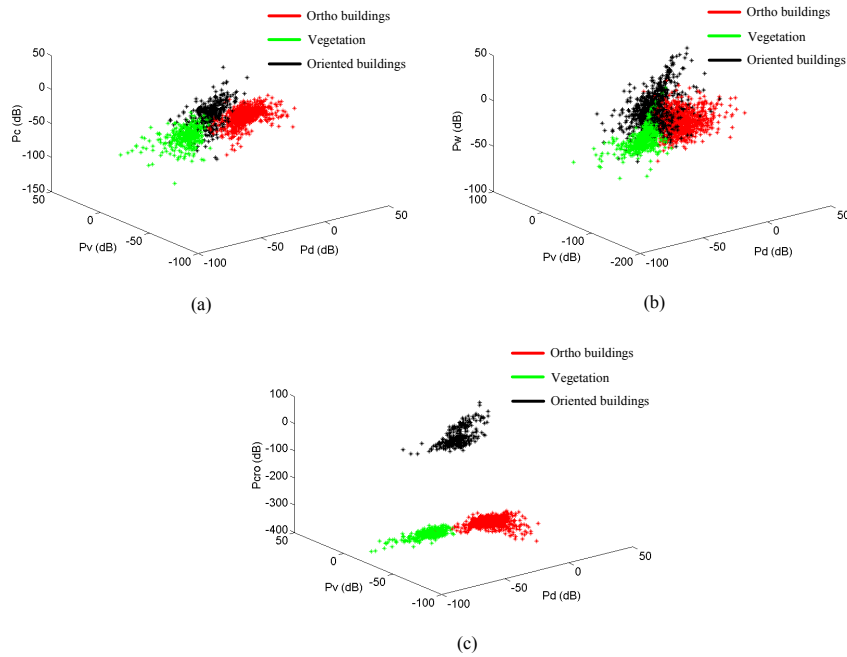
Figure 5.18 The scatter diagrams of ortho buildings (red points), vegetation (green points), and oriented buildings (black points) in three different decomposed powers. (a) Double-bounce, volume, and helix scattering diagrams; (b) Double-bounce, volume, and wire scattering diagrams; (c) Double-bounce, volume, and cross scattering diagrams.

What we can see from Figure 5.18 (c) is that the oriented buildings and vegetation can be clearly discriminated using cross scattering power

although oriented buildings have quite strong volume scattering, which is similar to vegetation. Moreover, it can be found that oriented and ortho buildings are also clearly distinguished. The results in Figure 5.18 (a) and Figure 5.18 (b) are not good, where vegetation and oriented buildings are seriously mixed. It can be found that the distribution of helix scattering is similar to that of wire scattering, which is in accordance with previous analysis. Even though helix scattering and wire scattering are both dominant in oriented urban areas, they also have strong values in vegetated and ortho urban areas. Overall, compared to helix and wire scattering, the proposed cross scattering can exploit more urban information from the PolSAR data, which makes it more suitable for urban area analysis.

5.4.2 Comparison of Classification Results with Different Decomposition Methods

In this research, we use unsupervised K-means classifier to classify urban areas based on the scattering powers. The four land cover classes are ortho buildings, oriented buildings, vegetation and water, respectively. It should be noted that this approach is pixel-based processing. Superpixel-based classification results will be shown in the following subsections.

The classification results of different methods, as well as the SPAN image are shown in Figure 5.19. It can be seen from Figure 5.19 (a) that using MCSM scattering powers, the oriented buildings and vegetated areas cannot be clearly separated. The reason is that wire scattering power difference between oriented buildings and vegetation is small, leading to low separation ability. Furthermore, it can be observed that the ortho and oriented buildings are slightly mixed, such as the urban area marked with white circle. Compared to the classification result using MCSM scattering powers, the classification result in Figure 5.19 (b) seems even worse. There are lots of misclassifications between oriented buildings and vegetation, as well as ortho buildings. In contrast, our method (Figure 5.19 (c)) can obtain quite promising classification result due to the cross scattering power, where the ortho buildings, oriented buildings and vegetated areas are all well classified.
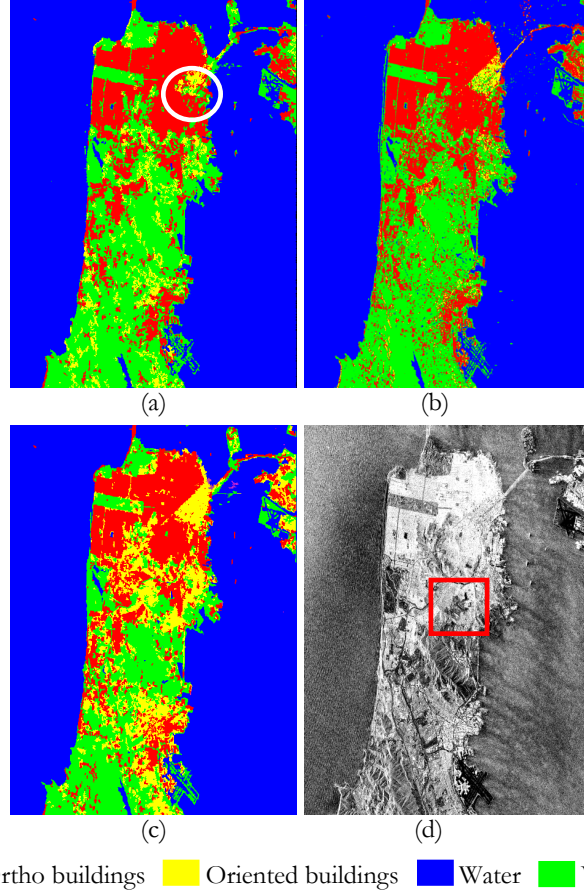
Figure 5.19 Classification results of RADARSAT-2 image. (a)-(c) K-means classification results with MCSM, Y4R, and the proposed decomposed scattering powers, respectively (d) SPAN image.

To compare the classification results in detail, the area marked with red rectangle in Figure 5.19 (d) is selected and the different classification results are enlarged in Figure 5.20. It is obvious that three methods can effectively discriminate the ortho buildings. Nevertheless, the results of oriented buildings are quite different, such as the two areas marked with red rectangles in Figure 5.20 (b). From Figure 5.20 (c), we can see that although some oriented buildings can be correctly classified using MCSM decomposed scattering powers, there still exist a lot of misclassifications, which decrease the overall accuracy. For instance, some oriented buildings are classified as vegetation. Moreover, some ortho buildings are misclassified as oriented buildings, such as the area marked with red ellipse. It can be seen from Pauli coded image that this

79

area has double-bounce scattering and should be classified as ortho buildings. What we can see from Figure 5.20 (d) is that the scattering powers of Y4R have lower ability to discriminate oriented buildings from ortho buildings and vegetation than MCSM. In contrast, our proposed method achieves a better classification result, as shown in Figure 5.20 (e). Even though there are still some confusions between ortho and oriented buildings, most of the oriented buildings can be well classified.
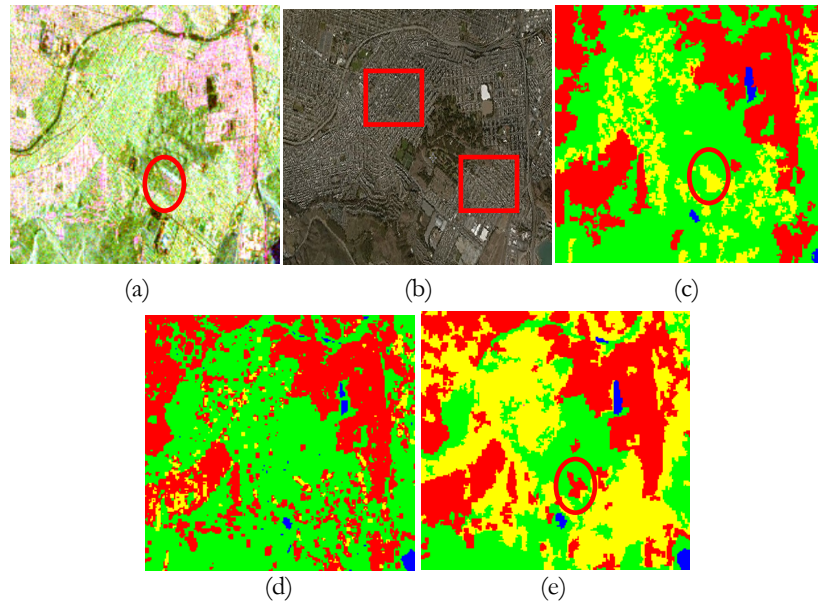
Figure 5.20 Detailed classification results of the selected patch. (a) Pauli coded PolSAR image. (b) Optical image. (c)-(e) K-means classification results with MCSM, Y4R, and the proposed decomposed scattering powers, respectively.

Finally, the classification accuracies of different methods are listed in Table 5.6. From Table 5.6 and Figure 5.20, we can conclude that the proposed classification method performs very well. The total accuracy achieves 88.3%, which is about 6.3% and 15.5% higher than other two methods, respectively. It is worth pointing out that in our method, the individual classification accuracy of oriented buildings plays a key role in the overall classification accuracy, which is 86.4%. In contrast, the results of MCSM and Y4R are much lower, which are only 65.4% and 38.8%, respectively. Hence, it can be demonstrated that the cross scattering is effective for urban area classification. Further detailed classification results and comparisons can be found in Paper 5.

Table 5.6 Classification accuracies of different methods (RADARSAT-2 image)

Class	MCSM	Proposed	Y4R
Ortho buildings	0.882	0.911	0.853
Oriented buildings	0.654	0.864	0.385
Water	0.924	0.913	0.893
Vegetation	0.821	0.848	0.782
Overall accuracy	0.82	0.883	0.728

5.4.3 Superpixel Generation

Figure 5.21 gives the superpixel generation results of ESAR dataset using Liu's (Liu et al. 2013), Qin's (Qin, Guo, and Lang 2015), and our proposed methods, respectively. The numbers of superpixel are all set to 2200.

To further compare the results in detail, two subareas marked with yellow rectangles A and B are selected from Figure 5.21 (c)-(f) and are shown in Figure 5.22. Area A mainly includes the buildings while Area B covers natural targets, as well as some man-made targets. Figure 5.21 (a), (c), and (e) present the final superpixel maps of three methods, where the red lines superimposed onto the Pauli images depict the superpixel boundaries. Figure 5.21 (b), (d), and (f) give the corresponding representation maps, in which the coherency matrix of each pixel is replaced by the average coherency matrix of the superpixel this pixel belongs to. From Figure 5.21 (a) and (b), we can see that the edges of the superpixels are very smooth, and the shape of the superpixels is quite regular. In natural areas, the results are acceptable. However, in urban areas, these superpixels cannot adhere well to image edges, the points and lines in the image are not preserved and most urban information is lost. Compared with Figure 5.21 (a), the result in Figure 5.21 (c) seems much better, where most of the edges and points are preserved. The superpixels can well adhere to image boundaries and capture the local information. However, the shape of the superpixel is very irregular and the edges are not smooth, even in the homogeneous natural areas, as shown in Figure 5.22 (a) and (e). In this method, to well preserve the edges and points, the trade-off factor which balances the polarimetric similarity and spatial proximity was set to 1.0. Therefore, the polarimetric similarity overweighs spatial proximity, leading to irregular superpixels. Moreover, it can be seen that there are still some problems in urban areas, such as discontinuities, artifacts, and missed detections, which are shown in Figure 5.22 (c) and (g).
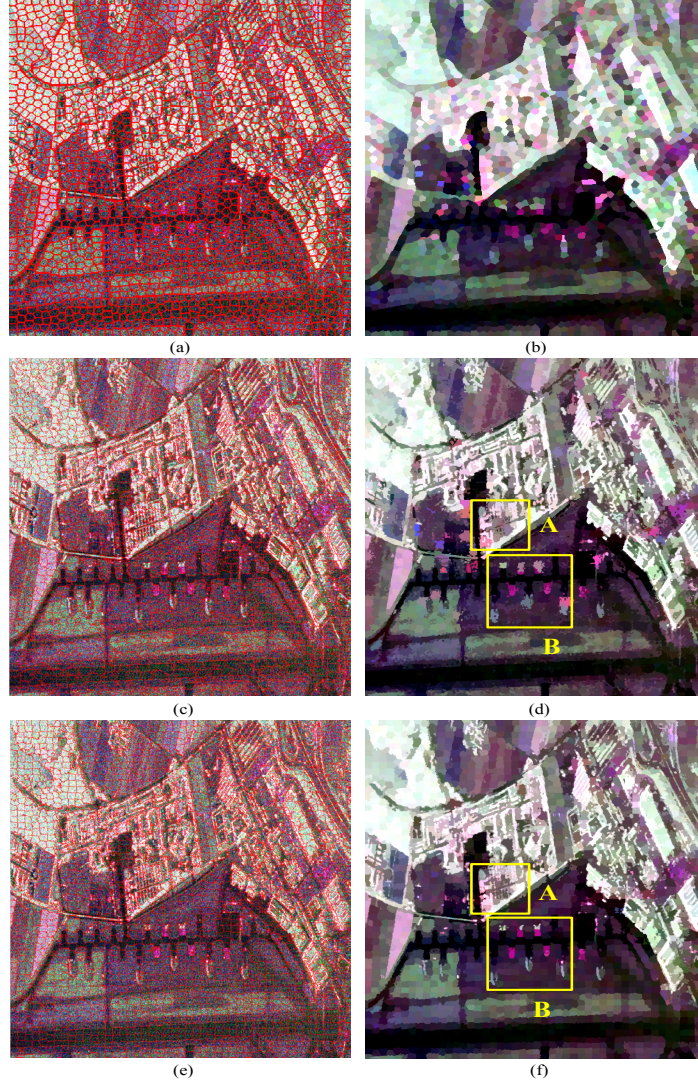
Figure 5.21 Superpixel generation results of Liu's, Qin's, and our proposed approaches with K = 2200 for ESAR image. The first column denotes the final superpixel maps of different methods. The red lines superimposed onto the Pauli images depict the superpixel boundaries. The second column gives the representation maps, where the coherency matrix of each pixel is replaced by the average value of the superpixel this pixel belongs to.

The results in Figure 5.21 (e) and (f) indicate that our proposed algorithm can generate promising superpixels for PolSAR images. The target points and edges can be preserved very well. Moreover, the compactness of the superpixels is adaptive. In homogeneous areas, the

edges of superpixels are very smooth and the superpixel shape is quite regular, which can be seen in Figure 5.22 (b) and (f). This is because in such areas, the homogeneity measurement is high, making the spatial proximity overweigh other two similarities. Therefore, the superpixels are compact and regular. In contrast, within heterogeneous areas, the homogeneity measurement is low. To preserve the detailed information, spatial proximity is not as important as polarimetric and texture similarities any more. Therefore, the superpixels have irregular shape and can well preserve the image edges and points. From Figure 5.22, we can also see that in heterogeneous areas, our method can achieve better results than Qin's method, where the building edges are clearer and the man-made targets are better extracted. This is because our new edge detector based on SIRV product model can detect more accurate edges. In addition, the proposed distance measure considers more local information for superpixel generation, such as the span information.
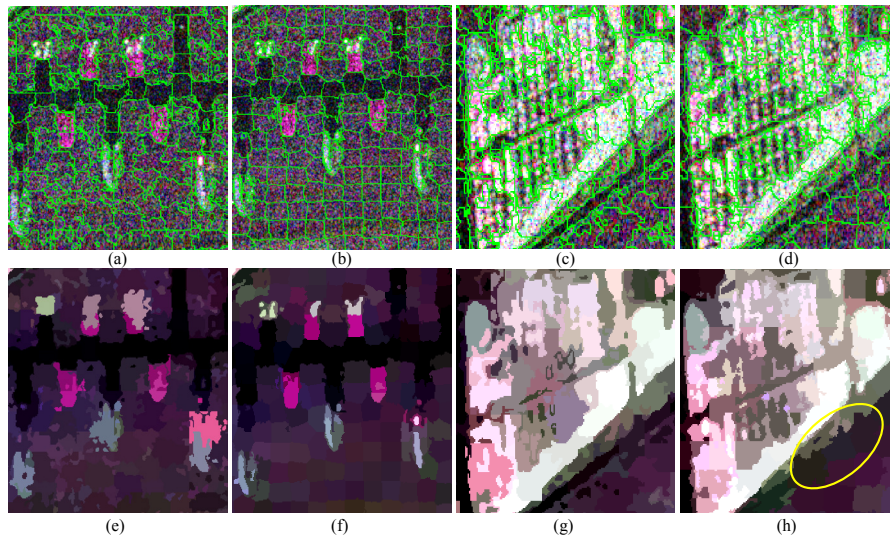
Figure 5.22 Comparison of detailed superpixel generation results in area A and B. The first row denotes the final superpixel maps. The green lines superimposed onto the Pauli images depict the superpixel boundaries. The second row gives the corresponding representation maps. (a) and (b) are the results of area B in Figure 5.17 (c) and (e), respectively. (c) and (d) are the results of area A in Figure 5.17 (c) and (e), respectively.

It should be noted that there are still some unsatisfactory results in homogeneous areas using our method, such the area marked with yellow ellipse in Figure 5.22 (h). The edges between two natural areas are

not well preserved. The reason is that SIRV product model is more suitable for non-Gaussian areas. Although some of the natural edges cannot be well detected, the superpixels are still acceptable. From the above analysis, it can be concluded that the superpixels generated by our method provide very smooth approximations in homogeneous areas, and also keep details in heterogeneous areas.

There are several benchmarks proposed for superpixel evaluation, in this study, to perform a quantitative comparison of different methods, we adopt two commonly used evaluation metrics: i.e., boundary recall (BR) (Arbelaez et al. 2011) and achievable segmentation accuracy (ASA) (Liu et al. 2011). BR is defined as the fraction of ground truth boundaries correctly recovered by the superpixel edges. If a true boundary pixel falls within 2 pixels from at least one superpixel edge, it can be regarded to be recovered correctly. Therefore, a high BR indicates that the superpixels can well adhere to image edges and very few true boundaries are missed. ASA is defined as the highest achievable accuracy of object segmentation when regarding the superpixels as units. By labeling each superpixel with the ground truth segments of the largest overlapping area, ASA can be obtained as the fraction of labeled pixels that are not leaked from the ground truth boundaries. Thus a high ASA means that the superpixels comply well with objects in the PolSAR image. These two indicators can evaluate the final superpixel maps. Figure 5.23 and Figure 5.24 depict the BR and ASA of three methods with different numbers of superpixels, respectively. This number is set from 250 to 2500 with different step sizes.
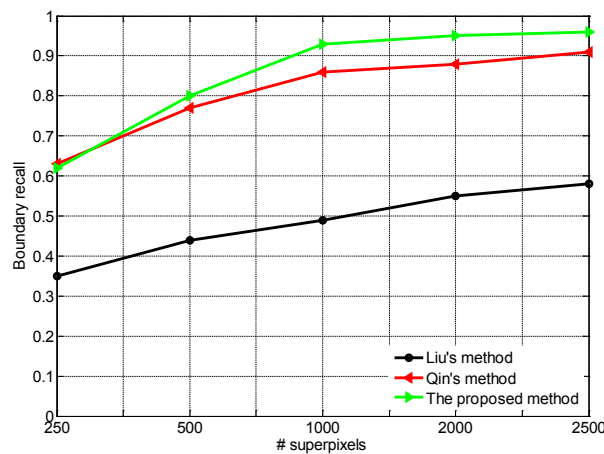
Figure 5.23 Boundary recall (BR) of three methods with different superpixel numbers.

According to these two figures, Liu's method performs the worst in terms of boundary adherence and achievable segmentation accuracy. In addition, another drawback is its extremely low time efficiency. Qin's method and our proposed method have similar BR when the superpixel number does not exceed 500. However, if we increase this value, our method has better boundary adherence than Qin's method. In Figure 5.24, these two methods have similar results but our method still performs slightly better than Qin's approach. Further quantitative evaluation and comparison can be found in Paper 6.
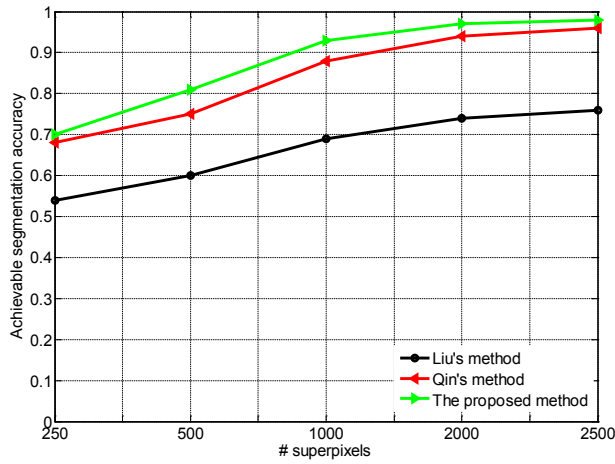
Figure 5.24 Achievable segmentation accuracy (ASA) of three methods with different superpixel numbers.

5.4.4 Comparison of Pixel-based and Object-based Classifications

To further demonstrate the capability of superpixels to improve the classification accuracy, we incorporate them into our unsupervised classification approach and then compare the superpixel-based results with the original pixel-based results. Two datasets, i.e., RADARSAT-2 and ESAR images are utilized in this subsection.

Figure 5.25 gives the classification results of RADARSAT-2 data with and without superpixels. Figure 5.25 (a) is the representation map after superpixel generation, Figure 5.25 (b) and (c) are the pixel-based and superpixel-based classification results, respectively. It can be seen that there are some isolated pixels and disconnected regions in Figure 5.25 (b). In contrast, the result in Figure 5.25 (c) is smoother thanks to the

superpixel segmentation. There are less false classifications and disconnected regions. Therefore, the superpixels generated by our method can be used as a pre-processing step for object-based classification.

(a)　　　　　　　　(b)　　　　　　　　(c)

🟥 Ortho buildings　🟨 Oriented buildings　🟦 Water　🟩 Vegetation
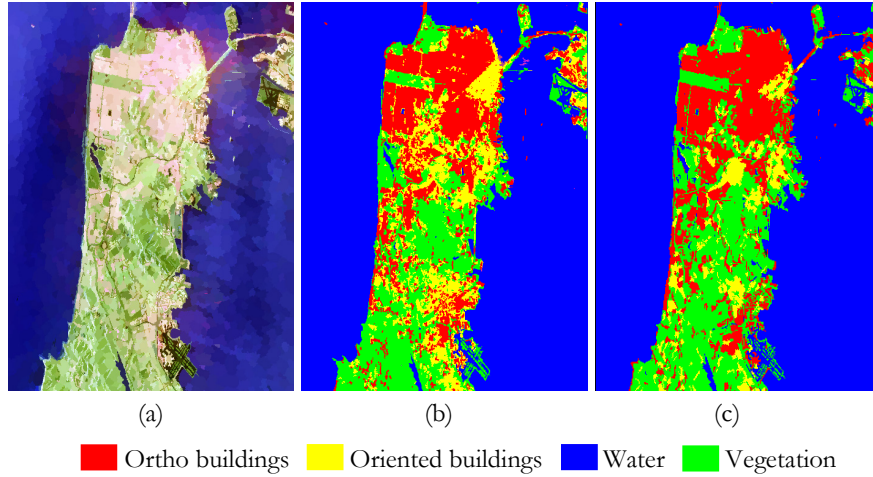
Figure 5.25 Classification results comparison of RADARSAT-2 data with and without superpixels. (a) Representation map after superpixel generation. (b) Pixel-based result. (c) Superpixel-based result.

(a)　　　　　　　　(b)　　　　　　　　(c)

🟥 Ortho buildings　🟨 Oriented buildings　⬜ Bare soil　🟩 Vegetation
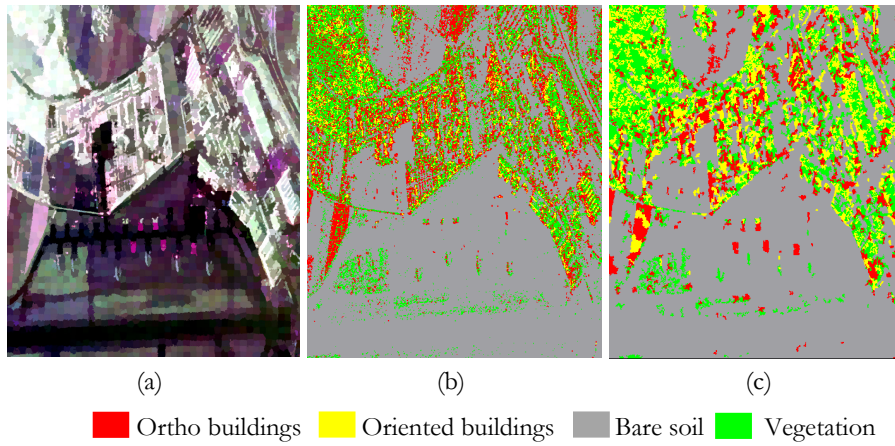
Figure 5.26 Classification results comparison of ESAR data with and without superpixels. (a) Representation map after superpixel generation. (b) Pixel-based result. (c) Superpixel-based result.

Figure 5.26 presents the classification results of ESAR data with and without superpixels. Figure 5.26 (b) is the pixel-based unsupervised classification result, which is not satisfactory. It should be noted that although some buildings have quite large polarization orientation angles,

leading to very strong cross scattering power; the forests also have cross scattering in this L-band ESAR data due to the microwave penetration. Therefore, there exist serious confusions between oriented buildings and vegetation. Here we only focus the effectiveness of superpixels on classification. From Figure 5.26 (b) and Figure 5.26 (c), it is apparent that superpixel-based classification outperforms pixel-based approach. The building objects are preserved well and the boundaries between different land covers are clearer. Therefore, we can conclude that the classification result can be refined using superpixels.

6 Conclusions and Future Research

6.1 Conclusions

This research investigated urban information extraction from PolSAR data, including urban scattering analysis, urban extraction, and urban classification and segmentation. The scattering components of buildings with different orientation angles are analysed and compared. The urban locations and areas can be accurately obtained in extraction stage while the ortho and oriented buildings can be discriminated in classification stage. In addition, the superpixels can be further used to refine the classification results, improving the overall accuracy. Considering the objectives of this research, specific conclusions can be drawn.

To distinguish ortho and oriented buildings, a new cross scattering model was proposed, which adaptively considers the building orientation angle. Unlike helix and wire scattering components, this cross scattering model mainly describes the HV scattering caused by oriented buildings. Two decomposition procedures are adopted to validate this cross scattering model. The decomposition results using RADARSAT-2 C-band data, AIRSAR and UAVSAR L-band data demonstrated that the proposed decomposition methods can generate cross scattering component for oriented buildings and can effectively enhance the urban characteristics (Paper 1, 2).

To solve the drawbacks of conventional nonstationarity detection method, the reflectance asymmetry of man-made targets was considered and an improved man-made target extraction method based on nonstationarity and asymmetry was proposed. By incorporating the asymmetry, natural areas with Bragg resonance are removed from the detection results, even though they also have nonstationarity like man-made targets. Furthermore, small man-made targets and metallic fences along the road are also clearly extracted, which demonstrates that the proposed approach performs better than original nonstationarity detection algorithm. Airborne ESAR data and spaceborne PALSAR data are utilized to demonstrate the performance of this detection method. It can be concluded that sub-aperture decomposition is beneficial for man-made target detection, especially for oriented buildings. The nonstationarity detection method with nonzero-mean statistical model performs better than the original nonstationarity detection method with Wishart distribution for high resolution PolSAR data; however, these

two methods cannot remove natural areas with Bragg resonance. In contrast, the proposed method has a better discriminative ability than the other two methods for airborne and spaceborne PolSAR data (Paper 3).

After analysing the shortcomings of conventional edge detectors for PolSAR data, a new edge detection approach using Gauss-shaped filter and SIRV model was proposed. This method was shown to be suitable for heterogeneous urban areas where the Wishart distribution is violated. The edges of urban and natural areas can be both effectively extracted, in addition, the locations are also more accurate. Edge detection of urban areas is beneficial for superpixel generation (Paper 4).

Based on the decomposed scattering powers, a K-means classifier is utilized to classify the urban areas. Using the cross scattering power, oriented buildings can be effective distinguished from ortho buildings and vegetation. Furthermore, the superpixel maps can be utilized as ancillary information to refine the classification results. Some small man-made targets and roads can be correctly classified with more accurate locations, which can improve the final accuracy. It is worth pointing out that the classification accuracy of natural areas is not high, such as water and bare soils. The reason is that the proposed decomposition method mainly works on urban areas, thus this classification approach cannot classify natural areas very well based on the scattering powers. But since this thesis focuses on urban information extraction, spatial or other features were not considered in the classification (Paper 5, Paper 6).

6.2 Future Research

Due to the limitation of data acquisition, this thesis only focuses on urban information extraction from one single PolSAR image acquired at single time. To further improve urban information extraction accuracy, the following topics will be investigated in the future.

[1] To overcome the limited information contained in PolSAR images acquired at single time, future research will investigate the use of multi-temporal PolSAR data. The urban scattering mechanisms can be well observed via change detection methods, which can supply useful information for target detection and classification.

[2] Instead of using PolSAR data with only polarimetric information, future research will investigate urban area information extraction using polarimetric interferometric SAR (PolInSAR) data.

Interferometric information will be used for urban analysis and new target detection and classification methods are necessary to be developed.

[3] Specific pattern recognition approaches such as Markov Random Field (MRF), Conditional Random Field (CRF), etc., for extraction of typical urban features will be studied. These features can be further used for urban analysis together with scattering mechanisms. Feature selection techniques also should be studied to reduce information redundancy.

[4] Finally, since object-based classification can achieve better results than pixel-based methods, the generated superpixels can be further used as a pre-processing step for classification. Feature extraction from superpixels should be studied in the future. Moreover, the man-made target detection should also be refined using the edge maps.

References

Achanta, Radhakrishna, Shaji, Appu, Smith, Kevin, Lucchi, Aurelien, Fua, Pascal, and Susstrunk, Sabine. 2012. SLIC superpixels compared to state-of-the-art superpixel methods. *IEEE Transactions on Pattern Analysis and Machine Intelligence* 34 (11):2274-2282.

Ainsworth, T. L., Jansen, R. W., Lee, J. S., and Fiedler, R. 1999. Sub-aperture analysis of high resolution polarimetric SAR data. *IEEE International Geoscience and Remote Sensing Symposium, 1999. IGARSS'99*, 1:41-43.

Ainsworth, T.L., Schuler, D.L., and Lee, J. S. 2008. Polarimetric SAR characterization of man-made structures in urban areas using normalized circular-pol correlation coefficients. *Remote Sensing of Environment* 112 (6):2876-2885.

Alonso-González, A., López-Martínez, C., and Salembier, P. 2012. Filtering and segmentation of polarimetric SAR data based on binary partition trees. *IEEE Transactions on Geoscience and Remote Sensing* 50 (2):593-605.

An, W., Cui, Y., and Yang, J. 2010. Three-component model-based decomposition for polarimetric SAR data. *IEEE Transactions on Geoscience and Remote Sensing* 48 (6):2732-2739.

Anfinsen, S., Eltoft, T., and Doulgeris, A. 2009. A relaxed Wishart model for polarimetric SAR data. *Proc. PolInSAR*, Frascati, Italy,

Anfinsen, Stian Normann, Doulgeris, Anthony P, and Eltoft, Torbjørn. 2009. Estimation of the equivalent number of looks in polarimetric synthetic aperture radar imagery. *IEEE Transactions on Geoscience and Remote Sensing* 47 (11):3795-3809.

Anfinsen, Stian Normann, Jenssen, Robert, and Eltoft, Torbjørn. 2007. Spectral clustering of polarimetric SAR data with Wishart-derived distance measures. *Proc. POLinSAR*, 7

Antropov, O. 2014. Land cover and forest mapping in boreal zone using polarimetric and interferometric SAR data. Aalto University.

Antropov, O., Rauste, Y., and Hame, T. 2011a. Volume scattering modeling in PolSAR decompositions: Study of ALOS PALSAR data over boreal forest. *IEEE Transactions on Geoscience and Remote Sensing* 49 (10):3838-3848.

Antropov, Oleg, Rauste, Yrjo, and Hame, Tuomas. 2011b. Volume scattering modeling in PolSAR decompositions: Study of ALOS PALSAR data over boreal forest. *IEEE Transactions on Geoscience and Remote Sensing* 49 (10):3838-3848.

Arbelaez, Pablo, Maire, Michael, Fowlkes, Charless, and Malik, Jitendra. 2011. Contour detection and hierarchical image segmentation. *IEEE Transactions on Pattern Analysis and Machine Intelligence* 33 (5):898-916.

Arii, M., Zyl, J. J., and Kim, Y. 2011. Adaptive model-based decomposition of polarimetric SAR covariance matrices. *IEEE Transactions on Geoscience and Remote Sensing* 49 (3):1104-1113.

Armando, M. 2012. *A new target detector based on geometrical perturbation filters for Polarimetric Synthetic Aperture Radar (POL-SAR)*: Springer Science & Business Media.

Azmedroub, B, and Ouarzeddine, M. 2015. Urban areas detection using polarimetric SAR images. *IEEE International Geoscience and Remote Sensing Symposium (IGARSS 2015)* 3227-3230.

Ban, Y., H. Hu and I. Rangel, 2010. Fusion of QuickBird MS and RADARSAT-1 SAR data for urban land-cover mapping: object-based and knowledge-based approach. *International Journal of Remote Sensing*, 31(6):1391-1410.

Ban, Y. and O. A. Yousif, 2012. Multitemporal spaceborne SAR data for urban change detection in China. *IEEE Journal on Selected Topics in Applied Earth Observations and Remote Sensing*, 5(4): 1087-1094.

Ban, Y. and A. Jacob, 2013. Object-based fusion of multitemporal multi-angle ENVISAT ASAR and HJ-1 multispectral data for urban land-cover mapping. *IEEE Transaction on GeoScience and Remote Sensing*, 51(4): 1998-2006.

Ban, Y., A. Jacob and P. Gamba, 2015. Spaceborne SAR data for global urban mapping at 30m resolution using a robust urban extractor. *ISPRS J. of Photogrammetry and Remote Sensing*, 103:28-37.

Barnes, C. F., and Burki, J. 2006. Late-season rural land-cover estimation with polarimetric-SAR intensity pixel blocks and σ-tree-structured near-neighbor classifiers. *IEEE Transactions on Geoscience and Remote Sensing* 44 (9):2384-2392.

Baum, Carl E. 2003. Symmetry in target recognition. *Interaction Note* 587.

Baum, CE. 1997. Symmetry in electromagnetic scattering as a target discriminant. *International Optical Science, Engineering and Instrumentation'97.*, 3120:295-307.

Bhattacharya, A, and Touzi, R. 2012. Polarimetric SAR urban classification using the Touzi target scattering decomposition. *Canadian Journal of Remote Sensing* 37 (4):323-332.

Bhattacharya, A., Muhuri, A., De, S., Manickam, S., and Frery, A. C. 2015. Modifying the Yamaguchi four-component decomposition scattering powers using a stochastic distance. *IEEE Journal of Selected Topics in Applied Earth Observations and Remote Sensing* PP (99):1-10.

Boerner, W. I., Mott, H., and Luneburg, E. 1997. Polarimetry in remote sensing: Basic and applied concepts. *IEEE International Geoscience and Remote Sensing, 1997. IGARSS'97*, 3:1401-1403.

Bombrun, L., and Beaulieu, J. M. 2008. Fisher distribution for texture modeling of Polarimetric SAR data. *IEEE Geoscience and Remote Sensing Letters* 5 (3):512-516. doi: 10.1109/LGRS.2008.923262.

Bombrun, L., Vasile, G., Gay, M., and Totir, F. 2011. Hierarchical segmentation of polarimetric SAR images using heterogeneous clutter models. *IEEE Transactions on Geoscience and Remote Sensing* 49 (2):726-737.

Bouvet A, Le Toan T, Lam-Dao N. 2009. Monitoring of the rice cropping system in the Mekong Delta using ENVISAT/ASAR dual polarization data. *IEEE Transactions on Geoscience and Remote Sensing* 47(2): 517-526.

Cameron, W., and Leung, L. 1990. Feature motivated polarization scattering matrix decomposition. *IEEE International Radar Conference 1990*, 1:549-557.

Cao, F., Hong, W., Wu, Y., and Pottier, E. 2007. An unsupervised segmentation with an adaptive number of clusters using the SPAN/H/α/A space and the

complex Wishart clustering for fully polarimetric SAR data analysis. *IEEE Transactions on Geoscience and Remote Sensing* 45 (11):3454–3467.

Cao, Y., Su, C., and Liang, J. 2012. Building unit density detection from high resolution TerraSAR-X image based on mathematical morphological operators. *IEEE International Geoscience and Remote Sensing Symposium (IGARSS 2012)* 5978-5981.

Chen, KS, Huang, WP, and Amar, F. 1996. Classification of multifrequency polarimetric SAR imagery using a dynamic learning neural network. *IEEE Transactions on Geoscience and Remote Sensing* 34 (3):814-820.

Chen, Q., Kuang, G., Li, J., Sui, L., and Li, D. 2013. Unsupervised land cover/land use classification using PolSAR imagery based on scattering similarity. *IEEE Transactions on Geoscience and Remote Sensing* 51 (3):1817-1825.

Chen, S. W., Li, Y. Z., and Wang, X. S. 2014. Modeling and interpretation of scattering mechanisms in polarimetric synthetic aperture radar: advances and perspectives. *IEEE Signal Processing Magazine* 31 (4):79-89.

Chen, S. W., Li, Y. Z., Wang, X. S., Koyama, C. N., and Sato, M. 2015. Urban damage mapping using scattering mechanism investigation technique for fully polarimetric SAR data. *IEEE International Geoscience and Remote Sensing Symposium (IGARSS 2015)*:3790-3793.

Chen, S. W., Ohki, M., Shimada, M., and Sato, M. 2013. Deorientation effect investigation for model-based decomposition over oriented built-up areas. *IEEE Geoscience and Remote Sensing Letters* 10 (2):273-277.

Chen, S. W., and Sato, M. 2013. Tsunami damage investigation of built-up areas using multi-temporal spaceborne full polarimetric SAR images. *IEEE Transactions on Geoscience and Remote Sensing* 51 (4):1985-1997.

Chen, S. W., Wang, X. S., Li, Y. Z., and Sato, M. 2014. Adaptive model-based polarimetric decomposition using PolInSAR coherence. *IEEE Transactions on Geoscience and Remote Sensing* 52 (3):1705-1718.

Chen, S. W., Wang, X. S., and Sato, M. 2014. Uniform polarimetric matrix rotation theory and its applications. *IEEE Transactions on Geoscience and Remote Sensing* 52 (8):4756-4770.

Cheng, J., Ji, Y., and Liu, H. 2015. Segmentation-based PolSAR image classification using visual features: RHLBP and color features. *Remote Sensing* 7 (5):6079-6106.

Cheng, J., Liu, J., and Xu, Y. 2013. Superpixel classification based optic disc and optic cup segmentation for glaucoma screening. *IEEE Transactions on Medical Imaging* 32 (6):1019-1032.

Cloude, S. 2009. *Polarisation: applications in remote sensing*: OUP Oxford.

Cloude, S. R. 1992. Lie groups in electromagnetic wave propagation and scattering. *Journal of electromagnetic waves and applications* 6 (7):947-974.

Cloude, S. R., and Pottier, E. 1997. An entropy based classification scheme for land applications of polarimetric SAR. *IEEE Transactions on Geoscience and Remote Sensing* 35 (1):68-78.

Cloude, SR, and Pottier, E. 1996. A review of target decomposition theorems in radar polarimetry. *IEEE Transactions on Geoscience and Remote Sensing* 34 (2):498-518.

Collins, M. J., Denbina, M., Minchew, B., Jones, C., and Holt, B. 2015. On the use of simulated airborne compact Polarimetric SAR for characterizing oil–

water mixing of the deepwater horizon oil spill. *IEEE Journal of Selected Topics in Applied Earth Observations and Remote Sensing* 8 (3):1062-1077.

Comaniciu, Dorin, and Meer, Peter. 2002. Mean shift: A robust approach toward feature space analysis. *IEEE Transactions on Pattern Analysis and Machine Intelligence* 24 (5):603-619.

Cui, Y., Yamaguchi, Y., and Yang, J. 2014. On complete model-based decomposition of polarimetric SAR coherency matrix data. *IEEE Transactions on Geoscience and Remote Sensing* 52 (4):1991-2001.

Cuong T Q, Minh D H T, Le Toan T. 2015. Ground subsidence monitoring in Vietnam by multi-temporal InSAR technique. *IEEE International Geoscience and Remote Sensing Symposium (IGARSS)* :3540-3543.

Dabboor, M., Collins, M. J., Karathanassi, V., and Braun, A. 2013. An unsupervised classification approach for polarimetric SAR data based on the chernoff distance for complex wishart distribution. *IEEE Transactions on Geoscience and Remote Sensing* 51 (7):4200-4213.

Davidson M W J, Le Toan T, Mattia F, et al. 2000. On the characterization of agricultural soil roughness for radar remote sensing studies. *IEEE Transactions on Geoscience and Remote Sensing* 38(2): 630-640.

De, S., and Bhattacharya, A. 2015. Urban classification using PolSAR data and deep learning. *IEEE International Geoscience and Remote Sensing Symposium (IGARSS 2015)* 353-356.

Dell'Acqua F, Gamba P. 2006. Discriminating urban environments using multiscale texture and multiple SAR images. *International Journal of Remote Sensing* 27(18): 3797-3812.

Dell'Acqua F, Gamba P. 2003a. Texture-based characterization of urban environments on satellite SAR images. *IEEE Transactions on Geoscience and Remote Sensing* 41(1): 153-159.

Dell'Acqua F, Gamba P, Lisini G. 2003b. Improvements to urban area characterization using multitemporal and multiangle SAR images. *IEEE Transactions on Geoscience and Remote Sensing* 41(9): 1996-2004.

Dell'Acqua F, Gamba P. 2001. Detection of urban structures in SAR images by robust fuzzy clustering algorithms: the example of street tracking. *IEEE Transactions on Geoscience and Remote Sensing* 39(10): 2287-2297.

Dell'Acqua F, Gamba P, Odasso L, et al. 2009. Segment-based urban block outlining in high-resolution SAR images. *IEEE 2009 Joint Urban Remote Sensing Event* 1-6.

Deng, L, and Wang, C. 2014. Improved building extraction with integrated decomposition of time-frequency and entropy-alpha using polarimetric SAR data. *IEEE Journal of Selected Topics in Applied Earth Observations and Remote Sensing* 7 (10):4058-4068.

Deng, L, Yan, Y, and Sun, C. 2015. Use of sub-aperture decomposition for supervised PolSAR classification in urban area. *Remote Sensing* 7 (2):1380-1396.

Deng, J and Y. Ban et al., 2014. Hierarchical segmentation of multitemporal RADARSAT-2 SAR data using stationary wavelet transform and algebraic multigrid method. *IEEE Transaction on GeoScience and Remote Sensing* 52(7): 4353-4363.

Doulgeris, A. P. 2015. An automatic-distribution and Markov Random Field segmentation algorithm for PolSAR images. *IEEE Transactions on Geoscience and Remote Sensing* 53 (4):1819-1827.

Esch, T., Thiel, M., Schenk, A., Roth, A., Muller, A., and Dech, S. 2010. Delineation of urban footprints from TerraSAR-X data by analyzing speckle characteristics and intensity information. *IEEE Transactions on Geoscience and Remote Sensing* 48 (2):905-916.

Feng, Jilan, Cao, Zongjie, and Pi, Yiming. 2014. Polarimetric contextual classification of PolSAR images using sparse representation and superpixels. *Remote Sensing* 6 (8):7158-7181.

Ferro-Famil, L, and Lavalle, M. 2009. Detection and analysis of urban areas using ALOS PALSAR polarimetric data. *IEEE International Geoscience and Remote Sensing Symposium, IGARSS 2009*, 5:V-142-V-145.

Ferro-Famil, L., E., Pottier, and Lee, JS. 2001. Unsupervised classification of multifrequency and fully polarimetric SAR images based on the H/A/Alpha-Wishart classifier. *IEEE Transactions on Geoscience and Remote Sensing* 39 (11):2332-2342.

Ferro-Famil, L., and Pottier, E. 2007. Urban area remote sensing from L-band PolSAR data using Time-Frequency techniques. *Urban Remote Sensing Joint Event, 2007*:1-6.

Ferro-Famil, L., Reigber, A., and Pottier, E. 2005. Nonstationary nutural media analysis from polarimetric sar data using a two-dimensional time-frequency decompostion approach. *Canadian Journal of Remote Sensing* 31 (1):21–29.

Ferro-Famil, L., Reigber, A., Pottier, E., and Boerner, W. M. 2003. Scene characterization using subaperture polarimetric SAR data. *IEEE Transactions on Geoscience and Remote Sensing* 41 (10):2264-2276.

Fjortoft, R., Lopes, A., Marthon, P., and Cubero-Castan, E. 1998. An optimal multiedge detector for SAR image segmentation. *IEEE Transactions on Geoscience and Remote Sensing* 36 (3):793-802. doi: 10.1109/36.673672.

Freeman, A, and Durden, SL. 1998. A three-component scattering model for polarimetric SAR data. *IEEE Transactions on Geoscience and Remote Sensing* 36 (3):963-973.

Freeman, A. 2007. Fitting a two-component scattering model to polarimetric SAR data from forests. *IEEE Transactions on Geoscience and Remote Sensing* 45 (8):2583-2592.

Freitas, Corina C, Frery, Alejandro C, and Correia, Antonio H. 2005. The polarimetric *Environmetrics* 16 (1):13-31.

Frery, A. C., Müller, H. J., Yanasse, C., and Anna, S. 1997. A model for extremely heterogeneous clutter. *IEEE Transactions on Geoscience and Remote Sensing* 35 (3):648-659.

Frery, A. C., Nascimento, A. D. C., and Cintra, R. J. 2014. Analytic expressions for stochastic distances between relaxed complex Wishart distributions. *IEEE Transactions on Geoscience and Remote Sensing* 52 (2):1213-1226.

Gamba P, Dell'Acqua F, Lisini G. 2006. Change detection of multitemporal SAR data in urban areas combining feature-based and pixel-based techniques. *IEEE Transactions on Geoscience and Remote Sensing* 44(10): 2820-2827.

95

Goodman, Joseph W. 1976. Some fundamental properties of speckle. *JOSA* 66 (11):1145-1150.

Goodman, Joseph W. 2007. *Speckle phenomena in optics: theory and applications*: Roberts and Company Publishers.

Goodman, N. R. 1963. Statistical analysis based on a certain multivariate complex Gaussian distribution (an introduction). *The Annals of mathematical statistics* 34 (1):152-177.

Guillaso, S., Ferro-Famil, L., Reigber, A., and Pottier, E. 2003. Urban area analysis based on ESPRIT/MUSIC methods using polarimetric interferometric SAR. *Proceedings of URBAN* 3.

Guillaso, S., Ferro-Famil, L., Reigber, A., and Pottier, E. 2005. Building characterization using L-band polarimetric interferometric SAR data. *IEEE Geoscience and Remote Sensing Letters* 2 (3):347–351.

Guo, H., Li, X., and Zhang, L. 2009. Study of detecting method with advanced airborne and spaceborne synthetic aperture radar data for collapsed urban buildings from the Wenchuan earthquake. *Journal of Applied Remote Sensing* 3 (1):031695-031695-031618.

Hajnsek, I., Pottier, E., and Cloude, S. R. 2003. Inversion of surface parameters from polarimetric SAR. *IEEE Transactions on Geoscience and Remote Sensing* 41 (4):727-744.

Hajnsek, Irena, Jagdhuber, Thomas, Schön, Helmut, and Papathanassiou, Konstantinos Panagiotis. 2009. Potential of estimating soil moisture under vegetation cover by means of PolSAR. *IEEE Transactions on Geoscience and Remote Sensing* 47 (2):442-454.

He, W., Jäger, M., Reigber, A., and Hellwich, O. 2008. Building extraction from polarimetric SAR data using mean shift and conditional random fields. *2008 7th European Conference on Synthetic Aperture Radar (EUSAR)*:1-4.

Henderson, FM, and Lewis, AJ. 1998. *Principles and applications of imaging radar. Manual of remote sensing, volume 2*: John Wiley and sons.

Hong, S H, and Wdowinski, S. 2014. Double-bounce component in cross-polarimetric SAR from a new scattering target decomposition. *IEEE Transactions on Geoscience and Remote Sensing* 52 (6):3039-3051.

Horn, R., Fischer, J., Marino, A., Nannini, M., Partington, K., Walker, N., and Woodhouse, I. 2007. The SARTOM project; Tomography for enhanced target detection for foliage penetrating airborne SAR (First-year results). *ElectroMagn. Remote Sens.-Defence Tech. Centre, Edinburgh, UK.*

Hu, H., and Ban, Y. 2012. Multitemporal RADARSAT-2 ultra-fine beam SAR data for urban land cover classification. *Canadian Journal of Remote Sensing* 38 (1):1-11.

Iwasa, S., and Susaki, J. 2011. Classification of building area using azimuth angle and density indices derived from polarimetric SAR. *2011 Joint Urban Remote Sensing Event (JURSE)*:269-272.

Jakeman, Eo. 1980. On the statistics of K-distributed noise. *Journal of Physics A: Mathematical and General* 13 (1):31-48.

Jin, Y., and Xu, F. 2013. *Polarimetric scattering and SAR information retrieval*: John Wiley & Sons.

Kajimoto, M., and Susaki, J. 2013a. Urban-area extraction from polarimetric SAR images using polarization orientation angle. *IEEE Geoscience and Remote Sensing Letters* 10 (2):337-341.

Kajimoto, M., and Susaki, J. 2012. Urban density estimation from polarimetric SAR images using polarization orientation angle. *IEEE International Geoscience and Remote Sensing Symposium (IGARSS 2012)* 5868-5871.

Kajimoto, M., and Susaki, J. 2013b. Urban density estimation from polarimetric SAR images based on a POA correction method. *IEEE Journal of Selected Topics in Applied Earth Observations and Remote Sensing* 6 (3):1418-1429.

Khan, S, and Guida, R. 2014. Application of Mellin-Kind statistics to Polarimetric distribution for SAR data. *IEEE Transactions on Geoscience and Remote Sensing* 52 (6):3513-3528.

Kimura, K., Yamaguchi, Y., Moriyama, T., and Yamada, H. 2004. Circular polarization correlation coefficient for detection of non-natural targets aligned not parallel to SAR flight path in the X-band POLSAR image analysis. *IEICE transactions on communications* E87-B (10):3050-3056.

Krogager, E. 1990. New decomposition of the radar target scattering matrix. *Electronics Letters* 26 (18):1525-1527.

Kusano, S., Takahashi, K., and Sato, M. 2014. Volume scattering power constraint based on the principal minors of the coherency matrix. *IEEE Geoscience and Remote Sensing Letters* 11 (1):361-365.

Lê, T. T., Atto, A. M., Trouvé, E., Solikhin, A., and Pinel, V. 2015. Change detection matrix for multitemporal filtering and change analysis of SAR and PolSAR image time series. *ISPRS Journal of Photogrammetry and Remote Sensing* 107:64-76.

Lang, F, Yang, J, and Li, D. 2015. Adaptive-window Polarimetric SAR image speckle filtering based on a homogeneity measurement. *IEEE Transactions on Geoscience and Remote Sensing* 53 (10):5435-5446. doi: 10.1109/TGRS.2015.2422737.

Lang, F., Yang, J., Li, D., Zhao, L., and Shi, L. 2014. Polarimetric SAR image segmentation using statistical region merging. *IEEE Geoscience and Remote Sensing Letters* 11 (2):509-513.

Lee, J., Grunes, M. R., Ainsworth, T. L., Du, L., Schuler, D. L., and Cloude, S. R. 1999. Unsupervised classification using polarimetric decomposition and the complex Wishart classifier. *IEEE Transactions on Geoscience and Remote Sensing* 37 (5):2249-2258.

Lee, J., and Pottier, E. 2009. *Polarimetric Radar Imaging: From Basics to Applications*. Edited by Boca Raton. FL, USA: CRC Press.

Lee, J. S. 2002. On the estimation of radar polarization orientation shifts induced by terrain slopes. *IEEE Transactions on Geoscience and Remote Sensing* 40 (1):30-41.

Lee, J. S., and Ainsworth, T. L. 2011. The effect of orientation angle compensation on coherency matrix and polarimetric target decompositions. *IEEE Transactions on Geoscience and Remote Sensing* 49 (1):53-64.

Lee, J. S., Du, L., Schuler, D. L., and Grunes, M. R. 1995. Statistical analysis and segmentation of multilook SAR imagery using partial polarimetric data. *IEEE International Geoscience and Remote Sensing Symposium, 1995. IGARSS'95*, 2:1422-1424.

Lee, J. S., Grunes, M. R., and De Grandi, G. 1999. Polarimetric SAR speckle filtering and its implication for classification. *IEEE Transactions on Geoscience and Remote Sensing* 37 (5):2363-2373.

Lee, J. S., Grunes, M. R., and Kwok, R. 1994. Classification of multi-look polarimetric SAR imagery based on complex Wishart distribution. *International Journal of Remote Sensing* 15 (11):2299-2311.

Lee, J. S., Hoppel, K. W., Mango, S. A., and Miller, A. R. 1994. Intensity and phase statistics of multilook polarimetric and interferometric SAR imagery. *IEEE Transactions on Geoscience and Remote Sensing* 32 (5):1017-1028.

Lee, JS, Schuler, DL, Lang, RH, and Ranson, KJ. 1994. K-distribution for multi-look processed polarimetric SAR imagery. *IEEE International Geoscience and Remote Sensing Symposium, 1994. IGARSS'94.*, 4:2179-2181.

Lee, K. Y., Oh, Y., and Kim, Y. 2012. Phase-difference of urban area in polarimetric SAR images. *Electronics Letters* 48 (21):1367-1368.

Lee, S. K. 2013. Forest parameter estimation using polarimetric SAR interferometry techniques at low frequencies. DLR.

Le Toan T, Beaudoin A, Riom J, et al. 1992. Relating forest biomass to SAR data. *IEEE Transactions on Geoscience and Remote Sensing*, 30(2): 403-411.

Le Toan T, Quegan S, Davidson M W J, et al. 2011. The BIOMASS mission: Mapping global forest biomass to better understand the terrestrial carbon cycle. *Remote sensing of environment*, 115(11): 2850-2860.

Le Toan T, Ribbes F, Wang L F, et al. 1997. Rice crop mapping and monitoring using ERS-1 data based on experiment and modeling results. *IEEE Transactions on Geoscience and Remote Sensing*, 35(1): 41-56.

Levinshtein, Alex, Stere, Adrian, Kutulakos, Kiriakos N, Fleet, David J, Dickinson, Sven J, and Siddiqi, Kaleem. 2009. Turbopixels: Fast superpixels using geometric flows. *IEEE Transactions on Pattern Analysis and Machine Intelligence* 31 (12):2290-2297.

Li, S, and Lu, H. 2011. Arbitrary body segmentation with a novel graph cuts-based algorithm. *IEEE Signal Processing Letters* 18 (12):753-756.

Li, X., Guo, H., Zhang, L., Chen, X., and Liang, L. 2012. A new approach to collapsed building extraction using RADARSAT-2 polarimetric SAR imagery. *IEEE Geoscience and Remote Sensing Letters* 9 (4):677-681.

Li, X., Pottier, E., Guo, H., and Ferro-Famil, L. 2010. Urban land cover classification with high-resolution polarimetric SAR interferometric data. *Canadian Journal of Remote Sensing* 36 (3):236-247.

Li, X., Zhang, L., Guo, H., Sun, Z., and Liang, L. 2012. New approaches to urban area change detection using multitemporal RADARSAT-2 polarimetric synthetic aperture radar (SAR) data. *Canadian Journal of Remote Sensing* 38 (3):253-266.

Liao, M., Zhang, L., and Balz, T. 2009. Post-earthquake landslide detection and early detection of landslide prone areas using SAR. *Urban Remote Sensing Event, 2009 Joint*:1-5.

Liu, B, Zhang, Z, Liu, X, and Yu, W. 2015. Representation and spatially adaptive segmentation for PolSAR images based on wedgelet analysis. *IEEE Transactions on Geoscience and Remote Sensing* 53 (9):4797-4809. doi: 10.1109/TGRS.2015.2410177.

Liu, B., Zhang, Z., Liu, X., and Yu, W. 2014. Edge extraction for polarimetric SAR images using degenerate filter with weighted maximum likelihood estimation. *IEEE Geoscience and Remote Sensing Letters* 11 (12):2140-2144. doi: 10.1109/LGRS.2014.2321629.

Liu, Bin, Hu, Hao, Wang, Huanyu, Wang, Kaizhi, Liu, Xingzhao, and Yu, Wenxian. 2013. Superpixel-based classification with an adaptive number of classes for polarimetric SAR images. *Geoscience and Remote Sensing, IEEE Transactions on* 51 (2):907-924.

Liu, M., Zhang, H., Wang, C., and Shan, Z. 2012. Urban change detection for high-resolution fully polarimetric SAR using a modified heterogeneous clutter model. *9th European Conference on Synthetic Aperture Radar, EUSAR 2012.* :87-90.

Liu, M., Zhang, H., Wang, C., and Wu, F. 2014. Change detection of multilook polarimetric SAR images using heterogeneous clutter models. *IEEE Transactions on Geoscience and Remote Sensing* 52 (12):7483-7494.

Liu, Ming-Yu, Tuzel, Oncel, Ramalingam, Srikumar, and Chellappa, Rama. 2011. Entropy rate superpixel segmentation. *Computer Vision and Pattern Recognition (CVPR), 2011 IEEE Conference on*:2097-2104.

Lopes, Armand, Touzi, Ridha, and Nezry, E. 1990. Adaptive speckle filters and scene heterogeneity. *IEEE Transactions on Geoscience and Remote Sensing* 28 (6):992-1000.

Martinez J M, Le Toan T. 2007. Mapping of flood dynamics and spatial distribution of vegetation in the Amazon floodplain using multitemporal SAR data. *Remote sensing of Environment* 108(3): 209-223.

Merzouki, A., McNairn, H., and Pacheco, A. 2010. Potential of mapping soil moisture by combining radar backscatter modeling and PolSAR decomposition. *IEEE International Geoscience and Remote Sensing Symposium (IGARSS 2010)*:4419-4422.

Migliaccio, M, Nunziata, F, and Buono, A. 2015. SAR polarimetry for sea oil slick observation. *International Journal of Remote Sensing* 36 (12):3243-3273.

Migliaccio, M., Nunziata, F., Montuori, A., Li, X., and Pichel, W. 2011. A multi-frequency polarimetric SAR processing chain to observe oil fields in the Gulf of Mexico. *IEEE Transactions on Geoscience and Remote Sensing* 49 (12):4729-4737.

Minh D H T, Van Trung L, Toan T L. 2015. Mapping ground subsidence phenomena in Ho Chi Minh City through the radar interferometry technique using ALOS PALSAR data. *Remote Sensing* 7(7): 8543-8562.

Mishra, B., and Susaki, J. 2013. Unsupervised change detection in an urban environment using multitemporal polsar images. *2013 Joint Urban Remote Sensing Event (JURSE)*:045-048.

Moriyama, T., Uratsuka, S., Umehara, T., Maeno, H., Satake, M., Nadai, A., and Nakamura, K. 2005. Polarimetric SAR image analysis using model fit for urban structures. *IEICE transactions on communications* E88-B (3):1234–1242.

Moriyama, T., Uratsuka, S., Umehara, T., Satake, M., Nadai, A., Maeno, H., and Yamaguchi, Y. 2004. A study on extraction of urban areas from polarimetric synthetic aperture radar image. *IEEE International Geoscience and Remote Sensing Symposium, 2004. IGARSS'04*, 1:703-706.

Moriyama, T., Yamaguchi, Y., Uratsuka, S., Umehara, T., Maeno, H., Satake, M., and Nakamura, K. 2005. A study on polarimetric correlation coefficient for feature extraction of polarimetric SAR data. *IEICE transactions on communications* 88 (6):2353-2361.

Nascimento, A. D. C., Horta, M. M., Frery, A. C., and Cintra, R. J. 2014. Comparing Edge Detection Methods Based on Stochastic Entropies and Distances for PolSAR Imagery. *IEEE Journal of Selected Topics in Applied Earth Observations and Remote Sensing* 7 (2):648-663. doi: 10.1109/JSTARS.2013.2266319.

Nghiem, S., Yueh, S., Kwok, R., and Li, F. 1992. Symmetry properties in polarimetric remote sensing. *Radio Science* 27 (5):693-711.

Niu, X. 2012. Multitemporal spaceborne polarimetric SAR data for urban land cover mapping. KTH Royal Institute of Technology.

Niu, X., and Ban, Y. 2012. An adaptive contextual SEM algorithm for urban land cover mapping using multitemporal high-resolution polarimetric SAR data. *IEEE Journal of Selected Topics in Applied Earth Observations and Remote Sensing* 5 (4):1129-1139.

Niu, X., and Ban, Y. 2013a. Multitemporal polarimetric RADARSAT-2 SAR data for urban land cover mapping through a dictionary-based and a rule-based model selection in a contextual SEM algorithm. *Canadian Journal of Remote Sensing* 39 (2):138-151.

Niu, X., and Ban, Y. 2013b. Multitemporal RADARSAT-2 polarimetric SAR data for urban land cover classification using an object-based support vector machine and a rule-based approach. *International Journal of Remote Sensing* 34 (1):1-26.

Niu, X., Ban, Y., and Dou, Y. 2015. RADARSAT-2 fine-beam polarimetric and ultra-fine-beam SAR data for urban mapping: comparison and synergy. *International Journal of Remote Sensing*:1-21.

Nunziata, F., Migliaccio, M., and Brown, C.E. 2012. Reflection symmetry for polarimetric observation of man-made metallic targets at sea. *IEEE Journal of Oceanic Engineering* 37 (3):384-394.

Oliver, C, and Quegan, S. 2004. *Understanding synthetic aperture radar images*: SciTech Publishing.

Pellizzeri, T. Macrı. 2003. Classification of polarimetric SAR images of suburban areas using joint annealed segmentation and 'H/A/a' polarimetric decomposition. *ISPRS Journal of Photogrammetry and Remote Sensing* 58 (1-2):55-70.

Qi, Z., Yeh, A., Li, X., and Lin, Z. 2012. A novel algorithm for land use and land cover classification using RADARSAT-2 polarimetric SAR data. *Remote Sensing of Environment* 118 (15):21-39.

Qin, F, Guo, J, and Lang, F. 2015. Superpixel segmentation for polarimetric SAR imagery using local iterative clustering. *IEEE Geoscience and Remote Sensing Letters* 12 (1):13-17. doi: 10.1109/LGRS.2014.2322960.

Reigber, A., Jager, M., He, W., Ferro-Famil, L., and Hellwish, O. 2007. Detection and classification of urban structures based on high-resolution SAR. *Proc. Urban Remote Sensing Joint Event, 2007 (JURSE'07)*, Paris, France, 1:1-6.

Rignot, E, Chellappa, R, and Dubois, P. 1992. Unsupervised segmentation of polarimetric SAR data using the covariance matrix. *IEEE Transactions on Geoscience and Remote Sensing* 30 (4):697-705.

Salehi, M., Sahebi, M. R., and Maghsoudi, Y. 2014. Improving the accuracy of urban land cover classification using radarsat-2 PolSAR data. *IEEE Journal of Selected Topics in Applied Earth Observations and Remote Sensing* 7 (4):1939-1404.

Sato, A., and Yamaguchi, Y. 2012. Four-component scattering power decomposition with extended volume scattering model. *IEEE Geoscience and Remote Sensing Letters* 9 (2):166-170.

Sato, M., Chen, S. W., and Satake, M. 2012. Polarimetric SAR analysis of tsunami damage following the March 11, 2011 East Japan earthquake. *Proceedings of the IEEE* 100 (10):2861-2875.

Santoro M, Fransson J E S, Eriksson L E B, et al. 2009. Signatures of ALOS PALSAR L-band backscatter in Swedish forest. *IEEE Transactions on Geoscience and Remote Sensing* 47(12): 4001-4019.

Santoro M, Fransson J E S, Eriksson L E B, et al. 2010. Clear-cut detection in Swedish boreal forest using multi-temporal ALOS PALSAR backscatter data. *IEEE Journal of Selected Topics in Applied Earth Observations and Remote Sensing* 3(4): 618-631.

Schou, J., Skriver, H., Nielsen, A. A., and Conradsen, K. 2003. CFAR edge detector for polarimetric SAR images. *IEEE Transactions on Geoscience and Remote Sensing* 41 (1):20-32. doi: 10.1109/TGRS.2002.808063.

Schuler, DL, and Lee, J-S. 2006. Mapping ocean surface features using biogenic slick-fields and SAR polarimetric decomposition techniques. *IEE Proceedings-Radar, Sonar and Navigation* 153 (3):260-270.

Shan, Z., Wang, C., Zhang, H., and An, W. 2012. Improved four-component model-based target decomposition for polarimetric SAR data. *IEEE Geoscience and Remote Sensing Letters* 9 (1):75-79.

Shan, Z., Zhang, H., and Wang, C. 2012. Four-component model-based decomposition of polarimetric SAR data for special ground objects. *IEEE Geoscience and Remote Sensing Letters* 9 (5):989-993.

Sharma, J. J., Hajnsek, I., Papathanassiou, K. P., and Moreira, A. 2011. Polarimetric decomposition over glacier ice using long-wavelength airborne PolSAR. *IEEE Transactions on Geoscience and Remote Sensing* 49 (1):519-535.

Shi, Jianbo, and Malik, Jitendra. 2000. Normalized cuts and image segmentation. *IEEE Transactions on Pattern Analysis and Machine Intelligence* 22 (8):888-905.

Shimada, M. 2011. Model-based polarimetric SAR calibration method using forest and surface-scattering targets. *IEEE Transactions on Geoscience and Remote Sensing* 49 (5):1712-1733.

Shimoni, M., Borghys, D., Heremans, R., Perneel, C., and Acheroy, M. 2009. Fusion of PolSAR and PolInSAR data for land cover classification. *International Journal of Applied Earth Observation and Geoinformation* 11 (3):169-180.

Shui, P., and Cheng, D. 2012. Edge detector of SAR images using Gaussian-Gamma-shaped bi-windows. *IEEE Geoscience and Remote Sensing Letters* 9 (5):846-850. doi: 10.1109/LGRS.2012.2184521.

Sieg, T. 2015. The potential of interferometric and polarimetric SAR data to characterize urban areas at the example of Mumbai and Manila. Universität Bayreuth.

Silva, W. B., Freitas, C. C., Sant'Anna, S. J., and Frery, A. C. 2013. Classification of segments in PolSAR imagery by minimum stochastic distances between Wishart distributions. *IEEE Journal of Selected Topics in Applied Earth Observations and Remote Sensing* 6 (3):1263-1273.

Singh, G., Yamaguchi, Y., and Park, S. E. 2013. General four-component scattering power decomposition with unitary transformation of coherency matrix. *IEEE Transactions on Geoscience and Remote Sensing* 51 (5):3014-3022.

Soergel, U. 2010. *Radar remote sensing of urban areas*. Edited by Andre Marcal. Vol. 15. Germany: Springer.

Song, H, Yang, W, Bai, Y, and Xu, X. 2015. Unsupervised classification of polarimetric SAR imagery using large-scale spectral clustering with spatial constraints. *International Journal of Remote Sensing* 36 (11):2816-2830.

Spigai, M., Tison, C., and Souyris, J. C. 2011. Time-frequency analysis in high-resolution SAR imagery. *IEEE Transactions on Geoscience and Remote Sensing* 49 (7):2699-2711.

Srivastava, Muni S. 1965. On the complex Wishart distribution. *The Annals of mathematical statistics* 36 (1):313-315.

Stefan, U. 2014. Advanced Techniques for Classification of Polarimetric Synthetic Aperture Radar Data. Tampere University of Technology.

Su, Xin, He, Chu, Feng, Qian, Deng, Xinping, and Sun, Hong. 2011. A supervised classification method based on conditional random fields with multiscale region connection calculus model for SAR image. *IEEE Geoscience and Remote Sensing Letters* 8 (3):497-501.

Susaki, J. 2013. Automatic extraction of buildings damaged by tsunami following 2011 East Japan Earthquake using aerial images. *IEEE International Geoscience and Remote Sensing Symposium (IGARSS 2013)* 699-702.

Susaki, J., Kajimoto, M., and Kishimoto, M. 2014. Urban density mapping of global megacities from polarimetric SAR images. *Remote Sensing of Environment* 155:334-348.

Tison, C., Nicolas, J. M., Tupin, F., and Maître, H. 2004. A new statistical model for Markovian classification of urban areas in high-resolution SAR images. *IEEE Transactions on Geoscience and Remote Sensing* 42 (10):2046-2057.

Touzi, R. 2002. A review of speckle filtering in the context of estimation theory. *IEEE Transactions on Geoscience and Remote Sensing* 40 (11):2392-2404.

Touzi R. 2007. Target scattering decomposition in terms of roll-invariant target parameters. *IEEE Transactions on Geoscience and Remote Sensing* 45 (1):73-84.

Touzi R, Goze S, Le Toan T, et al. 1992. Polarimetric discriminators for SAR images. *IEEE Transactions on Geoscience and Remote Sensing* 30(5): 973-980.

Treitz, P M, Howarth, P J, and Soulis, E D. 1996. Textural processing of multi-polarization SAR for agricultural crop classification. *IEEE International Geoscience and Remote Sensing Symposium, 1996. IGARSS'96*, 4:1986-1988.

Tu, S., Chen, J., Yang, W., and Sun, H. 2012. Laplacian eigenmaps-based polarimetric dimensionality reduction for SAR image classification. *IEEE Transactions on Geoscience and Remote Sensing* 50 (1):170-179.

Ulander L M H, LeToan T. 1999. Bragg-scattering resonance in VHF-SAR forestry data. Geoscience and Remote Sensing Symposium, *1999 IEEE International Proceedings IGARSS'99*. 4: 1886-1888.

Ulander L M H, Lundberg M, Pierson W, et al. 2005. Change detection for low-frequency SAR ground surveillance. *IET Proceedings Radar, Sonar and Navigation* 152(6): 413-420.

United Nations Department of Economic and Social Affairs. 2014. "Current world population." In. United Nations: Population Division.

Uratsuka, S., Kobayashi, T., Umehara, T., Matsuoka, T., Nadai, A., Satake, M., and Uemoto, J. 2010. Airborne SAR development at NICT: concept for new generation. *International Archives of the Photogrammetry, Remote Sensing and Spatial Information Science*, XXXVIII:133-136.

Vasile, G., Ovarlez, J. P., Pascal, F., Tison, C., Bombrun, L., Gay, M., and Trouve, E. 2008. Normalized coherency matrix estimation under the SIRV model. Alpine glacier POLSAR data analysis. *IEEE International Geoscience and Remote Sensing Symposium, 2008. IGARSS 2008*, Boston, MA, 1:I-74-I-77.

Vasile, G., Ovarlez, J., Pascal, F., and Tison, C. 2010. Coherency matrix estimation of heterogeneous clutter in high-resolution polarimetric SAR images. *IEEE Transactions on Geoscience and Remote Sensing* 48 (4):1809-1826. doi: 10.1109/TGRS.2009.2035496.

Voigt, S., Riedlinger, T., Reinartz, P., Künzer, C., Kiefl, R., Kemper, T., and Mehl, H. 2005. "Experience and perspective of providing satellite based crisis information, emergency mapping & disaster monitoring information to decision makers and relief workers." In *Geo-information for Disaster Management*, 519-531. Springer.

Wang, N., Shi, G., Liu, L., Zhao, L., and Kuang, G. 2012. Polarimetric sar target detection using the reflection symmetry. *IEEE Geoscience and Remote Sensing Letters* 9 (6):1104-1108.

Wang, S., Liu, K., Pei, J., Gong, M., and Liu, Y. 2013. Unsupervised classification of fully polarimetric SAR images based on scattering power entropy and copolarized ratio. *IEEE Geoscience and Remote Sensing Letters* 10 (3):622-626.

Wang, Y., Tupin, F., and C., Han. 2010. Building detection from high-resolution PolSAR data at the rectangle level by combining region and edge information. *Pattern Recognition Letters* 31 (10):1077-1088.

Wang, Y., Tupin, F., Han, C., and Nicolas, J. M. 2008. Building detection from high resolution POLSAR data by combining region and edge information. *IEEE International Geoscience and Remote Sensing Symposium, 2008. IGARSS 2008.* , 4:IV-153-IV-156.

Wu, W, Guo, H, and Li, X. 2015. Urban area SAR image man-made target extraction based on the product model and the Time-Frequency analysis. *IEEE Journal of Selected Topics in Applied Earth Observations and Remote Sensing* 8 (3):943-952. doi: 10.1109/JSTARS.2014.2371064.

Wu, W., Guo, H., and Li, X. 2013. Man-made target detection in urban areas based on a new azimuth stationarity extraction method. *IEEE Journal of Selected Topics in Applied Earth Observations and Remote Sensing* 6 (3):1138-1146.

Wu, W, Guo, H., and Li, X. 2014. Urban area man-made target detection for PolSAR data based on a nonzero-mean statistical model. *IEEE Geoscience and Remote Sensing Letters* 11 (10):1782-1786.

Xiang, D., Tang, T., Zhao, L., and Su, Y. 2013. Superpixel generating algorithm based on pixel intensity and location similarity for SAR image classification. *IEEE Geoscience and Remote Sensing Letters* 10 (6):1414-1418.

Xiao, S, Chen, S, Chang, Y, Li, Y, and Sato, M. 2014. Polarimetric coherence optimization and its application for manmade target extraction in PolSAR data. *IEICE Transactions on Electronics* E97-C (6):566-574.

Xie, L., Zhang, H., Wang, C., Liu, M., and Zhang, B. 2015. Superpixel-based PolSAR images change detection. *IEEE 5th Asia-Pacific Conference on Synthetic Aperture Radar (APSAR 2015)* 792-796.

Xu, J., Zhang, L., Wang, Y., Wang, H., and Liao, M. 2013. Urban change detection with polarimetric Advanced Land Observing Satellite phased array type L-band synthetic aperture radar data: a case study of Tai'an, China. *Journal of Applied Remote Sensing* 7 (1):073481-073481.

Yamaguchi, Y. 2012. Disaster monitoring by fully polarimetric SAR data acquired with ALOS-PALSAR. *Proceedings of the IEEE* 100 (10):2851-2860.

Yamaguchi, Y., Moriyama, T., Ishido, M., and Yamada, H. 2005. Four-component scattering model for polarimetric SAR image decomposition. *IEEE Transactions on Geoscience and Remote Sensing* 43 (8):1699–1706.

Yamaguchi, Y., Sato, A., Boerner, W. M., Sato, R., and Yamada, H. 2011. Four-component scattering power decomposition with rotation of coherency matrix. *IEEE Transactions on Geoscience and Remote Sensing* 49 (6):2251-2258.

Yamaguchi, Y., Yajima, Y., and Yamada, H. 2005. A four-component decomposition of POLSAR images based on the coherency matrix. *IEEE Geoscience and Remote Sensing Letters* 3 (3):292–296.

Yang, W, Yin, X, Song, H, Liu, Y, and Xu, X. 2014. Extraction of built-up areas from fully polarimetric SAR imagery via PU learning. *IEEE Journal of Selected Topics in Applied Earth Observations and Remote Sensing* 7 (4):1207-1216.

Yao, K. 1973. A representation theorem and its applications to spherically-invariant random processes. *IEEE Transactions on Information Theory* 19 (5):600-608. doi: 10.1109/TIT.1973.1055076.

Yueh, SH, Kwok, R, and Nghiem, SV. 1994. Polarimetric scattering and emission properties of targets with reflection symmetry. *Radio Science* 29:1409-1409.

Zhang, L., Guo, H., Li, X., and Fu, W. 2010. Application of aspect angle normalized polsar images for urban building detection. *IEEE International Geoscience and Remote Sensing Symposium (IGARSS 2010)*:2735-2738.

Zhang, L., Zou, B., Cai, H., and Zhang, Y. 2008. Multiple-component scattering model for polarimetric SAR image decomposition. *IEEE Geoscience and Remote Sensing Letters* 5 (4):603-607.

Zhang, L., Zou, B., and Tang, W. 2012. Stokes matrix polarimetric similarity parameter and its application in target detection. *Remote Sensing Letters* 3 (2):93-100.

Zhang, L., Zou, B., Zhang, J., and Zhang, Y. 2010. Classification of polarimetric SAR image based on support vector machine using multiple-component scattering model and texture features. *EURASIP Journal on Advances in Signal Processing* 2010 (960831):1-9.

Zhang, Q., Ban, Y., Liu, J., and Hu, Y. 2011. Simulation and analysis of urban growth scenarios for the Greater Shanghai Area, China. *Computers, Environment and Urban Systems* 35 (2):126-139.

Zhao, L., Yang, J., Li, P., Zhang, L., Shi, L., and Lang, F. 2013. Damage assessment in urban areas using post-earthquake airborne PolSAR imagery. *International Journal of Remote Sensing* 34 (24):8952-8966.

Zhou, G., Cui, Y., Chen, Y., Yang, J., Rashvand, H., and Yamaguchi, Y. 2011. Linear feature detection in polarimetric SAR images. *IEEE Transactions on Geoscience and Remote Sensing* 49 (4):1453-1463. doi: 10.1109/TGRS.2010.2081373.

Zou, B., Zhang, Y., Cao, N., and Minh, N. P. 2015. A four-component decomposition model for PolSAR data using asymmetric scattering component. *IEEE Journal of Selected Topics in Applied Earth Observations and Remote Sensing* 8 (3):1051-1061.

Zyl, J. J. Van, Arii, M., and Y. Kim. 2011. Model-based decomposition of polarimetric SAR covariance matrices constrained for nonnegative eigenvalues. *IEEE Transactions on Geoscience and Remote Sensing* 49 (9):3452–3459.

Zyl, J., Zebker, H., and Elachi, C. 1987. Imaging radar polarization signatures: Theory and observation. *Radio Science* 22 (4):529-543.

Zyl, van, and J, Jakob. 2011. *Synthetic aperture radar polarimetry*. Vol. 2: John Wiley & Sons.